Phased array imaging of two dimensional Doppler microwave backscattering from spherical tokamak edge plasmas

David A. Thomas

Doctor of Philosophy

University of York

Physics

July 2016

Abstract

Doppler backscattering (DBS) in 1D is an established and powerful fusion plasma diagnostic technique. In this thesis we explore the capability of the novel Synthetic Aperture Microwave Imaging diagnostic (SAMI) in performing proof-of-principle 2D DBS experiments on the Mega Ampere Spherical Tokamak (MAST) and the National Spherical Torus eXperiment Upgrade (NSTX-U). Phenomena observed previously using 1D DBS systems such as intrinsic plasma spin up, momentum injection from neutral beams and sharp changes in power and turbulence velocity coinciding with the L-H transition are re-observed. In addition, SAMI's unique 2D DBS capability has enabled the first ever 2D maps of Doppler backscattered radiation to be constructed. These 2D maps reveal that, due to turbulence elongated along field lines, Doppler backscattered power is concentrated in directions perpendicular to the magnetic field. This distribution of backscattered power allows magnetic pitch angle to be measured. Results from the utilisation of this technique are presented using MAST and NSTX-U data. This procedure constitutes a new independent channel for diagnosing magnetic pitch angle and is the first case of pitch angle being measured using a microwave diagnostic. A method utilising microwave diagnostics is of particular interest as this presents the possibility of high temporal and spatial magnetic pitch measurements enabling, through application of Ampère's law, measurement of edge current density: an important parameter in governing pedestal stability. The new capabilities and limitations resulting from implementation of a 2D DBS phased array system are discussed. How such a 2D device might be further optimised is examined and areas of further study are proposed.

Contents

List of Figures

Acknowledgements

I would like to thank: Roddy Vann and Vladimir Shevchenko for their dedicated and enthusiastic supervision. Simon Freethy for numerous insightful discussions regarding phased array image inversion, plasma physics and the SAMI diagnostic, to name a few. Jakob Brunner who has been an invaluable colleague throughout my research and whose support has been greatly appreciated. Gary Taylor and Bob Ellis for their assistance and guidance throughout SAMI's installation on NSTX-U. All my colleagues at the York Plasma Institute and CCFE for countless informative conversations and for providing a highly enjoyable working environment. My parents for their unwavering encouragement and assistance over 26 years. Lastly, to Jane Taylor for her love and for always being there through good times and bad.

This work was funded, in part, by EPSRC under grants EP/H016732 and EP/K504178, the University of York, and the RCUK Energy Programme under grant EP/I501045. This work has been carried out within the framework of the EUROfusion Consortium and has received funding from the Euratom research and training programme 2014–2018 under Eurofusion project ER-WP15_CCFE-03. The views and opinions expressed herein do not necessarily reflect those of the European Commission.

Author's declaration

This thesis has not been submitted for any other award at this or any other institution. Work presented in this thesis has been published in the following journal articles and conference proceedings:

- *2D Doppler backscattering using synthetic aperture microwave imaging of mast edge plasmas* D. A. Thomas, K. J. Brunner, S. J. Freethy, B. K. Huang, V. F. Shevchenko, and R. G. L. Vann, Nuclear Fusion, **56**, 026013 (2016).

- *Simultaneous 2D Doppler backscattering from edge turbulence* D. A. Thomas, K. J. Brunner, S. J. Freethy, B. K. Huang, V. F. Shevchenko and R. G. L. Vann, Bulletin of the American Physical Society, **60** (2015). *http://adsabs.harvard.edu/abs/2015APS..DPPCO5001T*

- *Observations of 2D Doppler backscattering on MAST using SAMI* D. A. Thomas, K. J. Brunner, S. J. Freethy, B. K. Huang, V. F. Shevchenko and R. G. L. Vann, 12th International Reflectometry Workshop (IRW 12, Jülich) (2015). *http://hdl.handle.net/11858/00-001M-0000-0028-FE2D-6*

- *Modifications to the synthetic aperture microwave imaging diagnostic* K. J. Brunner, J. C. Chorley, N. A. Dipper, G. Naylor, R. M. Sharples, G. Taylor, D. A. Thomas and R. G. L. Vann, Review of Scientific Instruments, (Submitted 2016).

- *Preliminary measurements of the edge magnetic field pitch from 2-D Doppler backscattering in MAST and NSTX-U* R. G. L. Vann, K. J. Brunner, R. Ellis, G. Taylor, and D. A. Thomas, Review of Scientific Instruments, (Submitted 2016).

- *GPU-Based Data Processing for 2-D Microwave Imaging on MAST* J. C. Chorley, R. J. Akers, K. J. Brunner, N. A. Dipper, S. J. Freethy, R. M. Sharples, V. F. Shevchenko, D. A. Thomas, R. G. L. Vann, American Nuclear Society, **69**, 643 (2016).

All work presented in this thesis is original to the best knowledge of the author. References and acknowledgements have been given when appropriate.

Chapter 1

Motivation and background

1.1 Nuclear fusion energy research

Nuclear fusion offers the possibility of an elegant and permanent solution to humanity's energy needs. There is enough ubiquitously available terrestrial deuterium and lithium fuel to provide enough low carbon fusion energy to supply current global demand for millions of years [1]. Maintaining conditions for fusion to take place is an extremely delicate process; loss of control would immediately cease further reactions. In addition, the amount of fuel required in a reactor at any one time is tiny, typically a few grams. These two factors combined render fusion reactors exceedingly safe. Further still, future fusion reactors are likely to be economically favourable in the long term as they have high power-generation density, provide power on demand, do not suffer from diseconomies of scale and produce no long-lived radioactive waste.

There are currently three known methods for confining fusion fuel at the right conditions for them to fuse and produce energy: gravitational confinement, inertial confinement and magnetic confinement. Gravitational confinement is employed solely by nature in stars. During Inertial Confinement Fusion (ICF) a fuel pellet is compressed, typically by a laser, to fusion conditions and the fuel's inertia alone holds the fuel in place while fusion reactions occur. Magnetic confinement fusion (MCF) uses magnetic fields to confine the hot fusion fuel in the form of a plasma. MCF is the subject of this thesis and therefore gravitational confinement and ICF will not be discussed further.

Many devices have been used to confine fusion plasmas such as magnetic mirrors,

stellarators and tokamaks. Magnetic mirrors use the *mirror effect* [2] to confine plasma within a region of low magnetic field. Stellarators have a very low or zero plasma current [3], achieving poloidal magnetic rotation through a specific field coil geometry. Tokamaks induce a poloidal magnetic field by passing current through the plasma itself. Experimentally, tokamaks outperform other devices holding the world records for fusion triple product [4] and fusion gain $Q \sim 0.7$ [5]. At present, tokamaks are generally agreed to be the most credible candidates for commercial fusion power plants. ITER ("the Way" in Latin) is the next generation tokamak device and is designed to be the first fusion experiment to achieve net energy gain. It will be the world's largest magnetic confinement fusion experiment, approximately double the spatial dimensions of the current largest device (see Table 1.1), the Joint European Tourus (JET). The central mission of the ITER project is to achieve Q$\sim$10 operation with a fusion power of $\sim$500 MW for several hundred seconds [6]. ITER is intended to be a proof-of-principle device which will be followed by a commercial demonstration fusion power plant (DEMO) [7].

Though the central thrust of fusion research is concentrated on large "conventional" aspect ratio devices such as JET and ITER, the data presented in this thesis was obtained during experiments on MAST and NSTX-U. MAST and NSTX-U are "Spherical" Tokamaks (STs) because of their comparatively low aspect ratios (see Table 1.1). STs have been developed alongside JET and ITER and potentially provide a significantly lower cost route to fusion energy.

Parameter	**MAST** [8]	**NSTX-U** [9]	**JET** [10]	**ITER** [11]
Major radius (m)	0.7	0.9	2.96	6.2
Minor radius (m)	0.5	0.6	1.25	2
Aspect ratio	1.4	1.5	2.4	3.1
Max plasma current (MA)	1	2	3.7	17
Max magnetic field (T)	0.5	1	3.4	5.3
Max shot length (s)	0.5	5	20	1000

Table 1.1: MAST and NSTX-U machine parameters

1.2 Spherical tokamaks

From the 1980s onwards it was well known that due to magnetohydrodynamic considerations, tokamak plasmas are inherently more stable at lower aspect ratios [12]. This increased stability allows Spherical Tokamaks (STs) to achieve higher plasma pressures for a given magnetic field [13]. STs are said to achieve a higher β which is a key performance metric used in tokamak design. β is defined as:

$$\beta = \frac{p}{\mu_0 B^2} \tag{1.1}$$

where p is the plasma pressure, μ_0 is the vacuum permeability, B is the magnetic field strength and the factor of 2 has been ignored. This increased performance would allow a ST power plant to be smaller and cheaper than a conventional aspect ratio design. However, STs are in a relatively early stage of development and have material science concerns, such as how to fit adequate neutron shielding around the centre column, that are yet to be addressed. However, in the nearer term it is thought that due to their high efficiency it could be possible to achieve a high fusion neutron flux environment in a relatively compact machine. Though it may not produce net energy gain, such a reactor could be used as a component test facility for fusion materials development [14].

1.3 H-mode and pedestal stability

In this section a brief overview of pedestal stability is discussed, for a more comprehensive treatment see [15].

Nuclear fusion power plants are expected to operate in the high confinement or H-mode. The transition to H-mode occurs when additional heating is applied to a low impurity ohmic plasma via either neutral beam injection (NBI) or radio frequency (RF) waves. H-mode is characterised by a transport barrier at the plasma edge which forms a pedestal in the density and temperature profiles (the grey shaded region in figure 1.1). The formation of this transport barrier is poorly understood though it is thought to be caused by suppression of edge turbulence due to shear flows [16].

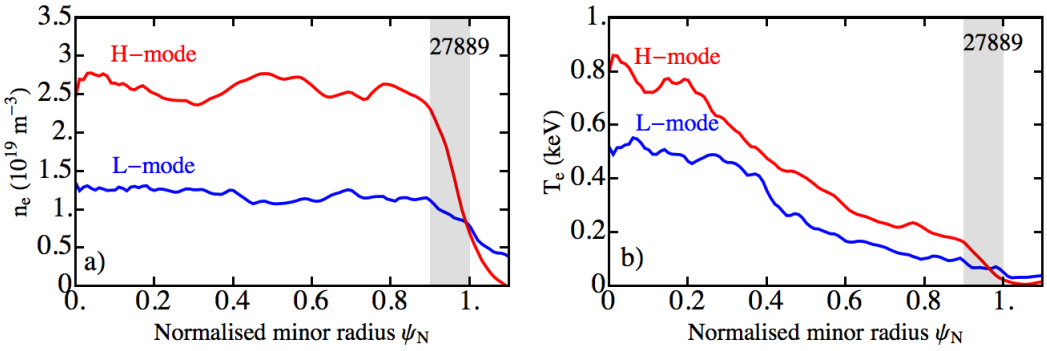

Figure 1.1: Electron number density (a) and temperature (b) profiles shown in L-mode (blue) and H-mode (red) for MAST shot 27889. The pedestal region is shaded grey.

H-mode operation is often accompanied by abrupt edge perturbations known as Edge Localised Modes (ELMs) [17]. Although ELMs can have beneficial effects, such as transporting impurities across the pedestal, they also significantly increase incident heat flux on the tokamak first wall components, particularly in the divertor region. In a DEMO scale device it is likely that the heat fluxes associated with ELMs would be intolerable and would cause permanent damage to the reactor divertor plates. The divertor is an expensive component and the need for its periodic replacement would seriously undermine the economic competitiveness of future fusion power stations. In addition, ELMs limit the height of the pedestal resulting in degraded confinement. It is generally agreed that a detailed, predictive understanding of ELMs is critical for the successful operation of next generation fusion devices.

Peeling-ballooning theory [15,18] proposes a mechanism for ELM onset and predicts pedestal height limits. It also highlights the importance of the interplay between bootstrap current and pressure gradient in pedestal stability. High toroidal mode number (n) pressure-driven ballooning modes couple with low n current-driven peeling modes at intermediate n ($3 < n < 20$) destabilising the pedestal by triggering ELMs. The stability limits imposed by these "peeling-ballooning" modes are shown schematically in figure 1.2. Within a certain region of p'_{ped} space the pedestal is stable. However, if the edge current or pressure gradient surpasses the stability limit then an ELM is triggered causing a relaxation of the plasma back into the stable region. Power moving radially outwards from the core causes the pedestal

gradient to rise between ELMs. The edge current (primarily bootstrap) lags behind this gradient increase. Type-III ELMs result when the density and input power are low so that the current has had time to reach the peeling limit before the pressure gradient reaches the ballooning limit (III in figure 1.2). If the pedestal gradients and current increase at similar rates then large type-I ELMs (I in figure 1.2) occur because as the pressure gradient collapses the pedestal remains in the unstable domain until the current density also relaxes to a value within the stable region. High input power can lead to type-II ELMs (II in figure 1.2) if the peeling limit is high due to strong shaping or large magnetic shear.

The edge pressure gradient is currently well diagnosed by, for example, Thomson scattering diagnostics [19]. However, high temporal and radial resolution measurements of the current density in the pedestal region have not yet been attained. In the absence of direct measurement the edge current density must be estimated using formulas [20], all of which have associated uncertainties. Therefore, edge current density is a highly sought after measurement as it allows peeling-ballooning models to be directly constrained accelerating their development.

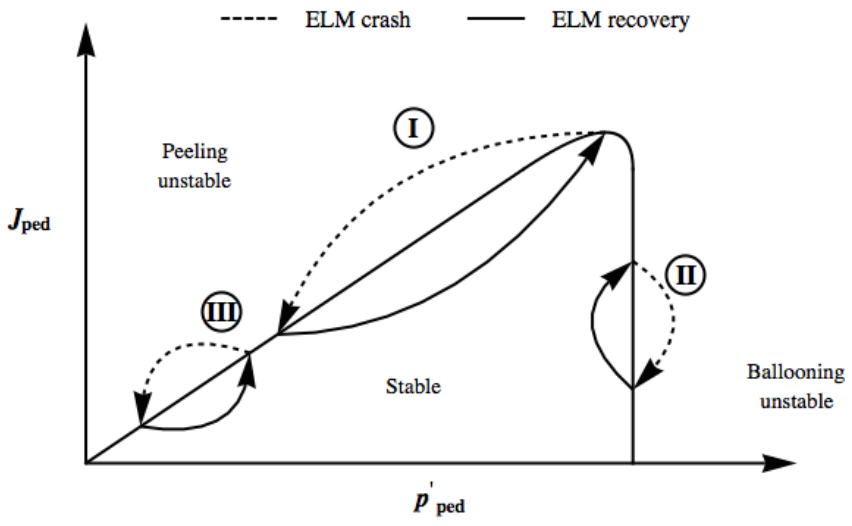

Figure 1.2: Simplified schematic diagram of stability limits in pedestal density gradient-current density (p'_{ped},J_{ped}) space. Type I, II and III ELM crash-recovery cycles are shown [15].

1.4 Microinstabilities and turbulence

Early on in magnetic fusion energy research in the 1950s scientists were optimistic, if heat and particle confinement was limited by collisional effects alone, net energy gain could be achieved imminently. Unfortunately, heat and particle transport was observed to be two orders of magnitude greater than that predicted by collisional estimates. Advances in theory, modelling and observations over the subsequent decades have resulted in the widely-held consensus that this so-called "anomalous transport" arises, in the absence of equilibrium-scale instabilities (sawteeth, kinks, tearing modes), as a result of gyroradius-scale "micro-instabilities". Micro-instabilities are driven by the free energy from density and temperature gradients. Micro-instabilities are not the subject of this thesis. However, Doppler backscattering diagnostics deployed on MCF experiments, as will be discussed further in section 2.1, analyse the radiation backscattered off turbulent structures caused by micro-instabilities. To give an insight into how these instabilities develop we will consider a few simplified examples.

1.4.1 Electron drift modes

Electron drift waves can be illustrated by considering a plasma slab in a uniform magnetic field (See figure 1.3). The magnetic field and density gradients are along the z and y-axes respectively. We consider a density perturbation to the background gradient where areas of increased and decreased density are indicated by $\delta \mathrm{n} > 0$ and $\delta \mathrm{n} < 0$ in figure 1.3 respectively. This initial perturbation creates an electron pressure which, due to their low inertia, the electrons respond by rapidly flowing along magnetic field lines. Electrons flow from regions of high density into regions of low density until the electron pressure is balanced by the electric field along the magnetic field. Let us consider the electron force balance (see Appendix A for derivation):

$$n_\mathrm{e} m_\mathrm{e} \Big(\frac{\partial \mathbf{v}_\mathrm{e}}{\partial t} + \mathbf{v}_\mathrm{e} \cdot \boldsymbol{\nabla} \boldsymbol{v}_\mathrm{e} \Big) = -\boldsymbol{\nabla} P_\mathrm{e} - n_\mathrm{e} e (\boldsymbol{E} + \boldsymbol{v}_\mathrm{e} \times \boldsymbol{B}) \tag{1.2}$$

where P_e is the electron pressure, e is the electronic charge, n_e the electron number density, $\boldsymbol{E}$ is the electric field, $\boldsymbol{v}_\mathrm{e}$ is the velocity of the fluid, m_e is the electron mass

and $\boldsymbol{B}$ is the magnetic field. Working in the plasma frame and considering only the component parallel to the magnetic field gives:

$$n_{\mathrm{e}} e \boldsymbol{E}_{\parallel} + \boldsymbol{\nabla}_{\parallel} P_{\mathrm{e}} = 0 \tag{1.3}$$

If we linearise Equation 1.3 and assume electrostatic perturbations:

$$n_{\mathrm{e}} \rightarrow n_{\mathrm{e0}} + \delta n_{\mathrm{e}} \tag{1.4}$$

$$\boldsymbol{E}_{\parallel} \rightarrow \boldsymbol{\nabla}_{\parallel}(\phi_0 + \delta\phi) \tag{1.5}$$

$$P_{\mathrm{e}} \rightarrow T_{\mathrm{e0}}(n_{\mathrm{e0}} + \delta n_{\mathrm{e}}) \tag{1.6}$$

we can derive the relation

$$\frac{\delta n_{\mathrm{e}}}{n_{\mathrm{e0}}} = \frac{e\delta\phi}{T_{e0}}. \tag{1.7}$$

where n_{e0}, T_{e0}, ϕ_0 are the equilibrium electron number density, temperature and electrostatic potential respectively. Perturbations to the equilibrium electron number density and electrostatic potential are given by δn_{e} and $\delta\phi$ respectively. Equation 1.7 indicates density perturbations along the x-axis give rise to an electric field from regions of higher to lower density as indicated in figure 1.3. The resulting $E \times B$ velocity then acts to reduce the density in areas of high density and increase the density of regions of low density. This causes the density and electrostatic potential perturbations to oscillate in time. The resulting wave that propagates down the x-axis, as indicated in figure 1.3, is an electron drift wave.

If the $E \times B$ flow and density perturbations are out of phase by $\pi/2$, as is the case if all non-ideal effects are ignored, then the mode does not grow and there is no net radial transport. However, if the electrons cannot keep up with the wave then this leads to a phase shift and growth of the mode. This can happen if one takes into account finite electron mass, collisions or Landau damping. This causes the drift wave to destabilise and the resulting microinstability is called the electron drift mode. This instability is ubiquitous in tokamaks as all plasmas have density gradients and dissipation; however, these modes can be stabilised through magnetic shear.

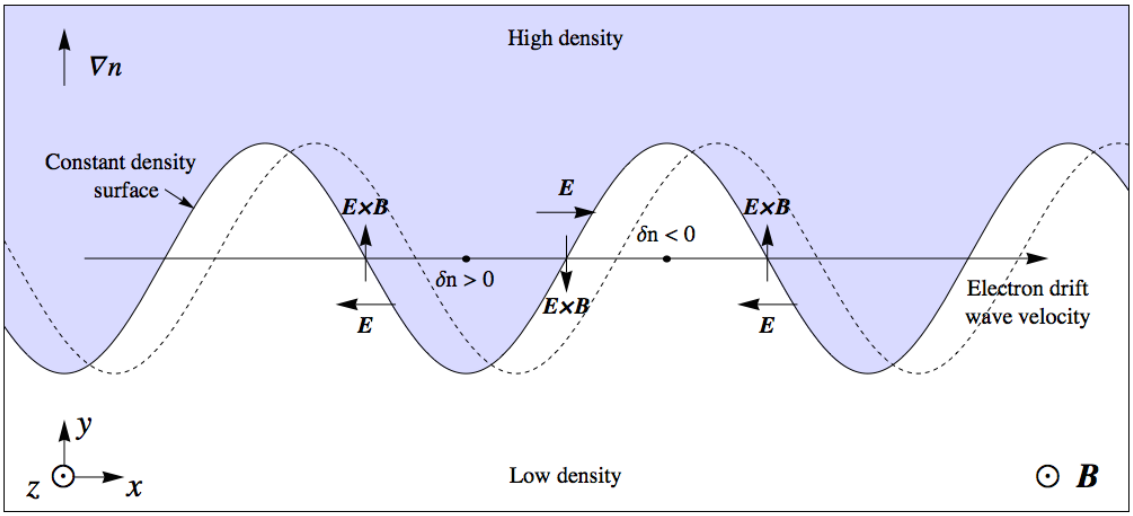

Figure 1.3: Illustration of the electron drift wave. A constant density surface is represented by a continuous black line at an initial time and the dashed curve at a later time. Regions where the density is greater than the line of constant density are shaded [21].

1.4.2 The ion temperature gradient mode

Figure 1.4 shows a plasma slab of uniform density with a temperature gradient along the y-axis. Let the magnetic field be orientated along the z-axis and increase in magnitude along the y-axis so that the ∇B-drift velocity is oriented in the negative x direction. If we assume that there is a initial small density perturbation, indicated by the continuous black line in figure 1.4, then the hotter regions will drift faster than the cooler regions. This will lead to regions of higher and lower density, indicated by $\delta n > 0$ and $\delta n < 0$ respectively in figure 1.4. Due to the electron adiabatic response (Equation 1.7) this gives rise to E-fields orientated as shown in figure 1.4. The resulting $E \times B$ drift amplifies the initial perturbation causing the mode to grow. This is the Ion Temperature Gradient (ITG) mode which has been studied extensively, for example [22], and is thought to be a major source of transport in tokamak plasmas. As the ITG mode depends on the ∇B-drift it has a wavelength of a few ion Larmor radii. The scale of the resulting fluctuations is given by $K_\perp \rho_\mathrm{i} \sim 0.3$ where $K_\perp$ is the component of the turbulent wave vector perpendicular to the magnetic field and ρ_i is the ion Larmor radius [23].

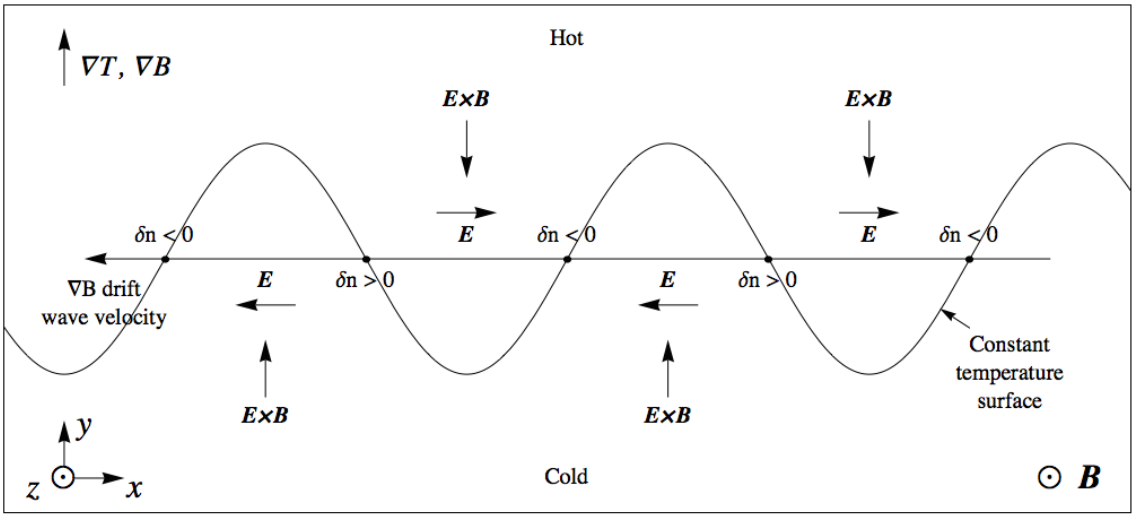

Figure 1.4: The physical mechanism for the Ion Temperature Gradient (ITG) mode. The continuous line indicates a contour of constant temperature [24].

1.4.3 Other microinstabilities

There are many microinstabilities in addition to electron drift and ITG modes. The Electron Temperature Gradient (ETG) mode, for example, is similar to the ITG with the roles of the electrons and ions reversed [25]. ETGs have small wavelengths and are thought to instigate fluctuations at small scales ($K_\perp \rho_\mathrm{i} \sim 10$) [23]. Trapped particles in tokamak plasmas are confined to the bad curvature, outboard side, resulting in a net drift. The passing particles act as a background source of electrons invoking an electron adiabatic response resulting in another drift type instability, the Trapped Electron Mode (TEM), which typically manifests itself at intermediate-scales ($K_\perp \rho_\mathrm{i} \sim 1$) [23]. In addition to ITGs, TEMs and ETGs there are microtearing [26], kinetic ballooning (concentrated in the H-mode pedestal region as discussed in section 1.3) [27] and impurity modes [28].

The effects of the different instabilities cannot be added together to form a solution as modes of different length scales interact nonlinearly resulting in turbulence. Within a magnetised plasma these turbulent eddies are elongated along the magnetic field so that $K_\parallel << K_\perp$ ($K_\perp$ is the component of the turbulence wave vector aligned perpendicular to the magnetic field).

1.5 Electromagnetic waves in cold plasma

If one ignores the thermal motion of the particles, treats the plasma as a fluid with an effective relative permittivity, assumes the frequency of the waves are much greater than the temporal wavelength and assumes the wavelength of the radiation is much shorter then the spatial variation of the background plasma, then the Appleton-Hartree relation can be derived [29–33]:

$$N^2 = 1 - \frac{2X(1-X)}{2(1-X) - Y^2\sin^2\theta \pm \gamma} \tag{1.8}$$

where

$$\gamma = \sqrt{Y^4\sin^4\theta + 4(1-X)^2Y^2\cos^2\theta}$$

and $X = \omega_{\mathrm{pe}}^2/\omega^2$, $Y = \omega_{\mathrm{ce}}/\omega$. The plasma frequency, electron cyclotron frequency, radiation frequency and angle of propagation to the magnetic field are given by ω_{pe}, ω_{ce}, ω and θ respectively. When light is propagating parallel to the magnetic field the "+" and "-" solutions corresponds to the left and right circularly polarised modes (L and R-modes) respectively. When light is propagating perpendicular to the magnetic field the "+" and "-" solutions correspond to the ordinary and extraordinary modes (O and X-modes) respectively. If the alignment is initially along the magnetic field and is slowly rotated to perpendicular propagation then the right and left-hand modes will evolve into the X-mode and O-modes respectively. Therefore, for oblique propagation we will refer to the LO and RX-modes.

For propagation parallel to the magnetic field Equation 1.8 simplifies to

$$N^2 = 1 - \frac{X}{1 \pm Y}. \tag{1.9}$$

Setting $N = 0$ in Equation 1.9 and solving for ω tells us that there are two cutoffs for parallel propagation given by

$$\omega_{1,2} = \frac{1}{2}[(\omega_{\mathrm{ce}}^2 + 4\omega_{\mathrm{pe}}^2)^{\frac{1}{2}} \pm \omega_{\mathrm{ce}}], \tag{1.10}$$

henceforth we will refer to these solutions as the upper (ω_1) and lower (ω_2) density cutoffs.

For propagation perpendicular to the magnetic field the "+" solution simplifies and results in the O-mode dispersion relation which is the same as that for an unmagnetised plasma:

$$N^2 = 1 - X \tag{1.11}$$

The "-" solution results in the X-mode dispersion relation:

$$N^2 = 1 - \frac{X(1-X)}{1-X-Y^2} \tag{1.12}$$

Just as in an unmagnetised plasma, setting $N = 0$ in Equation 1.11 and solving for ω gives a cutoff at the plasma frequency ω_{pe}. Setting $N = 0$ in Equation 1.12 and solving for ω shows that there are cutoffs, as for parallel propagation, at the upper and lower density cutoffs ($\omega_{1,2}$). However, there is also a resonance at the upper hybrid frequency:

$$\omega_{\mathrm{UH}} = \sqrt{\omega_{pe}^2 + \omega_{ce}^2}. \tag{1.13}$$

For a fixed value of magnetic field the parallel and perpendicular dispersion relations are plotted as a function of X in figures 1.5(a).

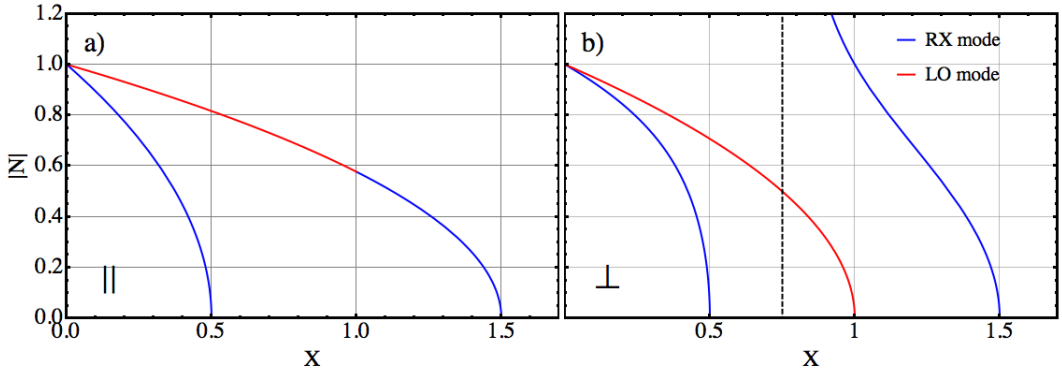

Figure 1.5: (a) and (b) dispersion relations for radiation propagating parallel and perpendicular to the magnetic field respectively with a constant magnetic field ($Y = 0.5$). The RX mode is shown in blue and the LO mode is shown in red. The upper hybrid resonance is indicated by the vertical dashed black line at $X = 0.75$.

1.6 Outline and scope of thesis

In this thesis we investigate the feasibility of utilising phased arrays to conduct 2D Doppler backscattering experiments on magnetised fusion plasmas. Results from experiments conducted on the MAST and NSTX-U spherical tokamaks using the synthetic apperture microwave imaging diagnostic (SAMI) are presented.

Chapter 2 starts by describing the principles of Doppler backscattering in magnetised plasmas along with a review of the field. A brief introduction to the relevant data processing techniques and computational models is also given.

A detailed introduction to the SAMI diagnostic including a hardware description, the array optimisation procedure, side-band separation and polarimetry is given in Chapter 3.

Chapter 4 describes the calibration and proof-of-principle experiments conducted in the lab prior to SAMI's installation onto MAST and NSTX-U. These experiments verified SAMI's ability to accurately measure the spatial location and extent of a Doppler shifted source as well as the consequences of 3D scattering effects in the recieving array. The antenna gain patterns and cross talks of the sinuous and Vivaldi antennas were also measured and compared.

An overview of SAMI's installation on MAST and NSTX-U is given in Chapter 5. The location of normal incidence cutoffs during L and H-modes on both devices as well as maps of probing $k_{\parallel}$ and $k_{\perp}$ values are presented.

Chapter 6 presents results from SAMI DBS experiments conducted on the MAST tokamak. Many previously observed qualitative effects are observed in the SAMI DBS signal. In addition, the first ever 2D maps of Doppler backscattered radiation are presented. Using the distribution of red and blue-shifted radiation on these maps, it is shown that a magnetic pitch angle measurement can be made. This pitch angle measurement is shown to be consistent with results from other diagnostics.

An overview of the results obtained during experiments conducted on NSTX-U are presented in Chapter 7. The same qualitative effects that were observed on MAST are also seen in the NSTX-U data. NSTX-U magnetic pitch angle measurements are presented and are shown again to be consistent with other diagnostics.

The main conclusions regarding the feasibility of the 2D phased array DBS method are presented in Chapter 8 along with recommendations for future work.

These recommendations include a number of experiments that could be conducted using SAMI in its current configuration as well as possible upgrades to the system. Potential designs for future phased array 2D DBS systems are also discussed.

Chapter 2

Experimental techniques

Declaration

Some discussion in this chapter has been previously published in [34, 35].

2.1 Doppler backscattering

Doppler backscattering (DBS) was born out of conventional reflectometry when propagating density fluctuations were found to cause the phase of the backscattered signal to continuously increase (referred to as "phase runaway") when the antenna was oriented oblique to the normal incidence cutoff surface [36]. DBS maintains many of the advantages of reflectometry such as: infrequent access to experimental hardware required, only a small amount of port space needed and high spatial and temporal resolution. As with most microwave diagnostics, DBS systems can be conducted using antennas fabricated from materials resistant to high heat and neutron flux. In addition, waveguides allow electronic components to be delocalised from the reactor and located behind neutron shielding if necessary. Therefore, DBS is one of the few plasma diagnostics techniques that is suitable for installation on next generation fusion reactors rendering its development essential.

Through measuring the Doppler shift and power (proportional to the turbulence amplitude in the linear regime [37]) of the backscattered beam, DBS experiments have been used to measure perpendicular velocity profiles of turbulence structures and turbulence amplitudes on ASDEX Upgrade (AUG) [38], DIII-D [39],

W7-AS [40, 41], EAST [42], HL-2A [43], LHD [44], L-2M [45], and MAST [46]. In addition, if the $E \times B$ velocity dominates the turbulence velocity then the radial electric field can be calculated: a parameter of great importance in fusion research because of the suppression of microinstabilities through $E_{\mathrm{r}} \times B$ velocity shear [47]. Mechanically steerable mirrors and antennas have allowed k spectra to be measured in addition to turbulence velocity on DIII-D [48], TJ-II [49], Tore Supra [50] and AUG [51]. Resolving k-spectra advances the study of reduced transport regimes where turbulence suppression is often non-uniform in space and wave-number. In addition, by looking at the driving scale of the turbulence, wave-number spectra can be used to spatially localise and identify microinstabilities.

DBS has also been used to study the toroidal and radial structure of geodesic acoustic modes on DIII-D [39, 52, 53], AUG [54], TCV [55], Tore Supra [56, 57] and FT-2 [58]. The perpendicular velocity, size and quasi-toroidal mode numbers of filaments in the edge region were determined using DBS on Globus-M [59].

A conventional DBS experiment comprises a single antenna (assuming a mono static arrangement) launching a beam oriented perpendicular to the magnetic field and, in contrast with reflectometry, *oblique* to the normal incidence cutoff surface. The returned signal is Bragg-backscattered off turbulent structures elongated along the magnetic field lines. Either O or X-mode probing can be used; X-mode tends to be preferred as full wave modelling predicts greater scattering efficiency in the vicinity of the cutoff [60].

DBS is a coherent scattering process. In order for coherent scattering to occur, the phase difference between scattering from one electron and from electrons in its shielding cloud has to be small, i.e. $k\lambda_{\mathrm{D}} \ll 1$, where k is the wave vector of the radiation being scattered and λ_{D} is the Debye length [61]. As will be shown in section 5.1, typical values of k in the scattering regions of NSTX-U and MAST are $k \sim 1$ cm^{-1} at SAMI frequencies. The Debye length in the edge region of the MAST plasma is $\lambda_{\mathrm{D}}) \sim 10^{-4}$ m. Therefore, $k\lambda_{\mathrm{D}} \sim 0.01$, satisfying the coherent scattering criterion.

2.1.1 Principles of Doppler backscattering

The principle of Doppler backscattering can be illustrated if one considers a beam propagating in vacuum incident on a turbulent reflecting layer (modelled as a sinusoidal corrugation of wave-number $K_\perp = 2\pi/\Lambda_\perp$ moving at velocity $\boldsymbol{v}_\perp$) at an oblique angle (see figure 2.1). For the diffraction pattern of order -1 to return to the launching antenna the Bragg condition requires

$$K_\perp = 2k_0 \sin\theta_t \tag{2.1}$$

where θ_t is the tilt angle of the antenna relative to the reflection surface normal and k_0 is the wave-number of the probing beam. From Equation 2.1 one can see that by changing the inclination of the antenna the $K_\perp$ spectrum of the turbulence can be scanned.

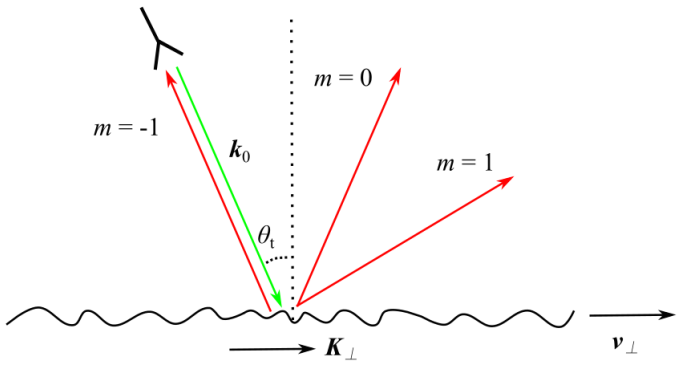

Figure 2.1: Cartoon depicting the principle of Doppler reflectometry. The incident beam of microwaves (in vacuum) is indicated by the green arrow. The scattered beams of microwaves are indicated by the red arrows (-1$^{\text{th}}$, 0$^{\text{th}}$ and 1$^{\text{th}}$ diffraction orders are shown). The turbulent reflecting layer is indicated by the continuous black line.

The Doppler shift of the backscattered beam is given by

$$\Delta\omega = 2v_\perp k_0 \sin\theta_t \tag{2.2}$$

$$= v_\perp K_\perp \tag{2.3}$$

2.1.2 Doppler backscattering in fusion plasmas

In this section we present a more realistic scenario than that in 2.1.1. Figure 2.2 shows a magnetised plasma slab where the density is increasing along the negative y-axis and the magnetic field is oriented along the z-axis. The incident beam's trajectory is at an oblique angle to the density surface normal and is aligned perpendicular to the magnetic field. As the beam enters the plasma it refracts as the refractive index (N) and wave vector of the probing beam (k) decrease (see figure 1.5). Fluctuation measurements in tokamaks using Beam Emission Spectroscopy (BES), reflectometry, heavy ion beam probes and laser scattering have shown that turbulence amplitude decreases as K^{-3} or faster for intermediate wave-numbers ($K_\perp \rho_i \sim 1$) in tokamaks [62]. In addition, analytical investigation of DBS using a two-dimensional slab model and employing the linear Born approximation has predicted that backscattering efficiency $\propto K^{-2}$ [63]. Consistent with these empirical and theoretical predictions, a K^{-5} scattered power dependence has been measured directly on MAST [46]. Therefore, although scattering occurs continuously along the path of the beam, backscattering is highly localised in the region of lowest k along the beam's path. Therefore, scattering occurs primarily at the reflection point where the beam is propagating perpendicular to the density surface normal and the Bragg condition becomes

$$K_\perp^{\mathrm{B}} \simeq -2k_{\mathrm{sc}} \tag{2.4}$$

where $K_\perp^{\mathrm{B}}$ is the binormal component of the density perturbations perpendicular to the equilibrium magnetic field and density surface normal. The incident wavenumber of the probing beam at the scattering location is given by k_{sc}.

2.1.3 Interpreting Doppler backscattered data

In this section a brief outline of the theory used to extract plasma parameters from DBS data is presented. Radial force balance requires that for each species in the plasma:

$$E_{\mathrm{r}} = \frac{\nabla P}{en} + v_\phi B_\theta - v_\theta B_\phi \tag{2.5}$$

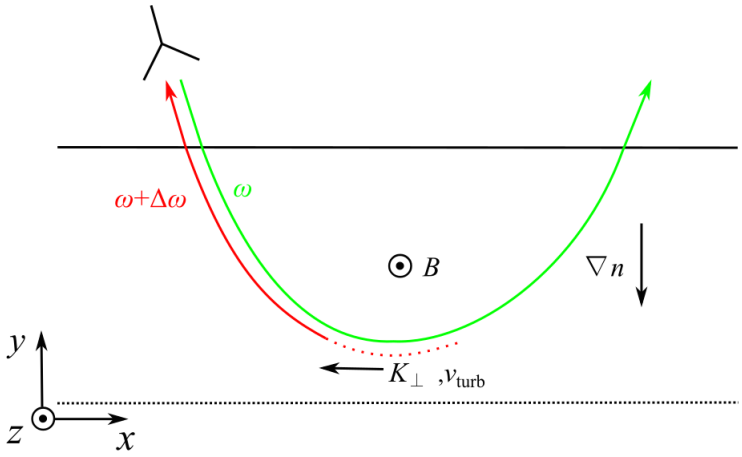

Figure 2.2: Cartoon representing DBS in a magnetised plasma. The plasma-vacuum boundary is indicated by the horizontal black continuous line. The incident and backscattered beams are represented by the green and red arrows respectively. The normal incidence cutoff is indicated by the horizontal black dashed line.

where E_r is the radial electric field, P is either the ion or electron pressure and n is either the ion or electron number density. The rotation velocity and magnetic field are denoted by v and B respectively. The ϕ and θ subscripts refer to the toroidal and poloidal directions respectively. The turbulent velocity has contributions from the $E \times B$ velocity and the phase velocity of the turbulence, $v_\mathrm{turb} = v_{E\times B} + v_\mathrm{phase}$. In the plasma edge the $E \times B$ velocity is generally much larger than the phase velocity of the dominant drift-wave turbulence [38, 40, 64], therefore $v_\mathrm{turb} \simeq v_{E\times B}$. Using the definition of the $E \times B$ velocity ($\mathbf{v}_{E\times B} = \frac{1}{B^2}\mathbf{E} \times \mathbf{B}$) and assuming $E_\phi = E_\theta = 0$ and $B_r = 0$ [65]:

$$E_\mathrm{r} = v_{E\times B} B. \tag{2.6}$$

Combining Equation 2.6 and 2.5 the turbulent velocity can be written as

$$v_\mathrm{turb} = v_{E\times B} = \frac{\nabla P}{qnB} + v_\phi \frac{B_\theta}{B} - v_\theta \frac{B_\phi}{B} \tag{2.7}$$

where the first term on the right-hand side of Equation 2.7 is the diamagnetic velocity and q is the charge of the species being considered. The second and third terms on the right-hand side are the contributions to the turbulent velocity from the toroidal and poloidal rotation of the plasma respectively.

If, for example, the aim of a DBS experiment is to measure the radial E_{r} field in the plasma edge, then a ray tracing code is used to calculate the location and value of k at the point of minimum $K_{\perp}$ along the path of the beam (k_{sc}). The wave vector at the scattering location can then be used, in conjunction with the measured Doppler shift, to calculate a turbulence velocity. The radial electric field can then be calculated using Equation 2.6 as is done in [38]. The scattering location is provided by ray-tracing, which can be used with a Grad-Shafranov equilibrium solver such as EFIT, to provide a value of B at the scattering location.

If the aim of the DBS experiments is to measure turbulent velocity then Equation 2.7 is used. Often the diamagnetic velocity and polidal roation are negligible [66], therefore,

$$v_{\mathrm{turb}} \simeq v_{\phi}\frac{B_{\theta}}{B}. \tag{2.8}$$

Again, as the scattering location is known from beam-tracing the magnetic field information can be derived from EFIT. On MAST toroidal rotation, as measured by a DBS diagnostic [46], has been compared with that measured from Beam Emission Spectroscopy (BES) [67] and Charge eXchange Recombination Spectroscopy (CXRS) [68] diagnostics; they were found to be in good agreement. It is notable from this discussion that DBS systems are dependent on other diagnostics to extract plasma parameters which is an unfortunate disadvantage of the technique. In addition, the core of tokamak plasmas are often dominated by turbulence that is more ITG and TEM-like [69]. In this case the phase velocity may no longer be negligible complicating the extraction of E_{r}.

2.2 Beam forming

The image inversion algorithm employed on the SAMI active probing data is based on the beam forming technique. Beam forming is a well established signal processing technique for phased arrays and has been applied in radar [70], sonar [71], seismology [72], wireless communications [73], radio astronomy [74], acoustics [75] and biomedicine [76]. The principle of beam forming is outlined below in figure 2.3: two parallel rays emanating from a source in the far field, at incident angle θ, are

shown incident on two antennas separated by distance b. If data from both antenna channels is digitised and the wavelength of the incident radiation is λ, then constructive interference will occur when the phase of one channel is shifted by $\frac{2\pi}{\lambda} b \sin\theta$. The same principle is applied when analysing SAMI data. However, SAMI data analysis is complicated by the following factors: the source is not assumed to be in the far field, the problem is 3D and SAMI receives data on eight antenna channels.

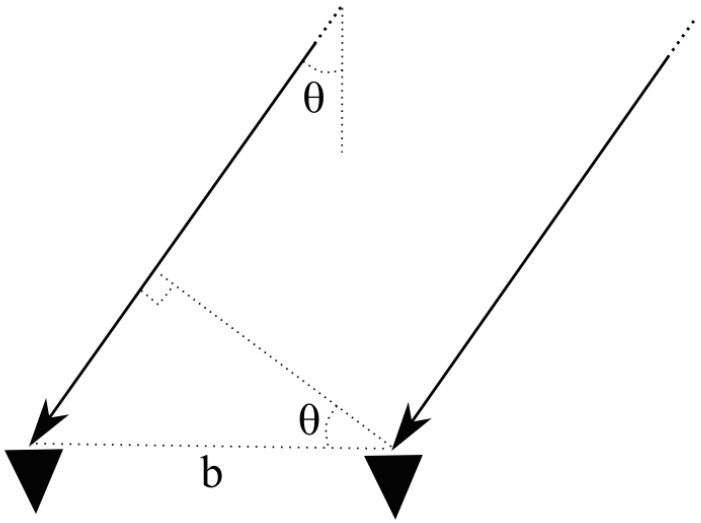

Figure 2.3: The principle of beam forming: two rays emanating from a source in the far field incident on two antennas. The antennas are indicated by the black triangles, and the rays are indicated by the black arrows. The incident rays are orientated at angle θ to the vertical and the two antennas are separated by b.

2.2.1 Frequency domain beam forming

Let us consider a receiving array positioned at the origin of a Cartesian coordinate system with its field of view centred along the positive x-axis (see figure 2.4). Let the beam be focused at a generalised point specified by $\boldsymbol{r}$ which is a distance r from the origin and is located at horizontal and vertical angles given by θ and ϕ as specified in figure 2.4. The unit vector, $\hat{\boldsymbol{r}}$, pointing towards $\boldsymbol{r}$ from the origin is given by

$$\hat{\boldsymbol{r}}(\theta,\phi) = \begin{pmatrix} \cos\phi\cos\theta \\ -\cos\phi\sin\theta \\ \sin\phi \end{pmatrix}. \tag{2.9}$$

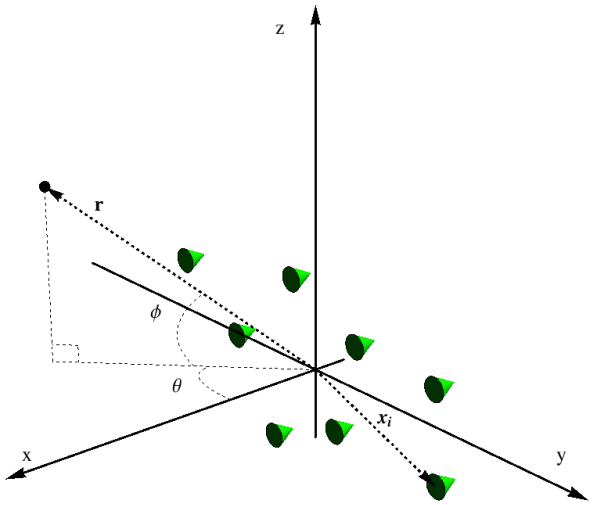

Figure 2.4: The 3D beam forming coordinate system. The positions of the antennas are marked with green cones.

If the position of the i^{th} antenna in the array is given by $\boldsymbol{x_i}$ and the array is receiving radiation with a wavelength λ, then in order to focus the array at point $\boldsymbol{r}$ the phase shift applied to the i^{th} antenna is given by

$$\psi_i(\theta, \phi) = -\frac{2\pi}{\lambda}|r\hat{\boldsymbol{r}} - \boldsymbol{x_i}| \tag{2.10}$$

It is intuitive to see that if a point source were placed at $\boldsymbol{r}$ the signal would be received at each of the antennas with a slightly different phase given by Equation 2.10 (note that $|r\hat{\boldsymbol{r}} - \boldsymbol{x_i}|$ is simply the distance from source to the i^{th} antenna). Therefore applying this phase shift to each antenna signal before summing them together results in constructive interference in the (θ, ϕ) direction. Before being phase shifted and summed together, if one considers a time interval Δt, a Fourier transform is applied to each antenna channel

$$\hat{S}_i^{\text{A}}(\nu) = \int_t^{t+\Delta t} S_i^{\text{A}}(t) e^{2\pi j \nu t} dt \tag{2.11}$$

where S_i^{A} is the complex signal made up of the I and Q components from the i^{th} antenna ($S_i^{\text{A}} = I_i + jQ_i$) and $j = \sqrt{-1}$. The complex signal from the i^{th} antenna in the frequency domain is denoted by $\hat{S}_i^{\text{A}}$. Applying a Fourier transform to each antenna channel allows the phase shifts denoted in Equation 2.10 to be

applied in the frequency domain. On SAMI DBS experiments this is computationally advantageous as one is typically only interested in a small subset of the available ±125 MHz IF spectrum; typically $\nu_{\text{probe}}\pm$ 0.2 MHz where ν_{probe} is the active probing IF frequency. In the frequency domain only the values of interest have to be phase shifted, therefore, when conducting frequency domain phase shifts on SAMI data the computational efficiency is increased by a factor of 625 (relative to a time domain phase shift). The frequency domain synthesised beam signal is given by

$$\hat{S}^{\text{B}}(\Delta\nu,\theta,\phi) = \sum_{i=1}^{N} w_i \hat{S}_i^{\text{A}}(\Delta\nu) e^{j\psi_i(\theta,\phi)} \tag{2.12}$$

where w_i is a complex calibration factor correcting for amplitude and phase imbalances between antenna channel hardware, the sum is over N antennas and $\Delta\nu$ denotes the subset of frequency values included in the receiving beam. To measure the intensity in the (θ,ϕ) direction within the bandwidth $\Delta\nu$, the magnitude of $\hat{S}^{\text{B}}$ is integrated across $\Delta\nu$:

$$I(\Delta\nu,\theta,\phi) = \int_{\Delta\nu} |\hat{S}^{\text{B}}(\nu;\theta,\phi)|^2 \text{d}\nu \tag{2.13}$$

By evaluating I over a range of horizontal and vertical viewing angles a 2D map of intensities, such as that shown at the figure 5.2b, can be plotted.

Erroneously in Equation 2.10 it is assumed that the location of the source is known. However, in the far field ($r >> |\boldsymbol{x_i}|$) the phase is not sensitive to r and much more so to the directionality, $\hat{\boldsymbol{r}}$. Therefore, a meticulous value of r is not necessary for accurate image reconstruction. SAMI is sufficiently far away from the plasma in MAST ($\frac{|\boldsymbol{x_i}|}{r} \sim 0.1$) for the far field approximation to hold. In practice r was estimated using the location of the LCFS. If installed on other experiments where $|\boldsymbol{x_i}| \sim r$, it will be critical to make as good an estimate as possible for r using density profile diagnostics and magnetic equilibria reconstructions.

2.2.2 Beam forming in terms of cross correlations

The intensity distribution derived from beam forming (Equation 2.13) can be rewritten as:

$$
\begin{aligned}
I(\Delta\nu,\theta,\phi) &= \int_{\Delta\nu} \hat{S}^{\mathrm{B}} \hat{S}^{\mathrm{B}^*} d\nu \\
&= \int_{\Delta\nu} \left(\sum_{i=1}^{N} w_i \hat{S}_i^A e^{j\psi} \right) \left(\sum_{i=1}^{N} w_i \hat{S}_i^A e^{j\psi} \right)^* d\nu \\
&= \sum_{i=1}^{N} \hat{\Gamma}_{ii} + \sum_{i=1}^{N-1} \sum_{j=i+1}^{N} \hat{\Gamma}_{ij} e^{j(\psi_i - \psi_j)} + \sum_{i=1}^{N-1} \sum_{j=i+1}^{N} \hat{\Gamma}_{ij}^* e^{-j(\psi_i - \psi_j)}
\end{aligned} \tag{2.14}
$$

where the frequency domain cross-correlation is given by:

$$
\hat{\Gamma}_{ij} = \int_{\Delta\nu} \hat{S}_i^A \hat{S}_j^{A^*} d\nu \tag{2.15}
$$

It is apparent from Equation 2.14 that beam forming, though not equivalent, is similar to the image inversion algorithm used during SAMI's passive operating mode [31, 77].

2.3 Ray and beam-tracing

DBS diagnostics provide turbulence amplitude and velocity measurements at the backscattering location for a particular beam alignment. Backscattering occurs at a location radially shifted outwards from the normal incidence cutoff where Equation 2.4 is satisfied and depends on the density profile and magnetic equilibrium. Therefore, to localise the DBS measurements the results have to be coupled to Thomson Scattering, a Grad-Shafranov magnetic equilibrium solver and a ray or beam-tracing code.

The ray-tracing equations are derived using the lowest order WKB approximation which is valid provided that the characteristic length and temporal scales of the plasma are longer than the wave length and period of the radiation in question. This condition is typically satisfied for radiation in tokamak plasmas where $\omega \sim \omega_{ce}$. For a complete derivation please consult the comprehensive description given in [78]. The resulting equations are as follows:

$$\dot{\boldsymbol{k}} = \frac{\partial D/\partial \boldsymbol{x}}{\partial D/\partial \omega}, \tag{2.16}$$

$$\dot{\boldsymbol{x}} = -\frac{\partial D/\partial \boldsymbol{k}}{\partial D/\partial \omega}, \tag{2.17}$$

$$\dot{\boldsymbol{\omega}} = -\frac{\partial D/\partial t}{\partial D/\partial \omega}, \tag{2.18}$$

where $\mathbf{x}$ is the position vector, D is the dispersion relation, $\mathbf{k}$ is the wave-vector and ω is the frequency of the radiation. Equations 2.16, 2.17 and 2.18 are solved numerically tracing out the path of the ray. Note that the evolution of the amplitude of the ray can only be determined by expanding the WKB solutions to higher order.

For SAMI experiments on MAST the TORBEAM beam-tracing code was used [79]. The beam-tracing approach [80] takes into account diffraction resulting in *ordinary* differential equations allowing a user to calculate the propagation of the beam in a tokamak plasma. The beam-tracing ordinary differential equations are outlined in [79]. For DBS core measurements, accurate beam-tracing is crucial to determine the spatial location of the probed wave-number. In edge measurements, such as SAMI, its importance is reduced as the radial shift outwards from the normal incidence cutoff is small. In addition, one should note that, when using TORBEAM, density was assumed to be constant on flux surfaces. However, it is known that neoclassical effects can change the density on a flux surface leading to up down poloidal asymmetry [81]. This could potentially lead to inaccuracies in the scattering location calculated by TORBEAM.

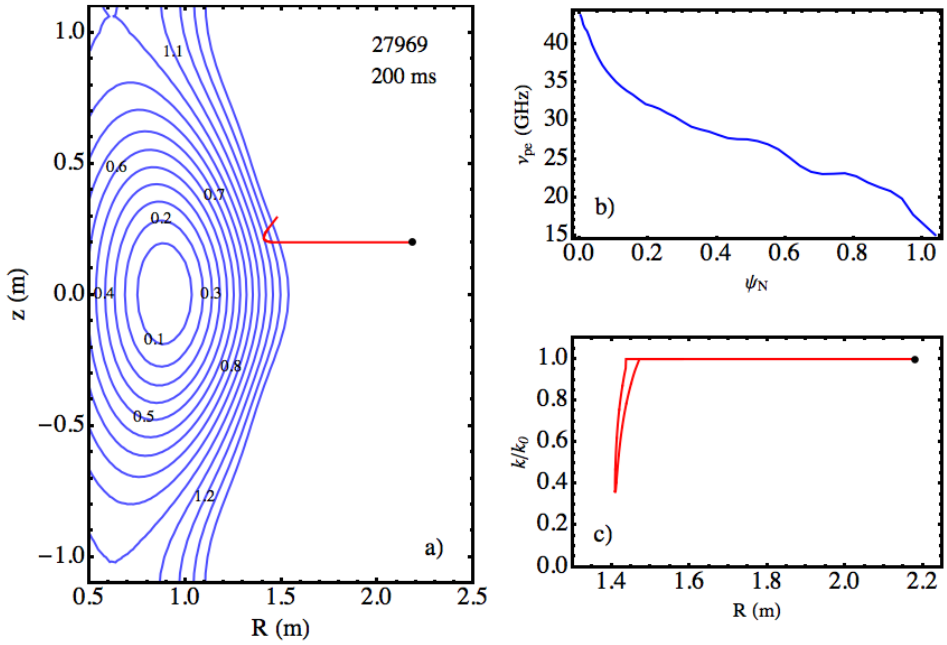

Figure 2.5: TORBEAM code applied 200 ms into MAST shot 27969. (a) A poloidal cross-section showing the path (red continuous line) of a beam launched horizontally from the position of the SAMI antenna array (black dot) towards the low field side of the plasma. Contours of constant normalised magnetic flux are shown in blue. (b) Plasma frequency as a function of normalised magnetic flux. (c) Normalised k as a function of major radius (R) along the path of the beam (k_0 is the wave vector of the beam in vacuum).

Chapter 3

The Synthetic Aperture Microwave Imaging (SAMI) diagnostic

Declaration

Figures 3.1 and 3.7 and the accompanying discussion have been previously published in [34, 35].

3.1 Overview

Doppler backscattering experiments have been developed which steer a narrow probing beam (thereby altering the scattering wave-number) either mechanically [46], or by sweeping in frequency [82]. The backscattered radiation is then received on a single antenna channel (see figure 3.1). However, never before has Doppler backscattering been attempted using a phased array. The Synthetic Aperture Microwave Imaging (SAMI) diagnostic [31, 77, 83] launches a broad ($\pm 40^\circ$ horizontal and vertical) probing beam and the backscattered signal is received on an array of eight antennas (figure 3.1(b)). The phase and amplitude of each channel is digitised enabling SAMI to focus the received beam post shot. This capability is unique to SAMI and is an entirely novel way of conducting DBS experiments. In addition, prior to SAMI only two DBS experiments have been conducted on spherical toka-

maks: one focusing on the edge [59] and one focusing on the core [39]. Spherical tokamaks are not well suited to traditional DBS experiments due to large variations in magnetic pitch leading to poor beam alignment. However, SAMI's 2D nature allows for good beam alignment regardless of pitch variations. In this chapter we give an introduction to this innovative and exciting diagnostic.

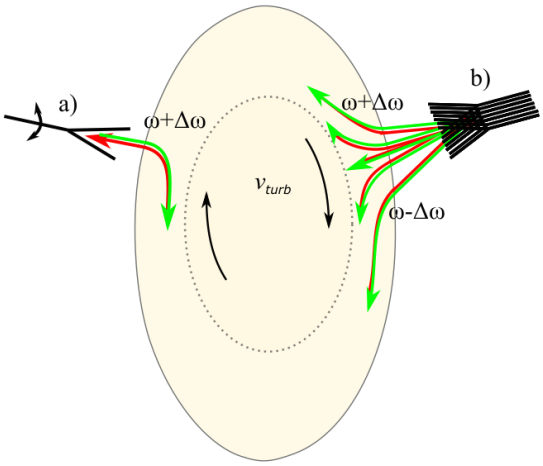

Figure 3.1: Poloidal cross-section cartoon of DBS. The plasma is indicated by the beige region. The incident probing beams are shown in green and the backscattered beams are shown in red. The direction of the turbulence velocity is indicated by the black arrows. The normal incidence O-mode cutoff is indicated by the dotted black line. (a) A steerable conventional single horn DBS experiment. (b) The SAMI diagnostic probes the plasma with a broad beam and receives backscattered radiation from multiple directions and Doppler shifts on eight phase sensitive antennas.

3.2 SAMI hardware

The SAMI hardware is grouped together into five components: the antenna array, the heterodyne receiver, the filter patch panel, the Field Programmable Gate Array (FPGA) and digitisation unit, the Local Oscillator (LO) source and the SAMI PC. (see figure 3.2). In the following section we will consider each of the components listed in figure 3.2 in turn. Here we give a brief overview of the system; if further technical information is desired, please consult the following references [31, 77, 83]. We will concentrate on the diagnostic as it was set-up on MAST. Notable modifi-

cations were made prior to installation on NSTX-U which will be discussed later in section 5.2.

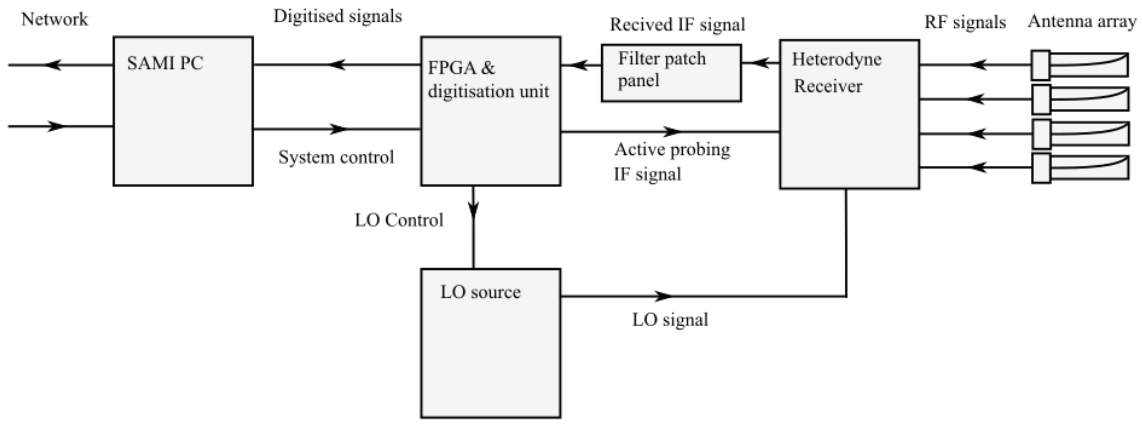

Figure 3.2: Simplified overview of the SAMI system. Arrows indicate the direction of information.

3.2.1 The antenna array, heterodyne receiver and filter patch panel

A schematic of the antenna array, heterodyne receiver and filter patch panel is shown in figure 3.3. Incident microwave radiation (10-34.5 GHz) is received by an array of eight Vivaldi or sinuous antennas (described below in sections 3.2.4 and 3.2.5 respectively). The signals from each antenna are then passed through a set of low noise amplifiers and 90° phase-separated into in-phase (I) and quadrature (Q) components by hybrid couplers. The I and Q components are then heterodyne down-converted by second harmonic mixers before being amplified, low-pass filtered and passed through coaxial cable (coax) to the digitisation unit. The incident local oscillator signal is initially amplified before being passed through two stages of four-way power splitters. The 16 resulting LO signals, attenuated to the same power, are then used to down-convert the I and Q components for each antenna channel.

As well as receiving and digitising passive plasma emission, SAMI also launches two beams of radiation towards the plasma and analyses the backscattered signal. FPGAs provide 10 and 12 MHz square waves which are split into I and Q components before being up-converted by a set of second harmonic mixers. The I and

Q components are then recombined before being amplified and launched into the plasma on two separate antennas.

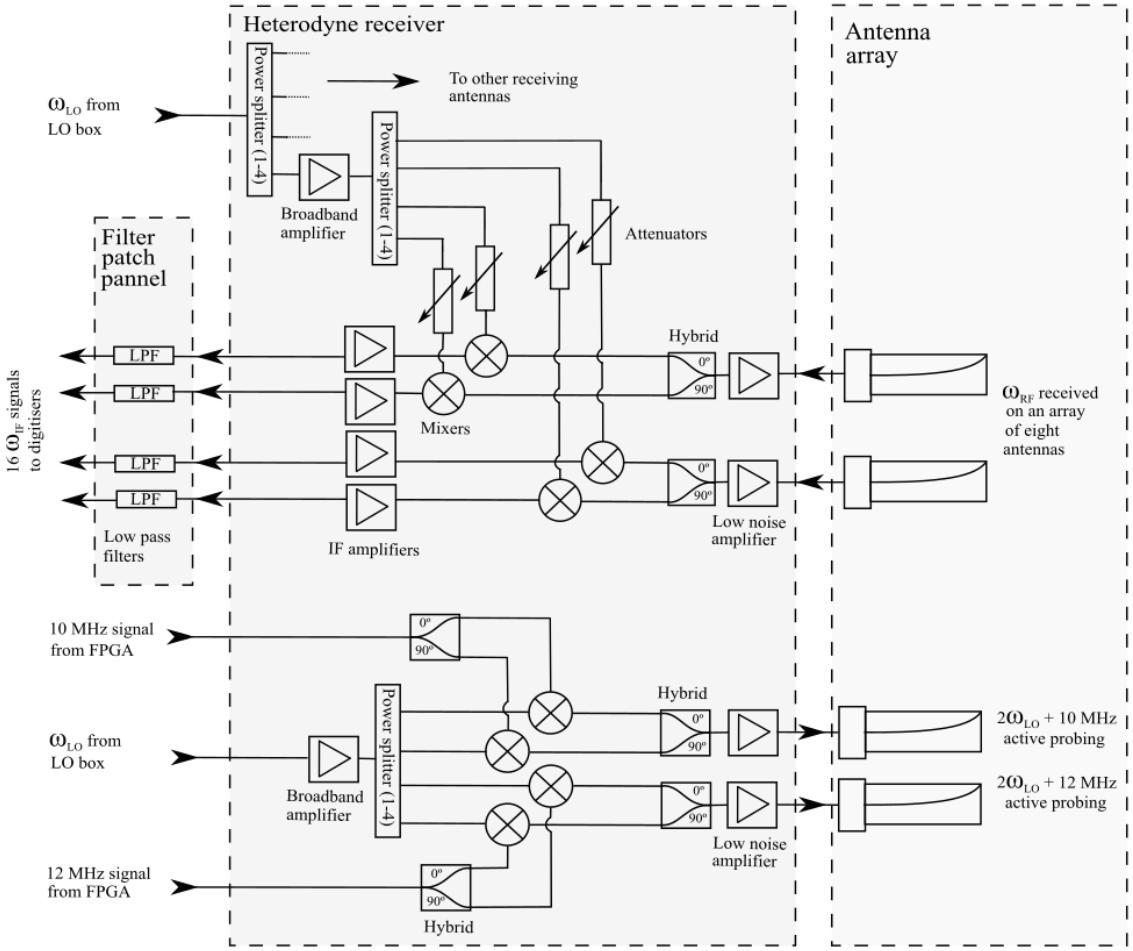

Figure 3.3: A schematic of the antenna array, heterodyne receiver and filter patch panel.

.

3.2.2 The Local Oscillator (LO) source

A schematic of the Local Oscillator (LO) source is shown in figure 3.4. The LO source contains a bank of Dielectric Resonance Oscillators (DROs) which provide LO signals at 5, 5.5, 6, 6.5, 7, 7.5, 8, 8.5, 9, 10.25, 11.25, 12.25, 13.25, 14.25, 15.25 and 17.25 GHz. Each DRO is connected to a 16-to-1 switch via an attenuator and isolator. The switch enables the FPGAs to select a particular LO channel and thereby set the receiving and probing frequencies. The selected LO channel is amplified before being passed through a two-way power splitter giving two identical

outputs. Both outputs are connected to the heterodyne receiver via coax (flexible 18 GHz SMA) and provide the LO signal for receiving, down-conversion and probing, up-conversion as discussed in section 3.2.1.

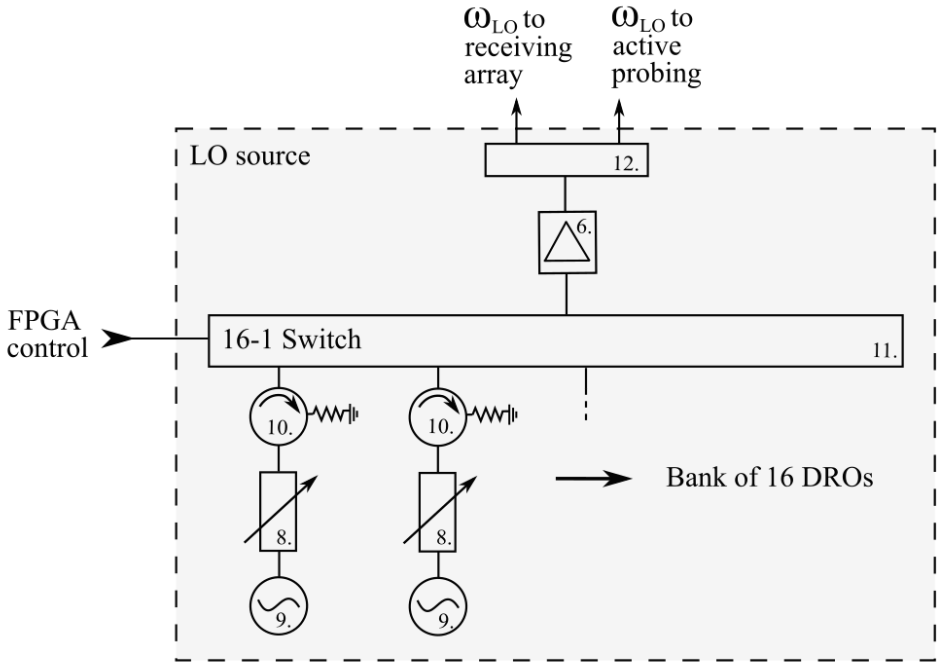

Figure 3.4: A schematic of the antenna array and Local Oscillator (LO) source.

3.2.3 Field Programmable Gate Arrays (FPGAs) and digitisation

SAMI uses FPGAs to control the demanding 14-bit, 250 Mega sample digitisation of 16 channels. FPGAs were chosen for this task as they are extremely flexible and their use incurs a significantly lower capital cost than a traditional digitiser of equivalent specification. Their flexibility has enabled the real time continuous streaming of active probing data to be implemented (limited to 0.5 s previously) via only a firmware upgrade and no additional circuitry. FPGAs also control the downloading of data and transmission over network to a PC where it is saved to disc. The FPGAs also control the frequency switching and produce the IF active probing frequencies. Two FPGA boards are used: one for digitising antenna channels one to four, and another for channels five to eight. Further discussion of the digitisation system is

outside the scope of this thesis but its design and implementation is discussed at length in reference [83].

3.2.4 Vivaldi antipodal antennas

SAMI's antennas have to satisfy a number of constraints: the antennas are required to be broadband (10-34.5 GHz), small enough so that at least 10 can fit into a 15 cm diameter circular port and have a wide field of view (±40 degrees in the vertical and horizontal directions). A design that satisfies all of these constraints is the antipodal Vivaldi antenna. Vivaldi antennas are also inexpensive as they are fabricated using Printed Circuit Board (PCB) technology. Since the Vivaldi antenna was initially proposed by Gibson [84] they have been researched extensively [85–89] and have been utilised in radar, satellite communication and radio astronomy [85]. Simulations have shown that an exponentially tapered flare, $y = c_1 e^{Tx} + c_2$ provides the best wide-band performance [90]. The optimal design parameters for the Vivaldi antenna can be obtained from the literature since, as Maxwell's equations are scale invariant, one only has to decide on the size of the Vivaldi antennas required for the desired frequency band. The width of the antenna approximately defines the lower frequency cut-off for the antenna which is $\sim \frac{\lambda}{2}$. An antenna with a width of 21 mm performs well between 7.5 and 36 GHz encompassing all the SAMI frequency channels.

3.2.5 Sinuous antennas

Another suitable PCB antenna is the sinuous design. Sinuous antennas have a spiral design meaning that their bandwidth is set by the inner and outer termination radius. However, unlike spiral antennas, they couple to linearly polarised radiation enabling them to be dual polarised. Their structure is considered to be composed of "cells", with each cell being a scaled version of its predecessor making sinuous antennas log-periodic. The cells of the sinuous structure are generated from the sinuous curve which is defined by the equation provided by R. H. Du Hamel [91]. The sinuous curve for the p^{th} cell is given by

$$\phi = (-1)^p \alpha \sin\left[\pi \frac{\ln(\frac{r}{\tau^p R_0})}{\ln(\tau)}\right] \tag{3.1}$$

where r and ϕ are the polar coordinates of the curve and R_0 is the radius of the outermost cell. The radius of the p^{th} cell is given by $\tau^p R_0$ and α is the angle through which the sinuous curve is swept. τ and α are constants (consistent with the definition of log-periodic).

In order to create a sinuous antenna, Equation 3.1 is swept through an angle 2δ to generate one sinuous arm. This process is then repeated with a 180° offset creating a dipole. The resulting two-petal, singularly polarised sinuous antenna is shown in figure 3.5. If the same process is repeated with a 90° offset, another dipole can be added creating a four-petal, dual-polarised sinuous antenna. Due to practical constraints connecting a balun to the antenna the SAMI sinuous antennas are made up of two single-polarised sinuous antennas offset at 90° stacked on top of each other. As with the Vivaldi antenna the optimum sinuous design parameters are available in the literature [92–94]: these were then scaled appropriately for the SAMI frequency bandwidth. Figure 3.5 shows the 15 cell design of the sinuous antennas for SAMI: the corresponding design parameters are $\tau = 0.77$, $\alpha = 90°$, $\delta = 22.5°$ and $R_0 = 6.5$ mm.

3.3 Array optimisation

A phased array can never perfectly reconstruct an image as this would require an infinite number of antennas filling an never-ending aperture. However, as we will see, a lot of information can be gained from a finite antenna inversion. A simple 2D example of a finite aperture image inversion (beam-pattern) using the beam forming algorithm is given in figure 3.6. Figure 3.6 shows how the image inversion is affected as the aperture and antenna separation is varied in an array of equally spaced antennas. The near-field response to a point source placed directly in front of the array at a distance of 1 m is shown. Perfect image reconstruction of the source would result in a line at zero degrees (indicated by the red dashed line in figure 3.6). The position of the point source can be accurately measured as this coincides with the maximum amplitude of the image reconstruction. However, in

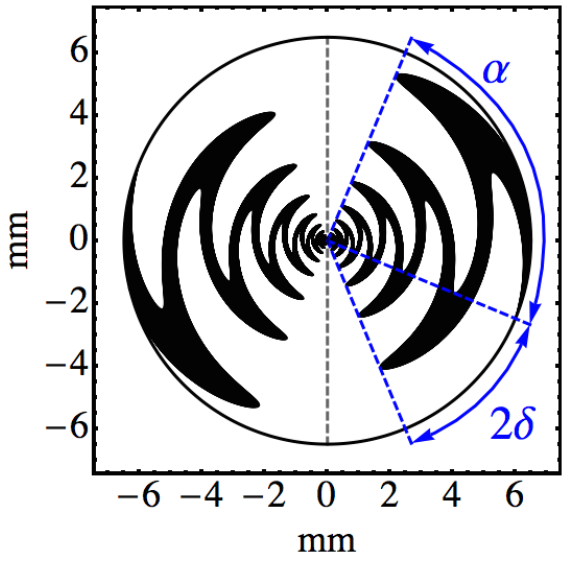

Figure 3.5: SAMI's singularly polarised, 15 cell, two-petal sinuous antenna design viewed from the front. The significance of the α and δ parameters are indicated in blue. The grey vertical dashed line indicates the frequency averaged polarisation along which maximum gain is achieved.

figures 3.6 (a) to (i), the central maximum is comparatively broad relative to the source and accompanied by spurious side-lobes which can confuse interpretation. In addition, when antenna separation is large (a-c) the array pattern repeats itself several times within the $\pm 90^\circ$ viewing range. Figure 3.6 illustrates two effects: the first, is that decreasing the distance between antennas increases the field of view (size of the non-repeated region); the second, is that the width of the central maximum (angular resolution) decreases as the aperture size increases.

Quantitatively, at small incident angles for a source in the far-field radiating at frequency ν, the field of view is given by

$$\theta_{\max} \simeq \frac{c}{\nu b_{\min}} \tag{3.2}$$

where the minimum antenna separation is $b_{\min}$ and c is the speed of light. If the maximum antenna separation in the receiving array is given by $b_{\max}$ then similarly the 3 dB width of the central maximum is given by

$$\theta_{3\mathrm{dB}} \simeq \frac{c}{3\nu b_{\max}} \tag{3.3}$$

In figure 3.6 the receiving antennas are in an equally spaced 1D array for simplicity.

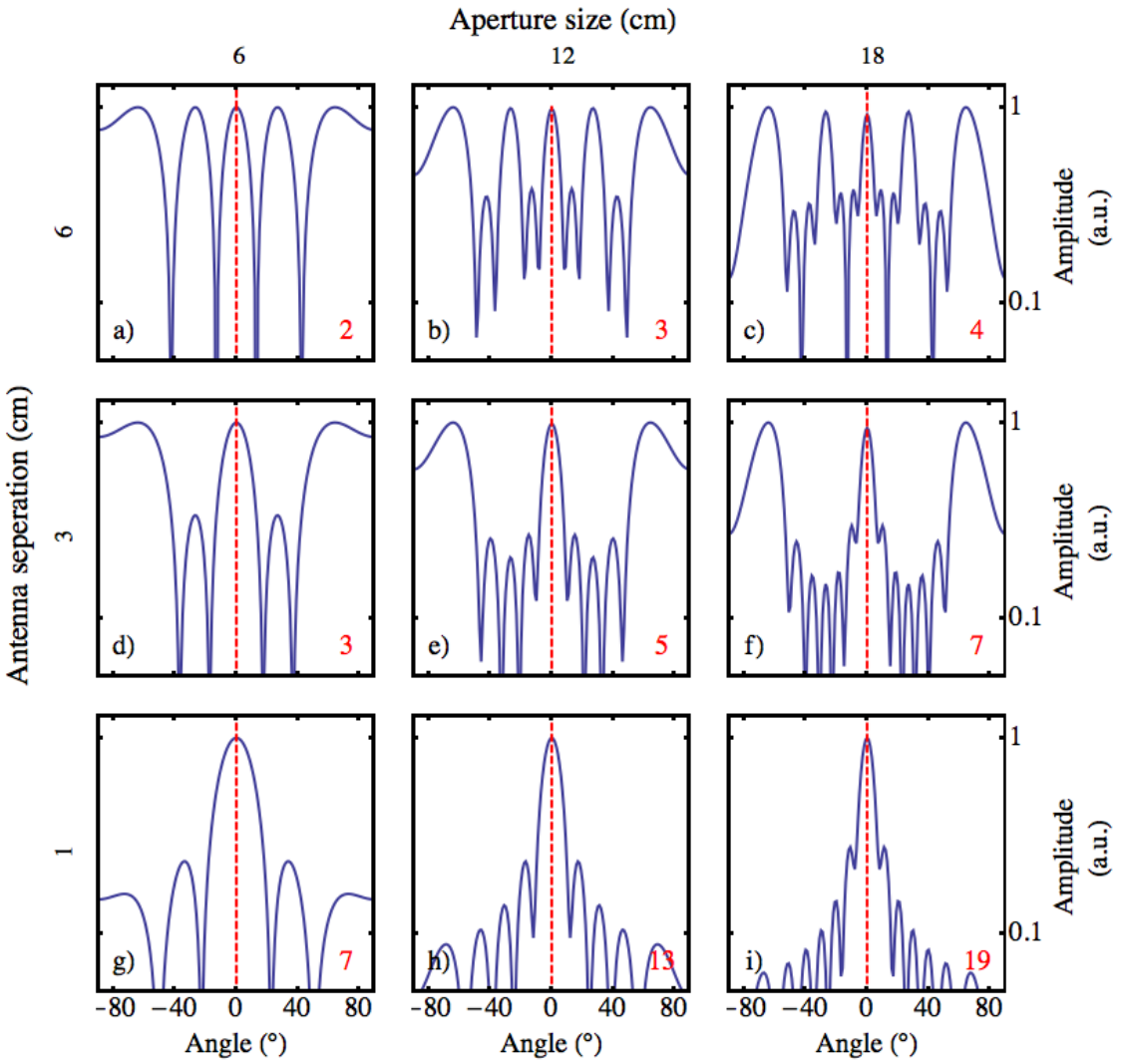

Figure 3.6: The response of a 1D array to a 11 GHz point source placed in the centre of the field of view at a distance of 1 m. The response of nine different arrays are shown (a)-(i) for all combinations of aperture sizes 6, 12, 18 cm and antenna separations 1, 3, 6 cm. The antennas are always equally spaced in the array: as the antenna separation decreases and aperture size increases, more antennas are added to the array. The number of antennas in the array is given by the red number in the bottom right-hand side of each graph.

However, having an array constructed in this way is highly inefficient in terms of side-lobe suppression. Designing an array in order to maximise its efficiency in 2D is an involved process.

The SAMI array installed on MAST was designed using a simulated annealing

antenna placement optimisation strategy, a process based on the analogy of annealing in metallurgy. The performance of the array was reduced to a single parameter, the array factor beam efficiency, which was then maximised. This optimisation method is further outlined in references [31, 95, 96]. The array design that resulted from this process is shown in figure 3.7.

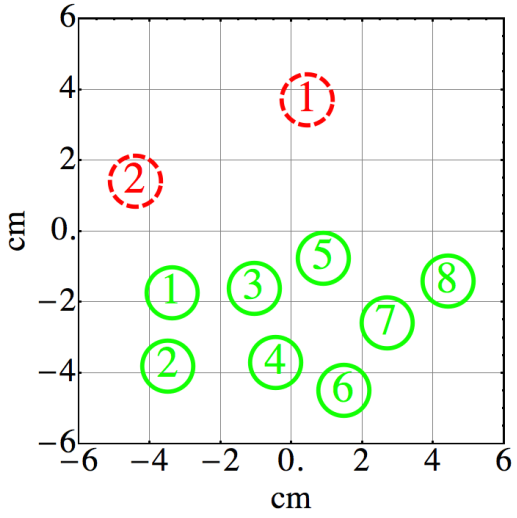

Figure 3.7: The MAST Vivaldi SAMI array configuration. The positions of the two emitting antennas are indicated by red dashed circles and are numbered 1-2. The positions of the eight receiving antennas are indicated by green circles and are numbered 1-8. The array is shown as viewed from the plasma facing side.

3.4 Side-band separation

RF radiation arriving at the SAMI receiving array is heterodyne down-converted using second harmonic mixers. This is done by mixing the RF signals with a local oscillator signal of frequency ω_{LO}. If we consider a single frequency, ω_{RF}, then mixing will result in two frequencies $2\omega_{\mathrm{LO}} + \omega_{\mathrm{RF}}$ and $2\omega_{\mathrm{LO}} - \omega_{\mathrm{RF}}$. Post mixing, signals pass through IF amplifiers, low pass filters and IF coaxial cable to the FPGAs. After these three stages the high frequency component, $2\omega_{\mathrm{LO}} + \omega_{\mathrm{RF}}$, is completely suppressed and only the IF, $2\omega_{\mathrm{LO}} - \omega_{\mathrm{RF}}$, component remains. The signals are digitised at a frequency of 250 Mega samples per second resulting in a Nyquist frequency of 125 MHz. Therefore, for a local oscillator channel of frequency ω_{LO}, data is digitised between $2\omega_{\mathrm{LO}}-$ 125 MHz and $2\omega_{\mathrm{LO}}+$ 125 MHz. Signals with frequency ω_{RF} that are

within the frequency ranges $2\omega_{\mathrm{LO}} - 125$ MHz$< \omega_{\mathrm{RF}} < 2\omega_{\mathrm{LO}}$ and $2\omega_{\mathrm{LO}} < \omega_{\mathrm{RF}} < 2\omega_{\mathrm{LO}} + 125$ MHz are said to be in the lower and upper side-bands respectively.

Let us consider a scenario where two RF signals of equal amplitude are incident on the SAMI antenna array; one in the lower side-band, frequency $2\omega_{\mathrm{LO}} - \delta\omega_{\mathrm{l}}$, phase ϕ_l; the other in the upper side-band, frequency $2\omega_{\mathrm{LO}} + \delta\omega_{\mathrm{u}}$, phase ϕ_{u}. These signals will be amplified and subsequently phase separated by the hybrid couplers; at which point the RF I and Q components can be written as

$$I_{\mathrm{RF}} = A_{\mathrm{I}} \left\{ \cos[(2\omega_{\mathrm{LO}} - \delta\omega_{\mathrm{l}})t + \phi_{\mathrm{l}}] + \cos[(2\omega_{\mathrm{LO}} + \delta\omega_{\mathrm{u}})t + \phi_{\mathrm{u}}] \right\} \tag{3.4}$$

$$Q_{\mathrm{RF}} = A_{\mathrm{Q}} \left\{ \sin[(2\omega_{\mathrm{LO}} - \delta\omega_{\mathrm{l}})t + \phi_{\mathrm{l}}] + \sin[(2\omega_{\mathrm{LO}} + \delta\omega_{\mathrm{u}})t + \phi_{\mathrm{u}}] \right\}. \tag{3.5}$$

where A_{I} and A_{Q} are the amplitudes of the I and Q components respectively. Now let us consider the effect of down-converting these signals. If I_{RF} and Q_{RF} are both multiplied by $\cos(2\omega_{LO})$ and passed through a low pass filter then the resulting IF signals are given by

$$I_{\mathrm{IF}} = \frac{A_{\mathrm{I}}}{2}[\cos(\delta\omega_{\mathrm{l}}t - \phi_{\mathrm{l}}) + \cos(\delta\omega_{\mathrm{u}}t + \phi_{\mathrm{u}})] \tag{3.6}$$

$$Q_{\mathrm{IF}} = \frac{A_{\mathrm{Q}}}{2}[-\sin(\delta\omega_{\mathrm{l}}t - \phi_{\mathrm{l}}) + \sin(\delta\omega_{\mathrm{u}}t + \phi_{\mathrm{u}})]. \tag{3.7}$$

It is clear from Equation 3.6 why I and Q separation is necessary *before* mixing; phases behave oppositely in upper and lower side-bands. In a phase sensitive device this makes phase measurements using only the I component of a dual side-band signal challenging. Digitising both I and Q components enables side-band separation and therefore phase sensitive measurements. If a Hilbert transform is taken of the I and Q signals post mixing then the following results:

$$\hat{I}_{\mathrm{IF}} = \frac{A_{\mathrm{I}}}{2}[\sin(\delta\omega_{\mathrm{l}}t - \phi_{\mathrm{l}}) + \sin(\delta\omega_{\mathrm{u}}t + \phi_{\mathrm{u}})] \tag{3.8}$$

$$\hat{Q}_{\mathrm{IF}} = \frac{A_{\mathrm{Q}}}{2}[\cos(\delta\omega_{\mathrm{l}}t - \phi_{\mathrm{l}}) - \cos(\delta\omega_{\mathrm{u}}t + \phi_{\mathrm{u}}) \tag{3.9}$$

where the hat operator denotes a Hilbert transform (in practice the Hilbert transform is applied post digitisation using software). Using Equations 3.6-3.8 and assuming

that the I and Q amplitudes are the same ($A_{\mathrm{I}} = A_{\mathrm{Q}} = A$), side-band separation can be achieved through the following relations:

$$I_{\mathrm{IF}} - \hat{Q}_{\mathrm{IF}} = A\cos(\delta\omega_{\mathrm{u}}t + \phi_{\mathrm{u}}) \tag{3.10}$$

$$\hat{I}_{\mathrm{IF}} + Q_{\mathrm{IF}} = A\sin(\delta\omega_{\mathrm{u}}t + \phi_{\mathrm{u}}) \tag{3.11}$$

$$I_{\mathrm{IF}} + \hat{Q}_{\mathrm{IF}} = A\cos(\delta\omega_{\mathrm{l}}t - \phi_{\mathrm{l}}) \tag{3.12}$$

$$\hat{I}_{\mathrm{IF}} - Q_{\mathrm{IF}} = A\sin(\delta\omega_{\mathrm{l}}t - \phi_{\mathrm{l}}). \tag{3.13}$$

In practice this process is limited by the phase and amplitude imbalance of the I and Q components. However, these imbalances can be corrected for through calibration allowing for a highly effective side-band separation.

3.5 Polarimetry

The polarisation of radiation incident on an antenna array is often described by set of four "Stokes" parameters [97,98]. For an electromagnetic wave propagating along the z-axis with E-field components in the x and y direction, the Stokes parameters (I, Q, U and V) are related to the x and y electric field components (E_x and E_y) by:

$$I = \langle E_x^2(t)\rangle + \langle E_y^2(t)\rangle \tag{3.14}$$

$$Q = \langle E_x^2(t)\rangle - \langle E_y^2(t)\rangle \tag{3.15}$$

$$U = 2\Re\langle E_x(t)E_y^*(t)\rangle \tag{3.16}$$

$$V = 2\Im\langle E_x(t)E_y^*(t)\rangle. \tag{3.17}$$

where the angled brackets indicate time averaging. Stokes parameters collectively constitute a complete description of polarisation: I is a measure of the total intensity, Q and U represent the linearly polarised components and V represents the circularly polarised component. The degrees of linear, circular and total polarisation are given by:

$$m_l = \frac{\sqrt{Q^2 + U^2}}{I} \tag{3.18}$$

$$m_c = \frac{V}{I} \tag{3.19}$$

$$m_t = \frac{\sqrt{Q^2 + U^2 + V^2}}{I} \tag{3.20}$$

$$\theta = \frac{1}{2}\tan^{-1}\left(\frac{U}{Q}\right) \tag{3.21}$$

respectively where θ gives the angular orientation of the linear polarisation plane. The m_t component will only not equal unity when unpolarised radiation is present (for example thermal radiation).

3.5.1 Linearly polarised antenna array response

Let us consider an array of linearly polarised antennas which lie in the $x-y$ plane and where the i^{th} antenna is orientated at angle ψ_i to the y-axis. If incident radiation has electric field components in the x and y directions and is propagating in the negative z direction, the response of the i^{th} antenna is given by:

$$s_i(t) = E_{x,i}\sin\psi_i + E_{y,i}\cos\psi_i \tag{3.22}$$

If we consider the cross-correlation between antennas ($\Gamma_{ij} = \langle s_i s_j^* \rangle$) then, using Equations 3.14-3.17 we obtain the following:

$$\begin{aligned}\Gamma_{ij} =& \frac{1}{2}[(I_{ij}^v + Q_{ij}^v)\sin\psi_i\sin\psi_j \\ &+ (U_{ij}^v + iV_{ij}^v)\sin\psi_i\cos\psi_j \\ &+ (U_{ij}^v - iV_{ij}^v)\cos\psi_i\sin\psi_j \\ &+ (I_{ij}^v - Q_{ij}^v)\cos\psi_i\cos\psi_j\end{aligned} \tag{3.23}$$

where the subscripts ij and superscript v have been added to the Stokes parameters symbols to indicate that they represent the complex correlated visibilities not simply the intensity of the radiation. It is these visibilities that are required in order to map polarised emission.

For simplicity, let us consider only antennas with angular orientations taking either $\psi_i = 0$ or $\psi_i = 90°$; it is then apparent that, in order to measure I^v_{ij} and Q^v_{ij} along a given baseline, it is necessary to obtain a correlation measurement between two antennas where $\{\psi_i = 0°, \psi_j = 0°\}$, whilst also along the same baseline obtaining the correlation between two antennas where $\{\psi_i = 90°, \psi_j = 90°\}$. Through addition and subtraction of these two results I^v_{ij} and Q^v_{ij} are obtained respectively. Which Stoke visibilities are obtained through which antenna orientation combinations are summarised in Table 3.1. From Table 3.1 it is clear through measuring four combinations of antenna orientations $\{\psi_i = 0°, \psi_j = 0°\}$, $\{\psi_i = 0°, \psi_j = 90°\}$, $\{\psi_i = 90°, \psi_j = 0°\}$ and $\{\psi_i = 90°, \psi_j = 90°\}$ that all four $(I^v_{ij}, Q^v_{ij}, U^v_{ij}, V^v_{ij})$ of the Stokes visibilities can be obtained allowing one to separate the linearly, circularly and unpolarised components of incident radiation.

It is apparent from the above treatment that in order to achieve polarisation separation the array in question must be made up of antennas sensitive to two orthogonal linear polarisations (dual polarised). Therefore, while SAMI's Vivaldi antenna array (section 3.2.4) cannot perform polarisation separation, the sinuous antenna array upgrade (section 3.2.5) enables this significant diagnostic capability.

ψ_i	ψ_j	Stokes visibilities measured
0°	0°	$I^v_{ij} + Q^v_{ij}$
0°	90°	$U^v_{ij} + jV^v_{ij}$
90°	0°	$U^v_{ij} - jV^v_{ij}$
90°	90°	$I^v_{ij} - Q^v_{ij}$

Table 3.1: Which Stoke parameters are measured by which antenna orientation combintations (only 0° and 90° orientations considered).

Chapter 4

Calibration & proof-of-principle experiments

Declaration

Some discussion in this chapter has been previously published in [34, 35].

4.1 Doppler backscattering lab test

Doppler proof-of-principle experiments were conducted in February 2012 and October 2013 to test SAMI's ability to measure the Doppler shift and angular position of a Doppler backscattered signal. In its active probing mode, SAMI launched a probing beam towards a rotating assembly of perforated aluminium corner reflectors (see figure 4.1) located 0.7 m in front of the array where the beam was Doppler backscattered.

SAMI acquired data for 500 ms switching between each frequency channel every 10 µs. Therefore, data saved to disk for each frequency was made up of 10 µs chunks each separated by 150 µs. The first 2 µs of each chunk is discarded to avoid switching noise resulting in 25 ms of data for each frequency channel made up of 3125, 8 µs chunks spread evenly over 500 ms. The active probing beam frequency was $2\omega_{\mathrm{LO}}$ + 10 MHz for each frequency channel respectively.

Figure 4.2 shows the 30 ms moving average of the red and blue Doppler shifted power as a function of time for the 22.5 GHz frequency channel. The blue and red-

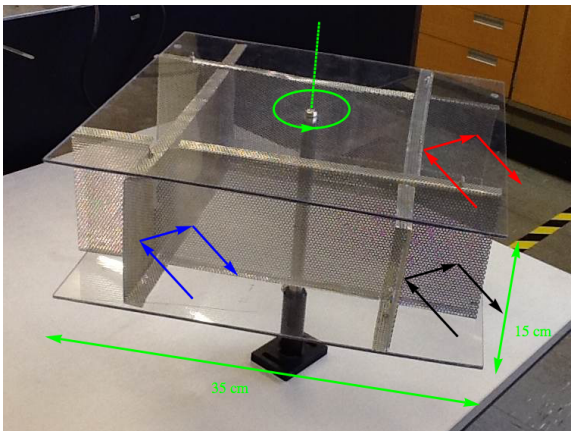

Figure 4.1: Perforated aluminium rotating corner reflector. The dimensional parameters and direction of rotation are indicated by the green arrows. The paths of the blue, red and un-Doppler shifted signals are indicated by the blue, red and black arrows respectively.

shifted IF frequency bands are 10.002-10.005 MHz and 9.996-9.999 MHz respectively. Not all corner reflectors are identical leading to slightly different power profiles. As each corner reflector comes into and disappears from view there will be a spike in the blue and red-shifted power respectively.

The vertical dashed lines in figure 4.2 mark peaks in the red and blue-shifted power as the corner reflector rotates. These peaks are separated by 124 ms corresponding to a rotation period of 496 ms. Other structures visible in the spectrum will result because of reflections in the experimental environment and Doppler-shifted signals off parts of the mesh other than the corners. In order to attain the frequency resolution necessary to resolve the Doppler shift from the rotating mesh the 8 µs data chunks have had to be spliced together. Due to a drift between the active probing and digitisation clocks, which will be discussed further in section 6.6.2, splicing introduces spurious noise leading to the irregular temporal power variation visible in figure 4.2 which cannot be accounted for by the motion of the mesh.

Taking into account the geometry of the mesh and its rotation speed, on the 17 GHz channel, two peaks at ±0.22 kHz should be visible. This is exactly what is observed as shown in figure 4.3a; the red and blue vertical dashed lines indicate where we would expect peaks in the spectrum due to mesh rotation and we can see that two peaks (4.8 dB signal to noise) do occur where expected. The asymmetry around zero can also be explained by clock drift which will be discussed in section 6.6.2.

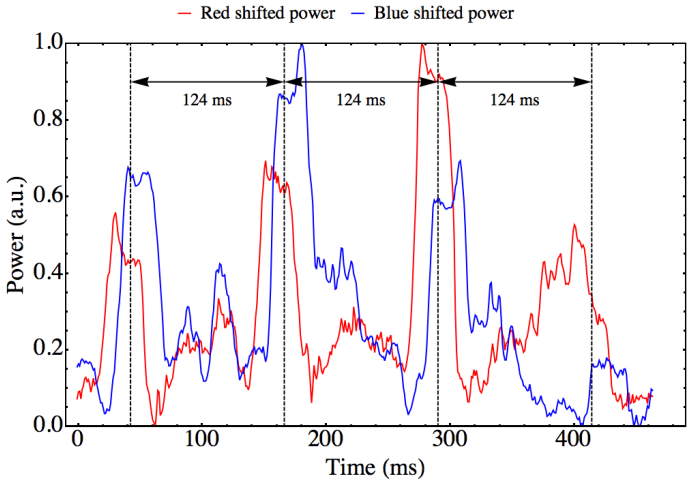

Figure 4.2: 30 ms moving average of red and blue-shifted power indicated by the red and blue lines respectively at 22.5 GHz.

To form figure 4.3(b) the SAMI array was focused, using beam forming, onto each point in a equally spaced 21 by 21 grid spanning ± 40° in the horizontal and vertical viewing directions. This was done using all 25 ms of available 16 GHz data. For each grid point the spectra of the received bean were analysed. The red and blue-shifted power was calculated by summing the amplitudes of the signals between 9.996-9.999 MHz and 10.002-10.005 MHz respectively in the IF. The difference between the blue and red-shifted power is plotted. Net positive and negative regions show where more blue and red-shifted power was present respectively (the colour bar is in arbitrary units). The grey dashed rectangle indicates the position of the rotating mesh which is in excellent agreement with the positions of the red and blue shifted maxima.

Therefore from this experiment we can conclude that SAMI measures Doppler shift to an accuracy of at least ±40 Hz (frequency resolution achieved using 25 ms of data). We also know that SAMI can measure the position of a source reliably. However, for a extensive quantitative analysis of SAMI's spatial accuracy see section 4.2.

4.2 COMPASS area experiments

Experiments were conducted in October 2013 in order to investigate the accuracy and reliability of SAMI's ability to track the location of a point source using the disused COMPASS [99] experimental area at CCFE. This is essentially a large open

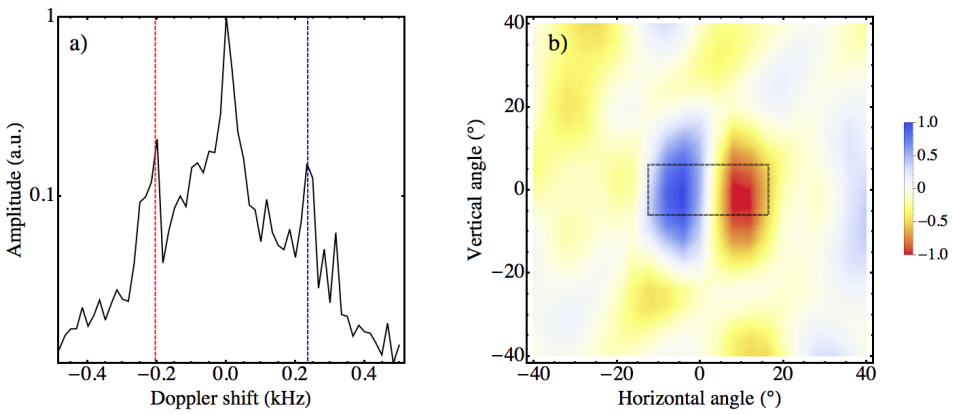

Figure 4.3: (a) IF spectrum of the received 17 GHz Doppler shifted signal. The Doppler shift is given relative to the launched frequency of the probing beam. (b) Doppler shifted power difference at 16 GHz during rotating mesh proof-of-principle experiment. Blue and red indicate more blue than red and more red than blue shifted power respectively. The grey dashed rectangle indicates the position of the rotating mesh.

space, ideal for microwave experiments due to the lack of local reflecting surfaces. A schematic of the experimental set-up is shown in figure 4.4. A signal generator (DC-18 GHz) and horn antenna was used to launch a beam of linearly polarised radiation towards the SAMI Vivaldi array mounted on a rotatable table at a distance of 244 cm. No active probing was used during these experiments and the array set-up used was that shown in figure 3.7. The signal generator was set-up to sweep between −125 MHz and +124 MHz in the IF taking 5 ms to do so for each RF frequency channel up to 18 GHz. This was done over a range of array orientations relative to the launching antenna by rotating the turntable between $\theta = -50$ and $\theta = +50$ in 5° steps.

From these experiments it was found that the array itself is responsible for causing interferences which undermine the accuracy of point source reconstruction. This happens as a result of the Vivaldi's 3D structure causing reflections and refraction within the array. This affects the phase and amplitude response of each individual antenna element non-linearly as a function of incident angle.

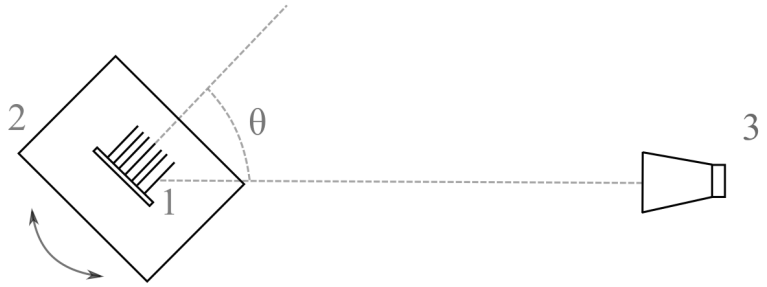

Figure 4.4: Schematic of point tracking COMPASS area experiments. 1) antenna array under test, 2) rotatable table, 3) Flann Microwave dual polarised horn antenna.

4.2.1 Amplitude distortion

In the absence of interference, as the array is rotated we would expect each antenna's amplitude response to decrease uniformly across the IF in accord with the isolated antenna's beam pattern. However, figure 4.5 shows 3D array effects resulting in IF power distortion by as much as 60% (red arrow in figure 4.5) on individual antenna elements as the array is rotated in the horizontal plane.

4.2.2 Phase distortion

The phase distortion from 3D antenna effects becomes apparent if one considers the correlated signal between antenna pairs. If s_i and s_j are the signals from the i^{th} and j^{th} antennas in an array respectively then the correlated signal between the two is given by

$$\Gamma_{ij} \equiv \int s_i s_j^* dt = \langle s_i s_j^* \rangle. \tag{4.1}$$

Figure 4.6(a) shows the phase of the 10 GHz correlation between antenna 4 and antenna 8 as a function of horizontal incidence angle (θ). The green line shows the predicted value of the correlations as a function of θ as calculated from signal path lengths; the red line shows the measured correlation phase. The discrepancy between observed and expected correlated phase values appears to increase at larger values of incident angle. Figure 4.6(b) shows the modulus of the difference between the expected and measured correlated phase averaged over all 28 antenna pair combinations as a function of θ for 10, 11, 12, 13, 14, 15, 16 and 17 GHz frequency channels. This highlights a general trend in the phase error increasing with $|\theta|$ be-

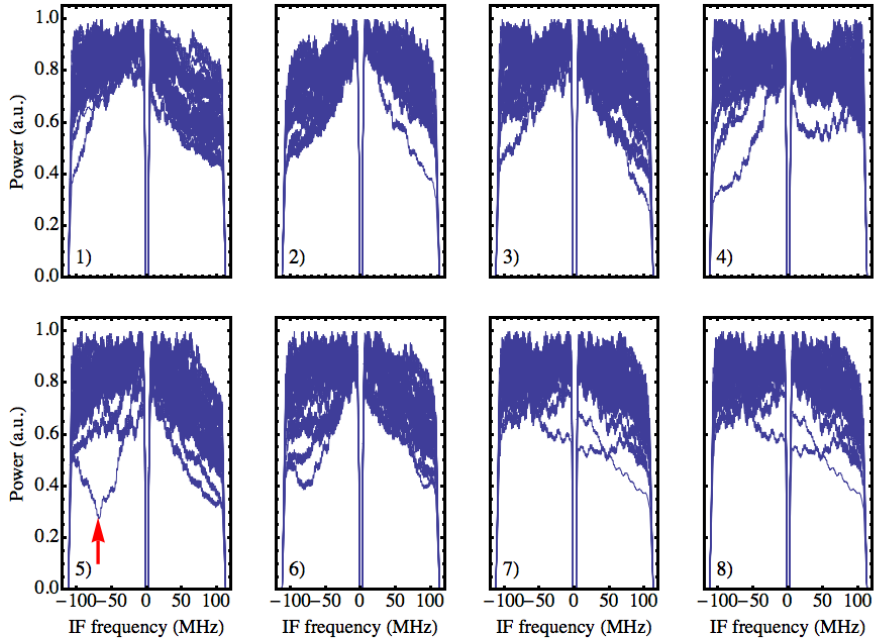

Figure 4.5: Power as a function for IF frequency for each antenna (1-8) in the Vivaldi array where each plot is normalised to its maximum value. For each antenna 21 plots are shown, one for each value of horizontal incidence angle ($\theta = -50^\circ$ to $\theta = -+50^\circ$ in 5° steps).

cause at larger incident angles the antennas shield, reflect and refract the incident beam to a greater degree.

4.2.3 Point source tracking

The ability of the eight antenna Vivaldi array to measure the angular position of the horn antenna source was investigated as a function of horizontal and vertical incidence angles. Different vertical incident angles were achieved by rotating the array by 90° and then moving the turntable on its horizontal axis. As in the amplitude and phase correlation experiments the signal generator was set-up to sweep between -125 MHz and $+124$ MHz in the IF over 5 ms for 10, 11, 12, 13, 14, 15, 16 and 17 GHz RF frequency channels and the turntable was moved between $\theta = -50^\circ$ to $\theta = +50^\circ$ in 5° steps. Results for 11 GHz point tracking are shown in figure 4.7

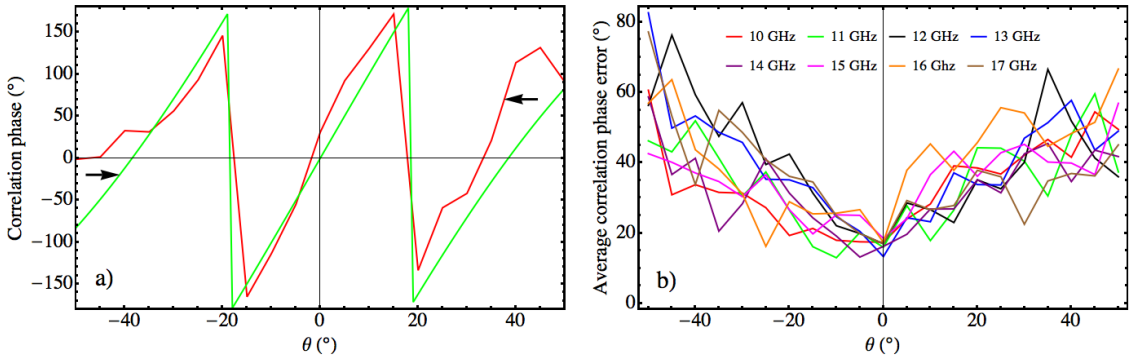

Figure 4.6: (a) The phase of the 10 GHz correlation between antennas 4 and 8 as a function of horizontal incident angle (θ) as observed (red) and as predicted from signal path lengths (green). (b) The modulus of the difference between expected and measured correlated phase averaged over all 28 antenna pair combinations as a function of angle for RF channels 10-17 GHz.

where beam forming image inversion was used and the angular position of the horn antenna was taken to be the position of the largest maxima in the resulting intensity map. The experimental error in the placement of the source was $\pm 0.5°$ in the horizontal and vertical directions.

Figure 4.8(a) shows the horizontal and vertical frequency averaged modulus error (defined as the angular difference between the measured and expected maxima locations) as a function of horizontal and vertical incidence angles. It is apparent, as with the correlated phase, that the error is generally higher at larger $|\theta|$ due to increased reflections and scattering within the array. Figure 4.8(b) shows the horizontal and vertical incidence angle averaged modulus error as a function of frequency channel. Decreased diffraction and increased angular resolution are responsible for the general trend of lower error at higher frequencies: the FWHM of the observed maximum from a point source decreases from 24° to 12°, 10-17 GHz respectively.

The COMPASS area experiments have shown that because the Vivaldi array is 3D, phase and amplitude distortion is introduced as a result of scattering, shadowing and refraction ultimately resulting in a decreased angular accuracy in measuring the position of a source. Therefore, implementing a 2D array is experimentally favourable as will be discussed in section 4.3.

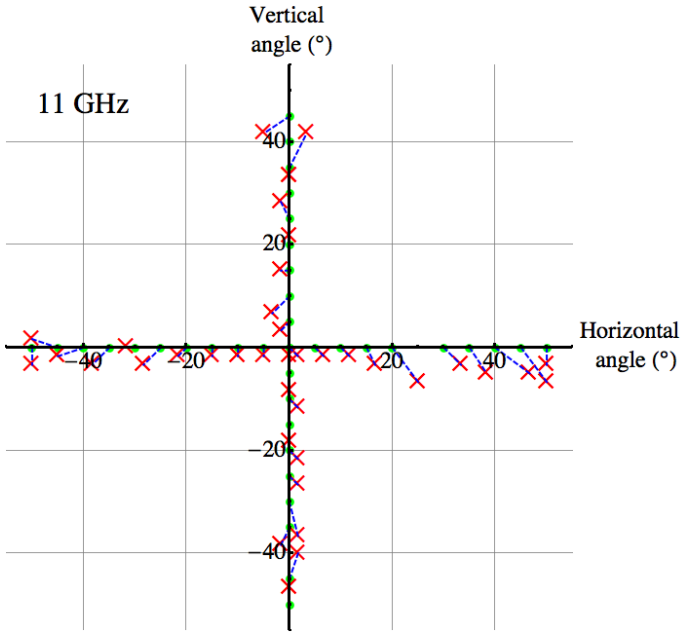

Figure 4.7: Measured (red crosses) and expected (green points) positions of the horn antenna source as a function of horizontal and vertical incidence angles at 11 GHz. The dashed blue lines go between where the source was expected and measured to be for each horizontal and vertical incidence angle.

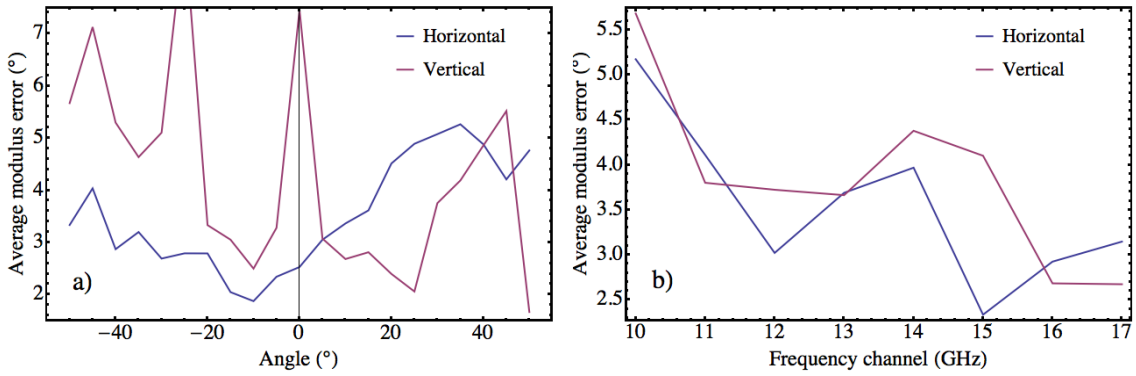

Figure 4.8: (a) Frequency averaged modulus error as a function of horizontal and vertical incidence angles. (b) Incidence angle averaged modulus error as a function of frequency channel for vertical and horizontal incidence angles.

Point tracking accuracy: number of antennas

Using the same data set as in section 4.2.3, we can investigate the capability of the SAMI array to track a point source using different numbers of antennas. Figure 4.9 shows the response of the SAMI array to a point source located at the centre of the field of view. Antenna position one is filled first (see figure 3.7), followed by antenna

position two, and so on. With only one antenna no interference is possible and so no spatial distribution of intensity can be resolved. With two antennas, interference is only possible along a single axis resulting in a symmetrical distribution aligned perpendicular to the single baseline. Only with three antennas is it possible to locate the position of a point source in 2D angular space. Adding additional antennas decreases the size of the central maximum as the array aperture is increased and side-lobes are suppressed.

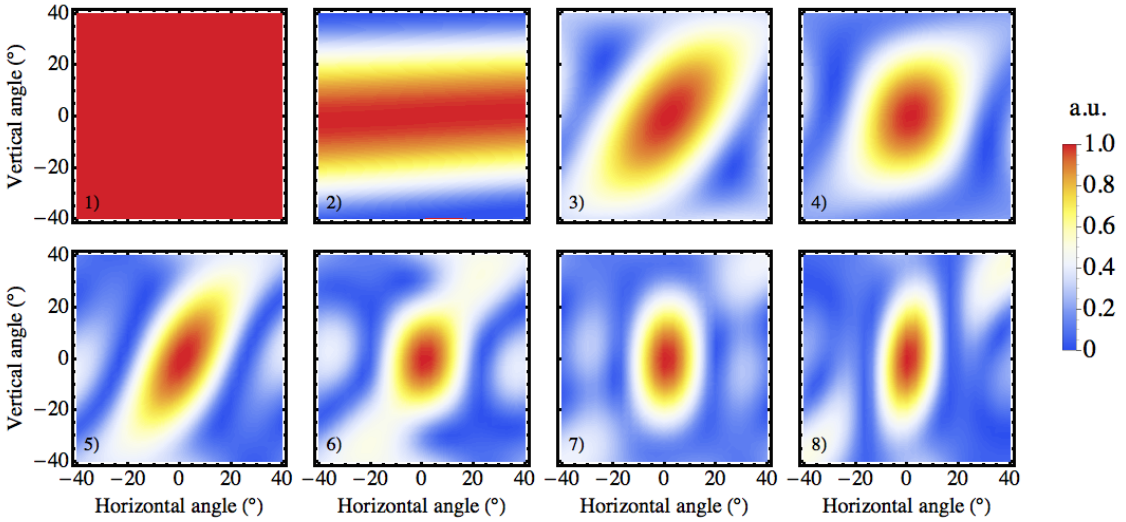

Figure 4.9: Response of the SAMI array to a 11 GHz point sourse located 244 cm from the array in the centre of the feild of view. The response of the SAMI 1-8 antenna array is shown in (1)-(8) respectively.

Figure 4.10 shows how the accuracy of the point source reconstruction varies as a function of number of antennas in the receiving array for a number of different frequency channels. Unsurprisingly, this shows a notable increase in accuracy as antennas are added due to the increasing vertical and horizontal aperture and decreasing side-lobe intensity. There are a large number of variables which have been held constant in this analysis; antenna design, antenna placement, signal to noise, to name a few. Nevertheless, this gives an indication of the potential benefits in terms of point source reconstruction accuracy that could be expected by additional antennas.

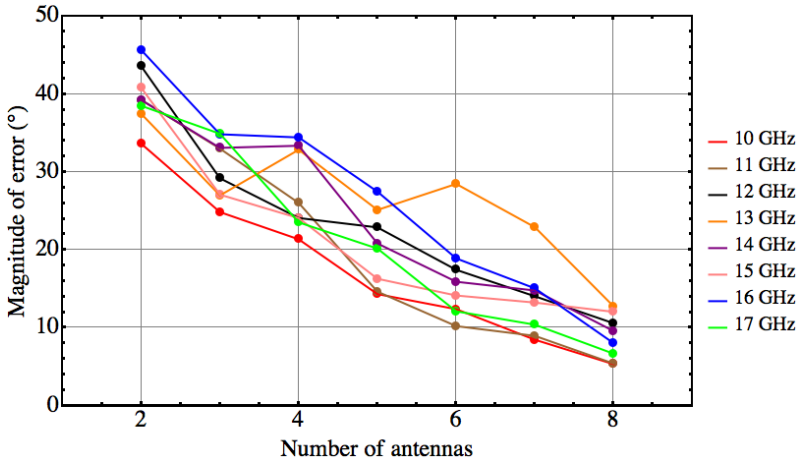

Figure 4.10: The magnitude of the error in point source tracking as a funciton of number of antennas in the receiving SAMI array. Frequency channels 10-17 GHz are shown. The error magnitude has been averaged over all vertical and horizontal incident angles. For computational expidiency only 1 ms of data was used and 1-40 MHz on the IF for each antenna position.

4.3 Sinuous antenna characterisation experiments

All SAMI data acquired during the 8th (M8: September 2011-January 2012) and 9th (M9: May-September 2013) MAST experimental campaigns was done so using the Vivaldi antenna design outlined in section 3.2.4.

Though the Vivaldi antennas have advantages (wide beam pattern and broad bandwidth) they are, as discussed in section 3.5, limited to a single polarisation. Therefore, SAMI was unable to distinguish between O and X-mode radiation during experiments. At SAMI frequencies (10-34.5 GHz) the X and O-mode normal incidence reflection points in the MAST plasma are typically in close proximity leading to error in the observed signal due to interference between the two modes. Without polarisation separation this interference is likely to introduce error in the measured signals. Another disadvantage of the Vivaldi antenna design is its 3D structure. As we saw in section 4.2, when arranged in an array this can lead to reflection and diffraction causing the observed phase and amplitude to vary unpredictably with incidence angle. In addition, relatively high levels of cross-talk can result from the 3D design.

Therefore, at the end of the MAST M9 campaign an alternative antenna design

was sought that had a wide beam pattern, a 2D planer design, was broadband (10-40 GHz) and dual polarised: propitiously, the sinuous antenna fulfils all of these requirements. As mentioned in section 3.2.5, due to practical constraints, instead of a 4 petal dual polarised design, two two-petal, single polarised PCBs were placed on top of one another with a relative axial rotation of 90° within a copper tube support structure (see figure 4.11). The antennas were manufactured in-house by Vladimir Shevchenko and I tested a number of their properties through a series of experiments conducted at the University of York in July 2015. The purpose of these experiments was to test whether the in-house manufactured sinuous antennas had the necessary gain, beam pattern and bandwidth to be used on future SAMI experimental campaigns.

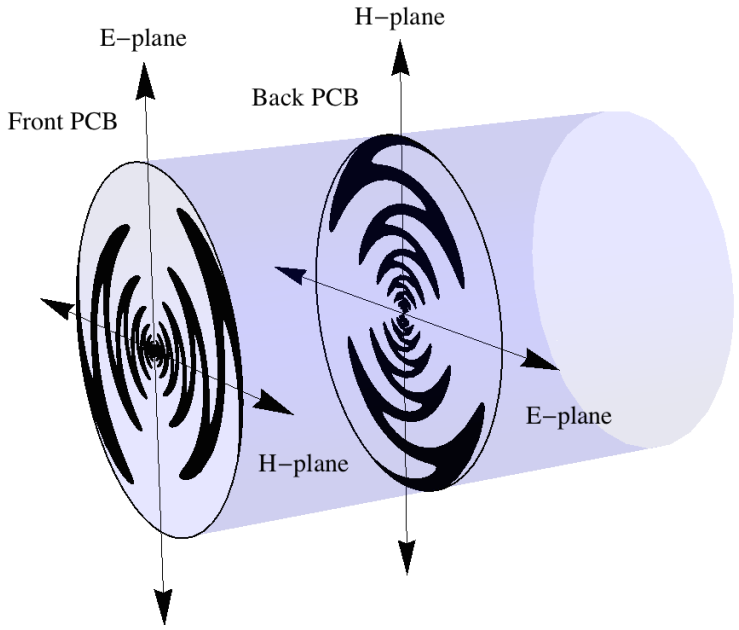

Figure 4.11: 3D schematic of the in-house sinuous antenna design with one PCB mounted behind the other and rotated by 90°. The copper tubing is indicated by blue shading.

A schematic of the set-up used for these experiments is shown in figure 4.12. A Flann Microwave horn antenna was placed 73 cm away from a computer controlled rotating turntable. The antenna under test was mounted on the turntable and both antennas were connected to a DC-26.5 GHz Vector Network Analyser (VNA). The entire apparatus was set-up within an anechoic chamber.

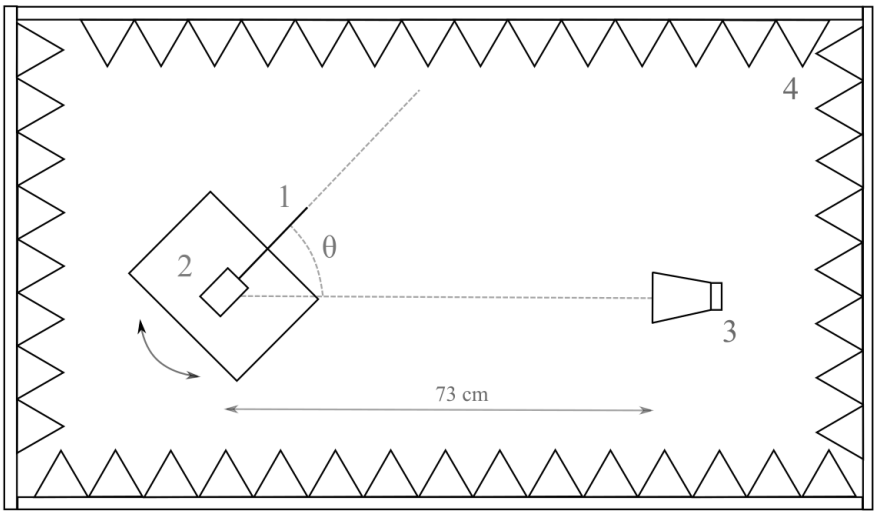

Figure 4.12: Schematic of the set-up used to measure beam patterns at the University of York. The equipment shown is as follows: 1) antenna under test, 2) computer controlled turntable, 3) Flann Microwave dual polarised horn antenna, 4) Microwave absorber.

Initially, in order to test the environment, E and H-plane beam patterns of a second Flann antenna identical to the launching antenna were obtained (the E-plane is the plane parallel to the antenna polarisation and the H-plane is the plane perpendicular to the antenna polarisation). The Flann antennas have a known beam pattern (specified by the manufacturer), therefore any discrepancy from the known pattern indicates that spurious reflections are present in the environment. However, the beam pattern was found to be in good agreement with the known values and so I could be confident that the anechoic chamber provided a reflection free environment for me to conduct further experiments.

Figures 4.13(a)and 4.13(c) show H-plane beam pattern measurements for an isolated (opposed to being in an array) Vivaldi and an isolated back PCB of a sinuous antenna respectively. Figures 4.13(b) and 4.13(d) show H-plane beam patten measurements for a Vivaldi antenna and the back PCB of a sinuous antenna in an array (position two of the array configuration shown in figure 3.7 was used). All beam patterns are normalised to the peak power received during the initial Flann beam pattern experiment and are shown between 5-26.5 GHz and from $\theta = -90°$ to $+90°$. In figures 4.13(a)-(d) a significant amount of noise is present in the beam pattern above 18 GHz. This is because unfortunately, when the data was acquired

a high frequency (40 GHz) coaxial cable with SMK 2.92 connectors to connect the VNA to the launching antenna was not available. Therefore, a lower frequency cable with SMA connectors (18 GHz) was used.

In figures 4.13(a)and 4.13(c) we can see that, for both the Vivaldi and sinuous antennas, the beam pattern is relatively flat within the SAMI experimental field of view ($\pm 40°$). H-plane measurements averaged between 10 and 18 GHz show that the power drop between $\theta = +40°$ and $\theta = 0°$ is 3.2 dB and 3.6 dB for the Vivaldi and sinuous antennas respectively. The corresponding numbers for E-plane are 7.9 dB and 4.2 dB for the Vivaldi and sinuous antennas respectively. The sinuous antennas under test were found to be lower gain overall than the Vivaldi antennas: averaged between $\pm 40°$ and 10-18 GHz the sinuous antennas were found to be 4.5 dB and 3.1 dB lower gain in H and E-planes respectively.

If one compares figures 4.13(a)and 4.13(b) it is apparent that the presence of the other antennas in the Vivaldi array distorts the beam pattern. The 3D geometry of the Vivaldi antennas leads to interference and scattering within the array. Comparing figures 4.13(c) and 4.13(d) we see that by switching to sinuous antennas the distortion caused by the array can be reduced. The modulus of the power difference averaged over the region $\pm 40°$, 10-18 GHz between an antenna being in isolation and in an array is 1.4 dB and 1.0 dB for the Vivaldi and sinuous antennas respectively.

Using the anechoic chamber, I also took cross-talk measurements between different elements in the Vivaldi and sinuous arrays. Figure 4.14 shows cross-talk measurements (10-18 GHz) between two Vivaldi antennas, two front sinuous PCBs and two back sinuous PCBs. All measurements were taken between positions one and two in the array (see figure 3.7). Figure 4.14 shows that cross-talk levels on both sinuous PCBs are lower than that of the Vivaldis across the whole of the frequency range shown. Averaged between 10-18GHz the sinuous back and front PCBs have 13.2 dB and 12.4 dB lower levels of cross-talk than the Vivaldis respectively.

4.3.1 Sinuous characterisation conclusions

The aim of the sinuous antenna characterisation experiments were to test the suitability of the sinuous antennas as a replacement for the Vivaldi antennas in the SAMI receiving array. It was hoped that the sinuous antennas would not only be broad-

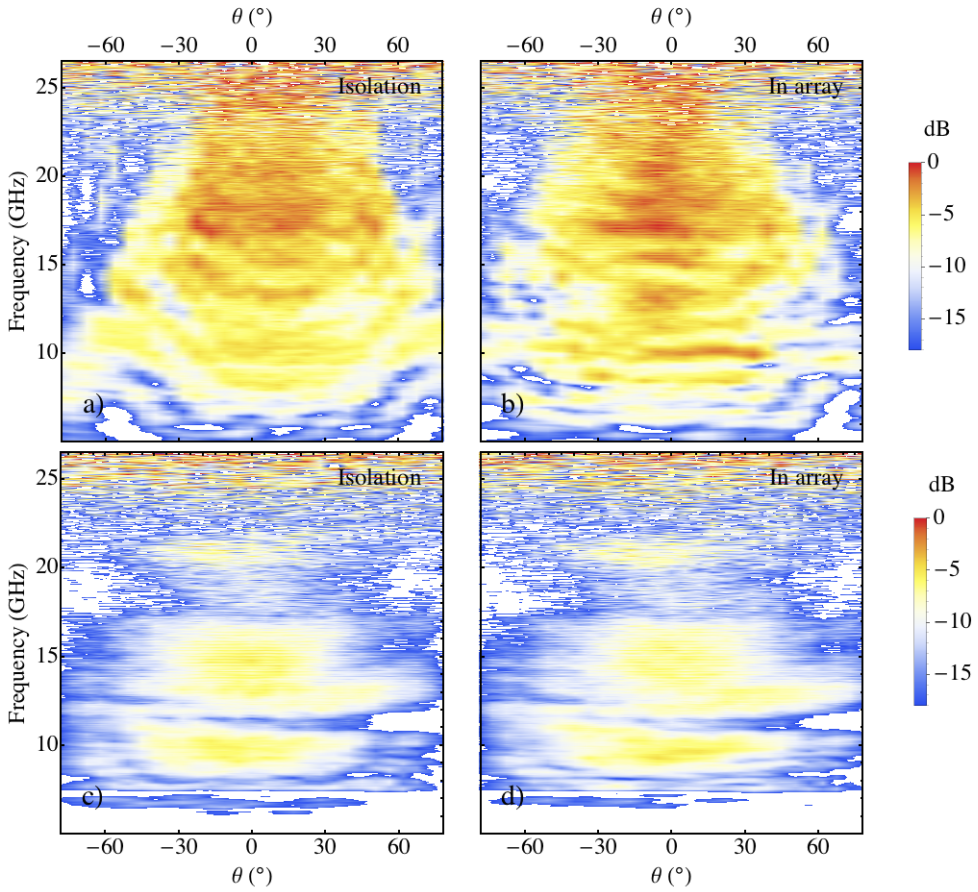

Figure 4.13: The measured power as a function of angle and frequency for the H-plane of the: (a) Vivaldi antenna in isolation, (b) Vivaldi antenna in an array, (c) back PCB sinuous antenna in isolation, (d) back PCB sinuous antenna in an array. All images are normalised to the same value.

band and wide angled, but also have low levels of cross-talk, operate on two different polarisations and reduce 3D array scattering effects. In the following discussion we will only be referring to angles within the SAMI field of view $-40^\circ < \theta < +40^\circ$ and within the frequency range 10 GHz$< \nu <$ 18 GHz (one cannot draw reliable conclusions from data above 18 GHz due to high noise levels).

Consistent with the sinuous literature [92–94] the in-house manufactured antennas were found to be broadband and have a wide antenna gain pattern. Though the sinuous antennas were found to have lower gain than Vivaldis (3.8 dB on average), this is acceptable and can be compensated for by introducing extra gain using the ADCs (up to 6 dB). The sinuous antennas were found to lessen the distortion of the beam pattern caused by in-array scattering and significantly reduce cross-talk.

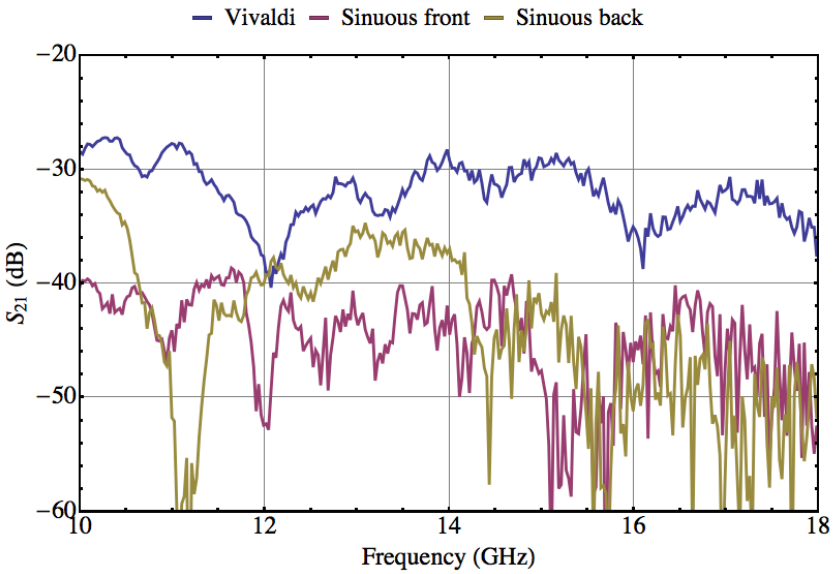

Figure 4.14: Cross-talk levels between two Vivaldi antennas (blue), two sinuous front PCBs (purple) and two back sinuous PCBs (brown). The two antennas were placed is receiving antennas positions one and two in the array design outlined in figure 3.7

Therefore, within the angular and frequency range specified above the sinuous antennas are suitable for deployment on future SAMI experiments. However, to test suitability above 18 GHz further experiments will have to be conducted.

Chapter 5

SAMI Installation

Declaration

Figures 5.2, 5.3 and 5.4 and the accompanying discussion have been previously published in [34, 35, 100].

5.1 Installation on MAST

As already discussed in section 4.3, SAMI was installed on MAST during the 8th (M8: September 2011 - January 2012) and 9th (M9: May-September 2013) MAST experimental campaigns. The SAMI array was installed in a 15 cm diameter port in sector seven, 20.3 cm above the mid-plane at a major radius of 210.4 cm. Figure 5.1 shows the SAMI array, and heterodyne receiver installed on the MAST vessel. In the following section we give a brief overview of SAMI's installation on MAST; for a more in-depth description please consult [77].

Figures 5.2(a)and (b) show SAMI's view of the MAST plasma. The entire vertical extent of the MAST plasma is visible apart from the top $\sim 20^{\circ}$ which is obscured from view by a poloidal field coil. Figure 5.2(b) shows the 16 GHz beam-formed image inversion of a synthetic point source whose location is indicated by the red dot in figure 5.2(a). We can see that 16 GHz probing gives us a central maximum with a Full Width Half Maximuma (FWHM) of 14.9° and 30.1° in the horizontal and vertical directions respectively. The maximum and average side-lobe levels with respect to the central maxima are -2.7 and -6.4 dB respectively. This is very dif-

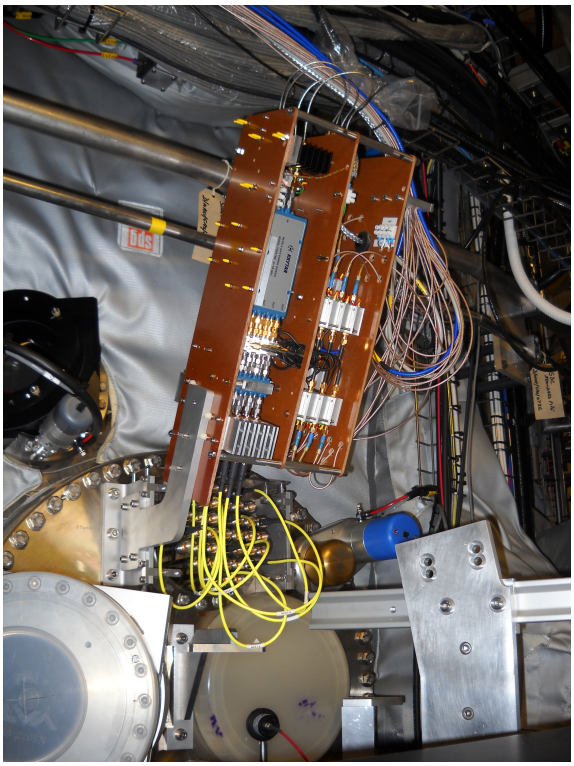

Figure 5.1: The SAMI array and heterodyne receiver mounted on the MAST vacuum vessel [31].

ferent from the beams typically used on conventional DBS experiments which use a focused beam (divergence $\sim$1°) with minimal side-lobes. When considering SAMI data, as side-lobes can be as high as 50% of maximum, they will have a significant effect on plasma data and will have to be considered carefully when interpreting results. This will be discussed further in Chapters 6 and 8.

One can see from figure 5.3 that SAMI primarily probes the edge region of the MAST plasma and that, like most spherical tokamaks, the MAST plasma is overdense ($\nu_{pe} > \nu_{ce}$). This is advantageous for DBS experiments as electron cyclotron resonances, where the probing beam can be absorbed, are easily avoided. In overdense plasmas, electron thermal emission results in electron Bernstein waves (EBWs) which can mode convert into O and X-mode radiation at the plasma edge. This mode converted emission is the subject of extensive passive emission studies using SAMI [31, 77, 102, 103]. The average separation of the O-mode normal incidence cutoffs shown in figure 5.3 are 1.5 and 0.1 cm for L and H-mode respectively. The average distance between the O and X-mode normal incidence cutoffs is 3 and 0.3 cm

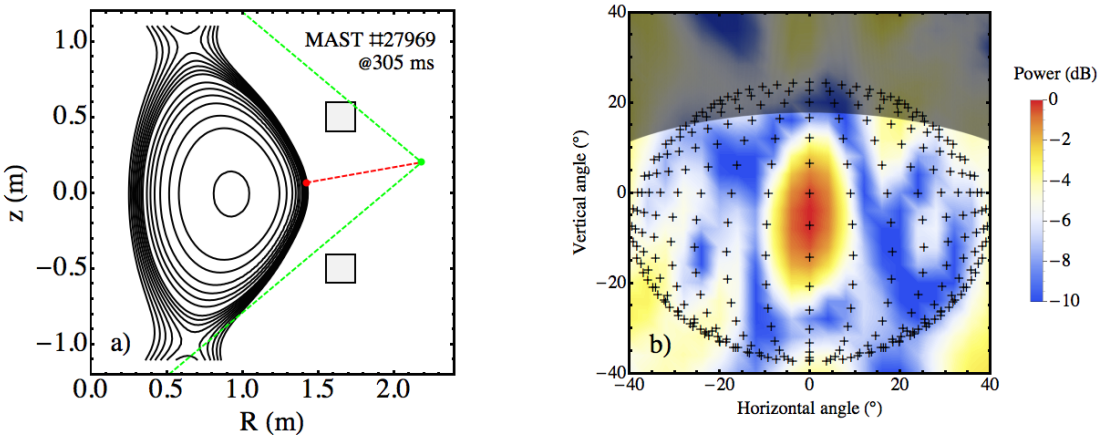

Figure 5.2: (a) Polodial cross-section of the SAMI installation on MAST at 305 ms into shot 27969. Normal incidence O-mode plasma density cutoff surfaces are plotted in black and the upper and lower poloidal field coils are indicated by black squares (on MAST the poloidal field coils are located inside the vacuum vessel). The vertical SAMI field of view (±40°) is indicated by the green dashed lines. The position of the SAMI array is marked with a green dot. The position of the test source is shown by a red dot. The test source and the SAMI array are connected by a red dashed line. The normal incidence cutoff surfaces were calculated using data from the MAST TS system and EFIT [101]. (b) Normalised intensity of the SAMI point spread function at 16 GHz in image coordinates. The position of the normal incidence 16 GHz O-mode cutoff surface is indicated by black crosses. The dark region at the top of the plot shows the field of view which is obscured by the upper poloidal field coil.

for L and H-mode respectively.

Figures 5.4(a)and (b) show the distribution of $k_{\|}$ and $k_{\perp}$ values respectively as a function of probing orientation that are accessible at 16 GHz, 230 ms into MAST shot 27969 calculated using TORBEAM. Doppler backscattering is most efficient when the incident beam is aligned perpendicular to the magnetic field at the scattering location (along $k_{\|} = 0$ in figure 7(a)). We can see from figure 5.4(b) that many values of $K_{\perp}$ (via Equation 2.4) can be measured simultaneously using a 2D DBS device although, unlike steerable DBS systems where the launching antenna is also the

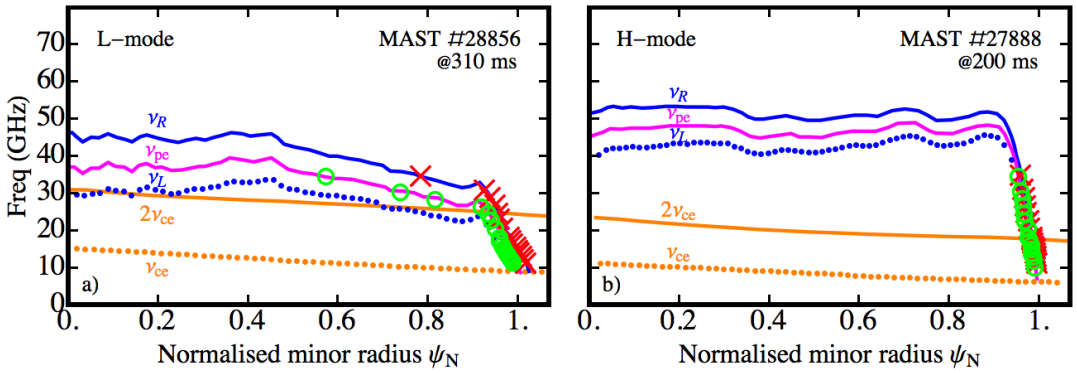

Figure 5.3: Normal incidence cutoffs for two MAST shots: (a) 28856 at 310 ms (L-mode) and (b) 27888 at 200 ms (H-mode). Blue continuous and dotted lines indicate the normal incidence X-mode right-hand (ν_R) and left-hand (ν_L) circularly polarised desnsity cutoffs respectively. The magenta line indicates the plasma frequency cut-off (ν_{pe}). The dotted and continuous orange lines mark the first (ν_{ce}) and second ($2\nu_{ce}$) electron cyclotron harmonics respectively. The green circles mark the positions of the normal incidence O-mode cutoffs for each of the SAMI frequency channels. The red crosses indicate the locations of the Normal Incidence (NI) right-hand circularly polarised cutoffs for each of the SAMI frequency channels. The density profile data is from the MAST 130 point Thomson Scattering (TS) system [19].

.

receiving antenna (monostatic), in its current configuration SAMI has been unable to measure K-spectra.

5.2 Installation on NSTX-U

After the M9 campaign MAST entered an extended shut-down period to allow for significant upgrade work to take place (MAST-U). In order to avoid any delay in SAMI's development a collaboration with the Princeton Plasma Physics Laboratory (PPPL) to install SAMI on NSTX-U was initiated. SAMI was shipped to PPPL in March 2014 and was tested and installed during trips to Princeton in March-April 2014, November 2015 and March 2016.

SAMI was installed on NSTX-U in bay I, on mid-plane at a major radius of

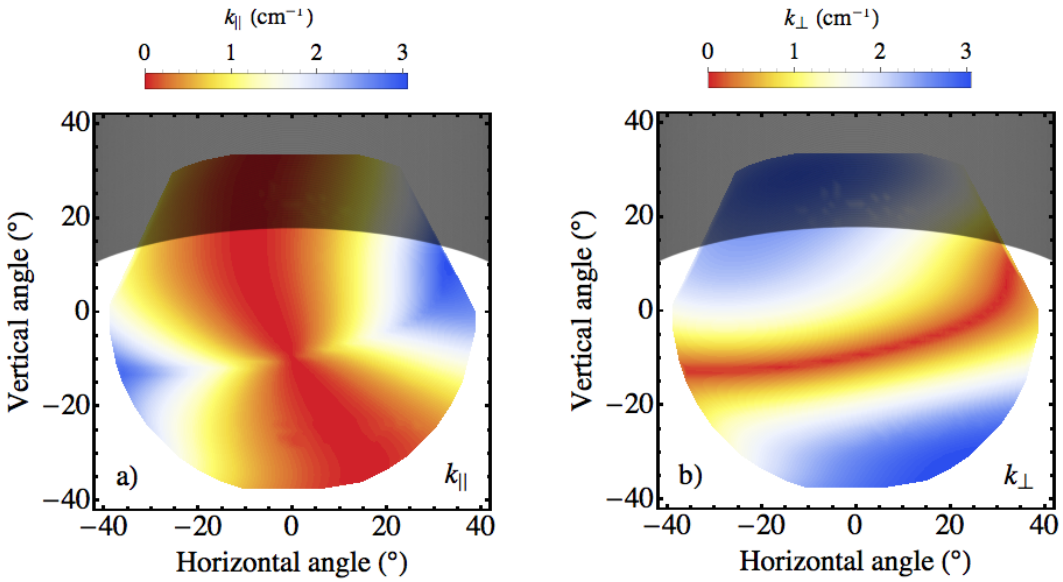

Figure 5.4: (a) and (b) show the $k_{\parallel}$ and $k_{\perp}$ values of the probing beam at the scattering location for 16 GHz probing as a function of vertical and horizontal viewing angles respectively. Calculated using the beam-tracing code TORBEAM and Thomson scattering n_e profile data 230 ms into MAST shot 27969. The dark region at the top of the plots shows the field of view which is obscured by the upper poloidal field coil.

1.96 m. Figures 5.5(a)and (b) show SAMI's view of the NSTX-U plasma. Due to its tightly fitted vacuum vessel, SAMI was mounted much closer to the plasma on NSTX-U (∼45 cm) than on MAST (∼77 cm). In Figure 5.5(a) we can see that on NSTX-U, SAMI's entire vertical field of view is taken up by the plasma. In contrast to MAST, as the poloidal field coils on NSTX-U are mounted outside the vacuum vessel, SAMI's view of the plasma is completely unobscured. The advantages and disadvantages of SAMI's close proximity to the plasma on NSTX-U will be discussed in chapter 7.

Considering figure 5.6, it is apparent that on NSTX-U SAMI primarily probes the edge region of the plasma as was the case on MAST. However, the H-mode pedestal is notably higher on NSTX-U confining the SAMI probing region to the lower half of the edge transport barrier. The average separation of the O-mode normal incidence cutoffs shown in figure 5.6 are 1.5 and 0.1 cm for L and H-mode respectively. The average distance between the O and X-mode normal incidence

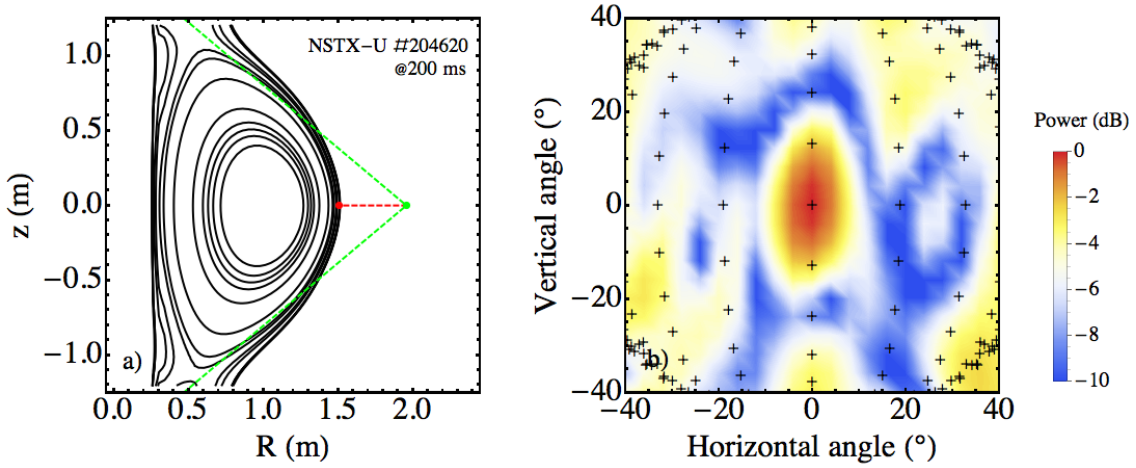

Figure 5.5: (a) Polodial cross-section of the SAMI installation on NSTX-U 200 ms into shot 204620. Normal incidence O-mode plasma density cutoff surfaces are plotted in black. The vertical SAMI field of view (±40°) is indicated by the green dashed lines. The position of the SAMI array is marked with a green dot. The position of the test source is shown by a red dot. The test source and the SAMI array are connected by a red dashed line. (b) Normalised intensity of the SAMI point spread function at 16 GHz in image coordinates. The position of the normal incidence 16 GHz O-mode cutoff surface is indicated by black crosses.

cutoffs is 5 and 0.6 cm for L and H-mode respectively.

Following SAMI's installation on NSTX-U, a number of upgrades are planned. One such upgrade is to change the receiving antennas from Vivaldi antennas to sinuous antennas. Sinuous antennas have many advantages over Vivaldi antennas (discussed in Chapters 3 and 4 above), the main of which is their dual polarisation capability. The SAMI hardware is limited to digitising I and Q components from a maximum of eight antenna channels. Therefore, only a single polarisation can be sampled at a time. However, separation can still be achieved through fast switching between orthogonal antenna polarisations. Switching between four relative polarisations ([0°,0°],[0°,90°],[90°,0°],[90°,90°]) for a particular antenna pair is necessary in order to achieve polarisation separation, as outlined in section 3.5. In order to achieve this in practice on NSTX-U, eight fast two-to-one switches (PMI: P2T-500M40G-60-R-55-292FF) are to be fitted in front of the low noise amplifiers in the heterodyne receiver. Two high frequency coax cables will then go from each switch to each sinuous antenna with the two cables attached to each of the antenna's

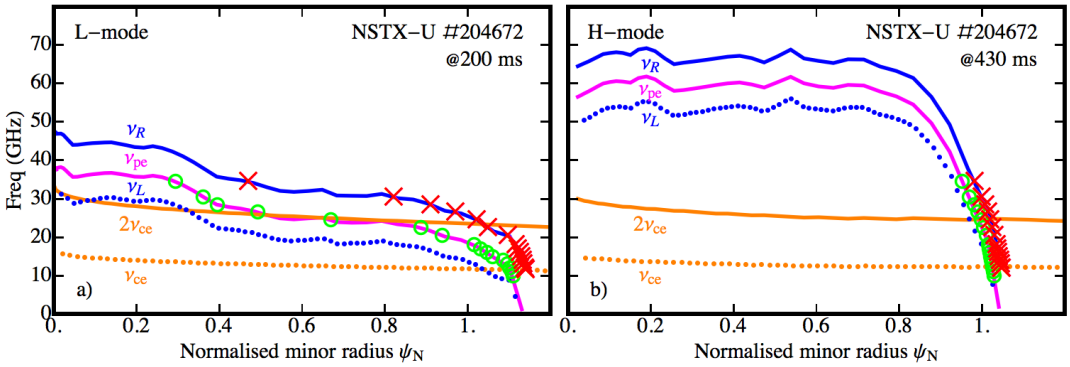

Figure 5.6: Normal incidence cutoffs for two NSTX-U shots: (a) 204672 at 200 ms (L-mode) and (b) at 430 ms (H-mode). Blue continuous and dotted lines indicate the normal incidence X-mode right-hand (ν_R) and left-hand (ν_L) circularly polarised density cutoffs respectively. The magenta line indicates the plasma frequency cut-off (ν_{pe}). The dotted and continuous orange lines mark the first (ν_{ce}) and second ($2\nu_{ce}$) electron cyclotron harmonics respectively. The green circles mark the positions of the normal incidence O-mode cutoffs for each of the SAMI frequency channels. The red crosses indicate the locations of the Normal Incidence (NI) right-hand circularly polarised cutoffs for each of the SAMI frequency channels. Magnetic field and electron density information is provided by the EFIT and NSTX-U Thomson scattering system [104, 105] respectively.

orthogonal polarisation outputs.

In addition to using sinuous antennas, the array layout will also be changed from that shown in figure 3.7 to the symmetrical circular design shown in figure 5.7. A symmetrical beam pattern with a recognisable point spread function is useful as physical effects are more easily separated from side-lobes. In addition, a closely packed array minimises near field effects; these are more pronounced on NSTX-U due to the SAMI array's closer proximity to the plasma. The compact circular array configuration was also found to perform well in terms of beam efficiency.

Changes made to the FPGA firmware [106] will make frequency switching more flexible on NSTX-U; on MAST it was only possible to set the switching period to a minimum and maximum of 1 µs and 213 µs respectively. The NSTX-U firmware upgrade will set the minimum switching period to 10 µs but remove any upper limit. In addition, the new firmware will use digital down-conversion and down-sampling

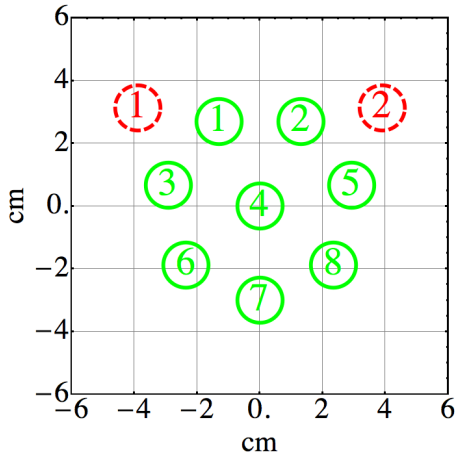

Figure 5.7: The NSTX-U sinuous SAMI array configuration. The positions of the two emitting antennas are indicated by red dashed circles and are numbered 1-2. The positions of the eight receiving antennas are indicated by green circles and are numbered 1-8. The array is shown as viewed from the plasma facing side.

to allow the FPGAs to stream active probing data in real time to disk. This removed any upper limit on active probing data acquisition time (limited to 500 ms on MAST by the FPGA memory).

Figure 5.8 gives an overview of the installation of the SAMI diagnostic on NSTX-U. The antenna array and heterodyne receiver are attached to the NSTX-U vacuum vessel itself (see also figure 5.11). The SAMI array is connected to the heterodyne receiver by 18 40 GHz 50 Ω SMK 2.92 cables; 16 for each polarisation of the 8 receiving antennas and 2 for the active probing launching antennas. Two LO signals arrive at the heterodyne receiver through two 18 GHz 50 Ω SMA cables; one to down convert the received signals and one to up convert the probing waveform. The 50Ω 18 GHz SMA cables and the 40 GHz 50Ω SMK 2.92 cables are the blue and yellow cables visible in figure 5.11 respectively.

Once each of the antenna channels are down converted and split into I and Q components they leave through 16 low frequency cables (brown cables visible in figure 5.11). The two active probing IF frequencies arrive through a further two low frequency 50 Ω SMA cables. These 18 IF cables pass through a filter patch panel before connecting to the FPGAs and digitisation unit. Here the 16 cables containing the received signal are digitised and the active probing IF frequencies are generated. The active probing data is then streamed to disk on the PC via two

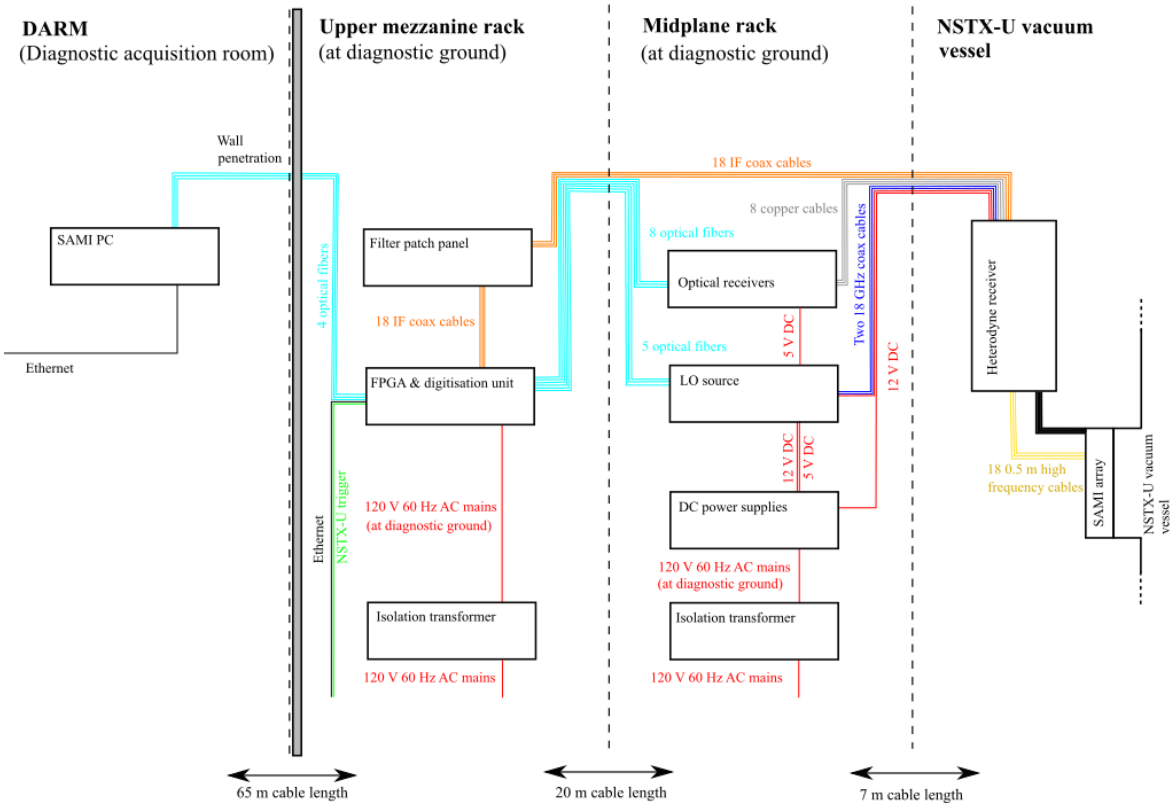

Figure 5.8: Cable diagram of SAMI's installation on NSTX-U.

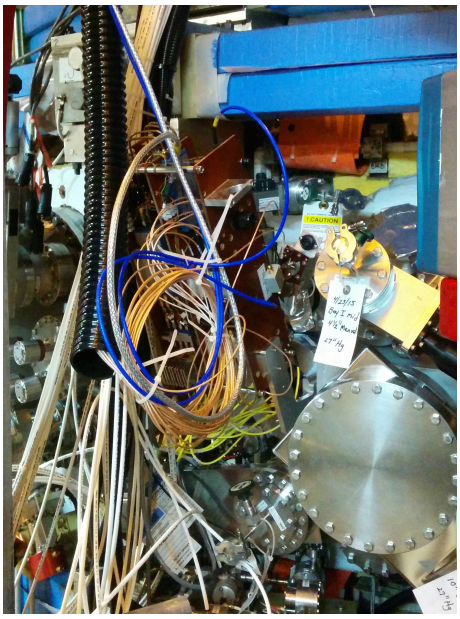

Figure 5.9: The SAMI array and heterodyne receiver mounted on the NSTX-U vacuum vessel.

optical fibres (one for each FPGA board). Two more fibre optic cables are used to pass the passive imaging data to the PC and to power cycle the FPGA board. The

data stored on the SAMI PC can then be accessed remotely via the PPPL intranet.

The whole system is FPGA controlled via a web page interface. Which frequencies to acquire, switching period, length of acquisition, polarisation switching and active probing can all be controlled via the web page on a shot by shot basis. The FPGAs then implement this user defined configuration via optical fibre to the LO source and polarisation switches. A mechanical shutter is placed immediately in front of the SAMI window to protect the window from lithium conditioning and block Electron Cyclotron Heating (ECH) used during plasma start up. The FPGAs can turn off the active probing amplifier if it is found that the shutter fails to open at the start of the shot (launching a beam into a closed shutter risks damaging the receiving RF electronics). To synchronise the system with the NSTX-U experiment a trigger is sent to the FPGAs which then initiate data acquisition. To prevent ground loops the system is ground lifted by isolation transformers.

The FPGA and digitisation unit was placed in the upper mezzanine rack in order to distance it as much as possible from the vacuum vessel: neutrons and microwave burst can cause hardware failure in electronic components located too close to the vessel. This led to the IF cables being considerably longer than on MAST leading to an additional 3 dB of attenuation. This extra attenuation and the comparative low gain of the sinuous antennas were counteracted by configuring the ADCs to add an additional 6 dB of gain at the digitisation stage.

5.2.1 NSTX-U mounting bracket design

Prior to SAMI's installation on NSTX-U a new mounting bracket design was required. This had to satisfy the spatial constraints of bay I and be done in a way (for reasons outlined in section 5.3.2) that allowed the SAMI array and heterodyne receiver to be unmounted from the NSTX-U vacuum vessel without any coaxial cables having to be disconnected. It was also desirable that the SAMI array could be removed and replaced with ease. The design was developed through an iterative procedure between myself and Bob Ellis at PPPL. The final design was that of a ring that could be bolted over the SAMI port flange (CAD drawing shown in figure 5.10). The ring would hold the SAMI array in place inside the re-entrant port as well as supporting the heterodyne receiver.

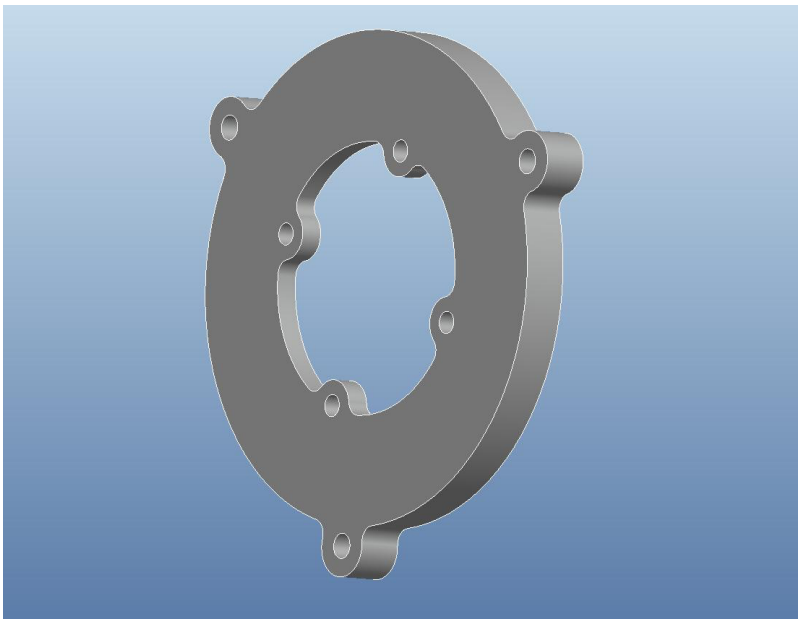

Figure 5.10: SAMI NSTX-U mounting bracket design. The inner ring of holes is to support the SAMI array while the outer holes are to secure the bracket onto the port flange.

5.3 NSTX-U calibration

Prior to data acquisition on NSTX-U the SAMI installation required calibration. Calibrating the SAMI diagnostic is an involved procedure and an exhaustive discussion is given in [31]. In the interest of expediency, here we will limit our discussion to the two most prevalent effects.

5.3.1 Rebalancing the I and Q components

The digitised I and Q channels for each SAMI antenna are non-ideally balanced. The phase shift applied by the hybrid couplers is not exact and the amplitude of each component is altered by amplifier manufacturing differences. Uncorrected, these non-ideal effects can limit the extent to which upper and lower side band separation can be achieved reducing the accuracy of the device. Thankfully, the discrepancy between each I and Q channel can be measured and corrected for using software. Let us assume that our raw uncorrected I and Q signals are given by

$$I' = A\cos(\omega t) \tag{5.1}$$

$$Q' = B\sin(\omega t + \phi) \tag{5.2}$$

where I', I, Q' and Q are the uncorrected and corrected I and Q components respectively and ϕ is the phase error introduced by the hybrid couplers. By considering equations 5.1 and 5.2 we can see that the corrected I and Q values can be obtained via the following matrix operation:

$$\begin{pmatrix} I \\ Q \end{pmatrix} = \begin{pmatrix} \frac{B}{A} & 0 \\ \frac{B}{A}\tan\phi & \sec\phi \end{pmatrix} \begin{pmatrix} I' \\ Q' \end{pmatrix}. \tag{5.3}$$

Computationally, the components correction matrix in equation 5.3 can be obtained via time averaging of the uncorrected I and Q components. For example, B/A can be obtained as follows:

$$\frac{B}{A} = \sqrt{\frac{\langle Q'Q' \rangle}{\langle I'I' \rangle}} \tag{5.4}$$

where the angled brackets denote time averaging. Similarly the other matrix components can be obtained as follows:

$$\frac{B}{A}\tan\phi = \sqrt{\frac{\langle Q'Q' \rangle}{\langle I'I' \rangle}}\tan\left[\arcsin\left(\frac{\langle I'Q' \rangle}{\sqrt{\langle I'I' \rangle\langle Q'Q' \rangle}}\right)\right] \tag{5.5}$$

$$\sec\phi = \sec\left[\arcsin\left(\frac{\langle I'Q' \rangle}{\sqrt{\langle I'I' \rangle\langle Q'Q' \rangle}}\right)\right]. \tag{5.6}$$

One should note that this process must be carried out separately for the upper and lower side-bands (when considering the lower side-band $\phi \to -\phi$).

5.3.2 Accounting for differences in signal path from antenna to digitiser

Due to discrepancies in the cables, connectors and amplifiers, the signal paths in each antenna channel are not identical. This leads to a constant phase offset in each

channel and, if not corrected, will lead to inaccurate spatial localisation of incident radiation.

In order to correct for this effect an emitting antenna is placed directly in front of the SAMI array in the far field. The ideal phase difference between all the antenna channels due to such a signal is zero. Therefore, the relative phases can be measured from the calibration source and subtracted from all further measurements, thereby correcting for the path length differences.

Due to the short wavelength radiation observed by the SAMI diagnostic (λ = 1-3 cm for 34.5-10 GHz) a phase offset in an antenna channel can be changed significantly by, for example, the tightness of a cable connector. Therefore, if any of the cables are disconnected then a new calibration is required. With this in mind, the calibration was done on-vessel so that the SAMI array could be mounted onto the NSTX-U vacuum vessel without any cables being disconnected. The NSTX-U on-vessel calibration set-up (as conducted in November 2015) is shown in figure 5.11.

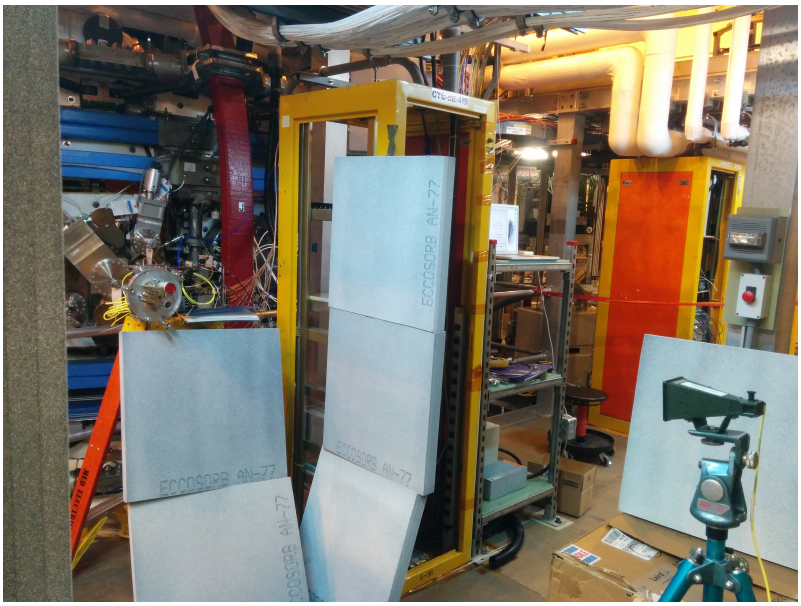

Figure 5.11: November 2015 NSTX-U on-vessel calibration set-up. The SAMI array and Flann anntenna are visible. Surrounding metal surfaces have been covered by microwave absorbing (Eccosorb) material in order to minimise spurious reflections in the calibration environment.

Chapter 6

MAST Results

Declaration

Figures 6.2, 6.5, 6.6, 6.7 and 6.9 and the accompanying discussion have been previously published in [34, 35, 100].

6.1 SAMI diagnostic spectra

SAMI data analysis differs markedly from that used on conventional DBS experiments. Limited to eight wide field of view receiving antennas only a partial suppression of signals outside a chosen probing direction is possible leading to challenging spectral interpretation. In the following sections we give an overview of the received spectral power distribution.

6.1.1 Single antenna spectra

The IF power spectrum of data acquired between 200-202 ms on a single SAMI receiving antenna during the fixed frequency 14 GHz MAST shot 27970 is shown in figure 6.1(a). A constant background punctuated with discrete peaks is visible. The background is B-X-O mode converted passive emission and is not the subject of this thesis. The power spike centred around 0 MHz is due to ADC bit noise and $1/\nu$ (pink) noise from the amplifiers and their power supplies. The peaked signals visible at 12, 24, 36, ... MHz are the 12 MHz active probing frequency and higher harmonics resulting from the FPGA square wave input. These large

un-Doppler shifted power spikes are visible due to reflections off the window and normal incidence reflections off the plasma. The background power envelope results from a convolution of amplification gain patterns applied to the received signal prior to digitisation. Tapering at the edges of the spectrum is caused by low pass filters imposing incomplete suppression.

When conducting active-probing data analysis, only a fraction of the SAMI IF spectrum is considered. The relevant region is shaded green in 6.1(a); zooming in on this area gives figure 6.1(b). In figure 6.1(b), either side of the 12 MHz active probing peak, two regions where the power is up to an order of magnitude above background are visible. This increase in received power is due to blue (blue shaded region) and red (red shaded region) Doppler shifted backscattered radiation.

At this point we will define some useful quantities. We define the "total blue shifted power" as:

$$P_{\text{blue}}(\theta,\phi) = \int_{\nu_{\text{probe}}+\nu_{\text{notch}}}^{\nu_{\text{probe}}+\nu_{\text{shift}}} |\hat{S}^{\text{B}}(\nu;\theta,\phi)|^2 \text{d}\nu \tag{6.1}$$

where $\hat{S}^{\text{B}}$ is the frequency domain synthesised beam signal (defined in Equation 2.12), $2\nu_{\text{notch}}$ is the width of the central un-shifted active probing peak, $2\nu_{\text{shift}}$ is the width of the frequency band containing Doppler shifted power and ν_{probe} is the IF frequency of the active probing beam. The relevance of the ν_{notch} and ν_{probe} parameters are illustrated in figure 6.1(b). Similarly we can define the "total red shifted power" as:

$$P_{\text{red}}(\theta,\phi) = \int_{\nu_{\text{probe}}-\nu_{\text{shift}}}^{\nu_{\text{probe}}-\nu_{\text{notch}}} |\hat{S}^{\text{B}}(\nu;\theta,\phi)|^2 \text{d}\nu \tag{6.2}$$

One can also define a "centre of gravity" of the Doppler shifted IF spectrum as:

$$\nu_{\text{cog}}(\theta,\phi) = \frac{\int_{\nu_{\text{probe}}-\nu_{\text{shift}}}^{\nu_{\text{probe}}-\nu_{\text{notch}}} \nu\hat{S}^{B}(\nu;\theta,\phi)d\nu + \int_{\nu_{\text{probe}}+\nu_{\text{notch}}}^{\nu_{\text{probe}}+\nu_{\text{shift}}} \nu\hat{S}^{B}(\nu;\theta,\phi)d\nu}{\int_{\nu_{\text{probe}}-\nu_{\text{shift}}}^{\nu_{\text{probe}}-\nu_{\text{notch}}} \hat{S}^{B}(\nu;\theta,\phi)d\nu + \int_{\nu_{\text{probe}}+\nu_{\text{notch}}}^{\nu_{\text{probe}}+\nu_{\text{shift}}} \hat{S}^{B}(\nu;\theta,\phi)d\nu} \tag{6.3}$$

6.1.2 Beam formed spectra

To form figure 6.2(a), the SAMI array was focused using beam forming onto each point in an equally spaced 21 by 21 grid spanning $\pm 40^\circ$ in the horizontal and vertical viewing directions. The blue-red Doppler shifted power imbalance ($P_{\text{blue}} - P_{\text{red}}$) was

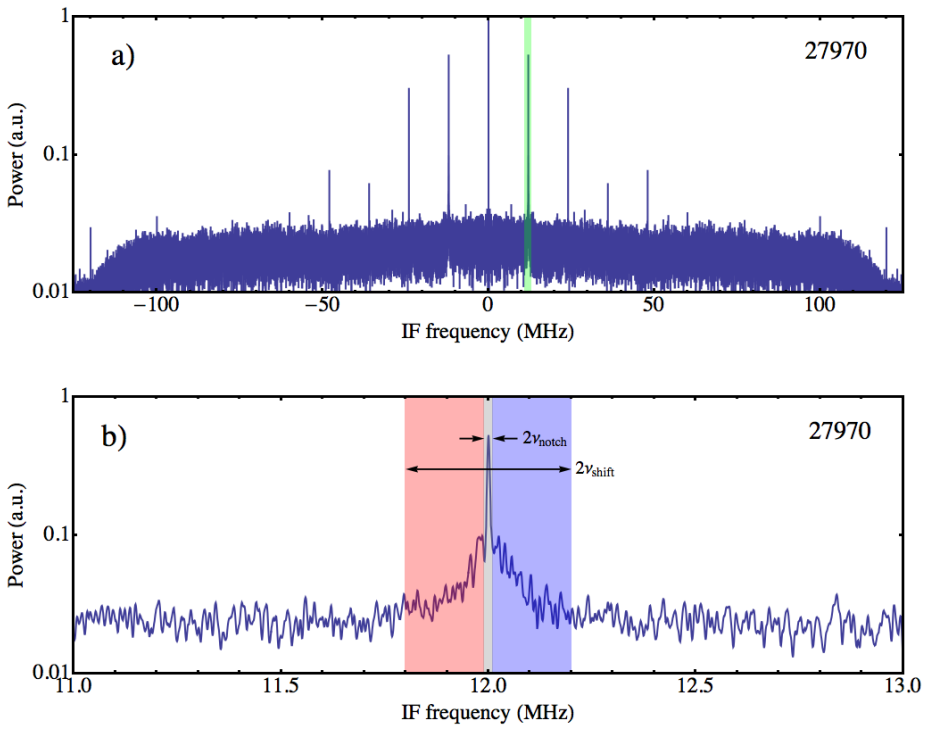

Figure 6.1: The SAMI IF spectrum for data taken between 200-202 ms during fixed frequency 14 GHz MAST shot 27970. In (a), the region of the IF spectrum used in DBS data analysis is marked by green shading. This subsection of the spectrum is then shown in (b). In (b), the red and blue Doppler shifted signal regions are marked by red and blue shading respectively. The gray shaded region marks the un-Doppler shifted region. The significance of the ν_{notch} and ν_{shift} parameters are also indicated.

then calculated at each point on the grid. Figure 6.2(a) shows a contour plot of this data where the ν_{probe}, ν_{shift} and ν_{notch} parameters were set to 12, 0.2 and 0.01 MHz respectively. The points of maximum and minimum $P_{\text{blue}} - P_{\text{red}}$ are marked by the crosses labelled 1 and 2 respectively. Figures 6.2(b) and 6.2(c) show $\hat{S}^{\text{B}}$ when focused at positions 1 and 2 respectively. There is a notable absence of Doppler peaks in these spectra as would be observed in conventional DBS experiments [38, 40–44, 46, 59, 107]. This is caused by the partial directionality of the receiving beam smearing out the spectral localisation of received power. In addition, SAMI data acquired on MAST is only digitised on a single linear polarisation. Therefore, O and X-mode polarisations cannot be separated delocalising the scattering location and increasing the range of sampled $K_{\perp}$s. Due to a continuum of different $K_{\perp}$s, a

convolution of backscattered signals and both O and X-mode polarisations present, a fully quantitative interpretation of the observed spectra is challenging. A synthetic diagnostic which models the probing beam using a full-wave treatment would aid interpretation; just such a code is currently under development at the University of York [108]. Nevertheless, the directional weighting imposed by the phased array does allow a red-blue power imbalance to be resolved allowing information to be extracted as will be discussed in the following sections.

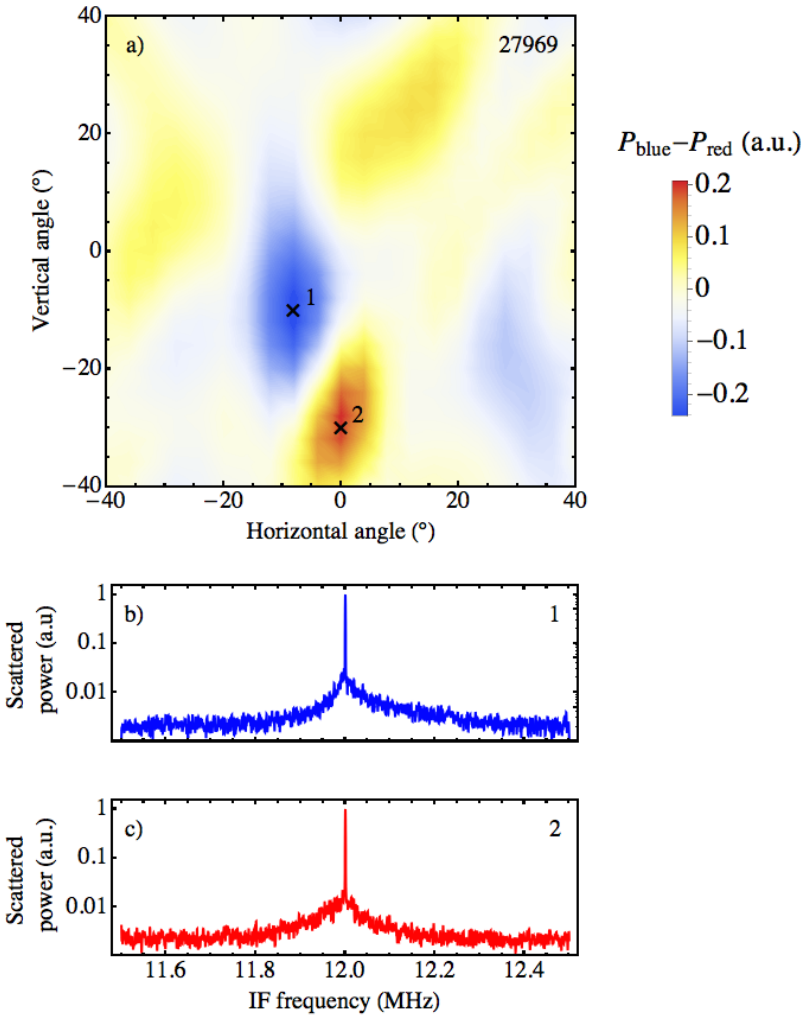

Figure 6.2: (a) Contour plot of $P_{\text{blue}} - P_{\text{red}}$ where $\nu_{\text{probe}} = 12$ MHz, $\nu_{\text{shift}} = 0.2$ MHz and $\nu_{\text{notch}} = 0.01$ MHz. Numbered points 1 and 2 mark the angular positions of maximum and minimum $P_{\text{blue}} - P_{\text{red}}$ respectively. Panels (b) and (c) show $\hat{S}^{\text{B}}$ when the receiving beam was focused at points 1 and 2 respectively. Data used to plot (a), (b) and (c) was aquired between 290 and 310 ms during MAST 16 GHz fixed frequency shot 27969.

6.2 2D "centre of mass" Doppler shift (L-mode)

Figures 6.3(a)and (b) show contour plots of total ($P_{\text{blue}} + P_{\text{red}}$) and "centre of gravity" (ν_{cog}) Doppler shifted power as a function of horizontal and vertical viewing angle respectively where ν_{shift}, ν_{probe} and ν_{notch} are 0.2, 12 and 0.01 MHz respectively. Doppler backscattering is most efficient when both $k_{\parallel}$ and $k_{\perp}$ are small: cross referencing with figure 5.4 we can see the Doppler backscattered power distribution in figure 6.3(a)reflects this. In figure 6.3 we can see that there are regions of predominantly blue and red-shifted backscattered radiation centred around {-8°,-8°} and {4°,-32°} respectively (similar to the pattern of $P_{\text{blue}} - P_{\text{red}}$ visible in figure 6.2). This is due to turbulent structures elongated along magnetic field lines moving diagonally downwards as the plasma rotates. The slant is dictated by the magnetic field pitch and the Doppler shift is related to the rate of rotation by equation 2.8. The asymmetry between the blue and red-shifted regions is due to the SAMI array being positioned above mid-plane making the blue shifted region more visible. The crosses positioned at {-8,-8} and {4,-32} in figure 6.3 mark the points of maximum and minimum ν_{cog} respectively and the points {-5,-14}, {-2,-20} and {1,-26} are evenly spaced in image coordinates between these two extrema.

Figures 6.4(a) and (b) show $\nu_{\text{cog}} - \nu_{\text{probe}}$ and $P_{\text{red}} + P_{\text{blue}}$ (background passive emission subtracted) respectively at probing orientations {-8°,-8°}, {-5°,-14°}, {-2°,-20°}, {1°,-26°} and {4°,-32°} as specified in figure 6.3(b). Figures 6.4(c), (d) and (e) show the major radius, normalised minor radius and $k_{\perp}$ at the scattering location respectively as calculated by TORBEAM. Missing values correspond to when the launched beam missed the plasma entirely. Spontaneous plasma spin up and therefore an increased observed turbulence velocity causes $|\nu_{\text{cog}} - \nu_{\text{probe}}|$ to increase over the first 100 ms in figure 6.4(a). Plasma turbulence is moving towards the SAMI receiving array at {-8°,-8°} and away at {4°,-32°}; this is reflected in the measured ν_{cog} across the five focusing points. From 100 to 380 ms ν_{cog} stays relatively constant until a mass gas injection occurs resulting in an increase in the observed backscattered power (see figure 6.4(b)) and a decrease in $|\nu_{\text{cog}} - \nu_{\text{probe}}|$. The mass injection also causes a substantial increase in the line averaged density (see figure 6.4(f)). There is a notable decline in the total backscattered power as shown in figure 6.4(b) from 100 to 200 ms potentially due to a reduction turbulence

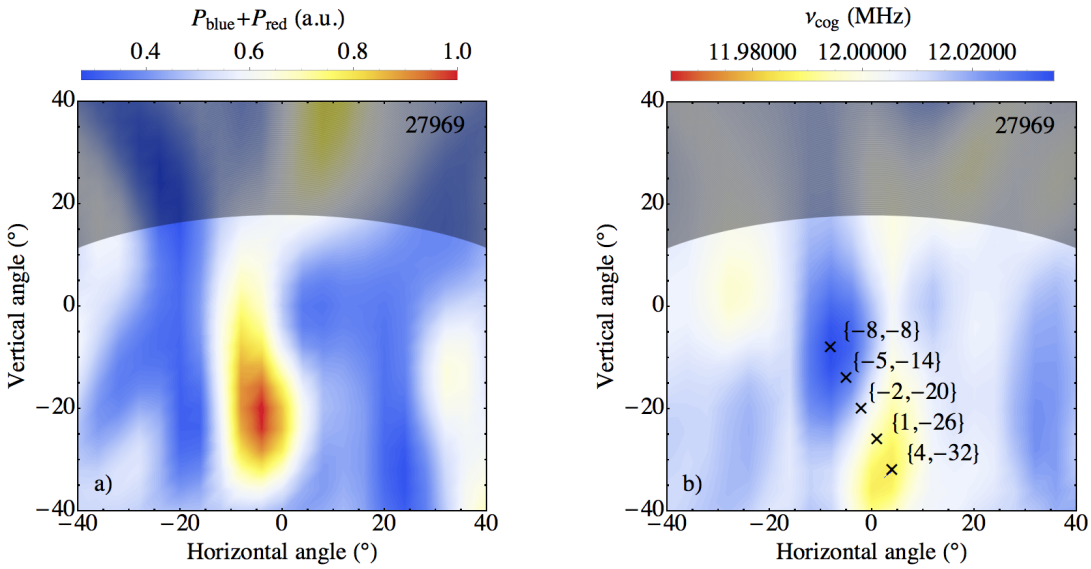

Figure 6.3: (a) and (b) show the Doppler shifted power ($P_{\text{blue}} + P_{\text{red}}$) and the centre of gravity Doppler shift ($\nu_{\text{cog}}(\theta, \phi)$) respectively integrated between 50 and 184 ms during MAST fixed frequency, 16 GHz, Ohmic, L-mode shot 27969 where ν_{probe}, ν_{shift} and ν_{notch} are 12, 0.2 and 0.01 MHz respectively. In (b) five different probing orienataions are marked by crosses at {-8°,-8°}, {-5°,-14°}, {-2°,-20°}, {1°,-26°} and {4°,-32°}. Time traces of ν_{cog} with the beam focused at these five points are shown in figure 6.4.

amplitude in the backscattering layer.

Figures 6.2(a), 6.3(a), 6.3(b), 6.4(a) and 6.4(b) show the first ever simultaneous 2D DBS analysis that has been conducted on a fusion plasma experiment. Measuring the temporal evolution of ν_{probe} at five locations simultaneously, as shown in figure 6.4(a), is a capability unique to SAMI. Spontaneous plasma spin up has been observed on previous conventional DBS experiments [39]; it is encouraging therefore that SAMI, as a proof-of-principle device, has re-observed this phenomena.

However, it is important to note that only a "centre of gravity" spectral measurement has been made whereas conventional DBS systems would consider the spectral shift of a discrete peak. SAMI routinely measures $|\nu_{\text{cog}} - \nu_{\text{probe}}|$ ~0.01 MHz whereas a Doppler peaks have been observed to be offset by ~1 MHz on conventional MAST DBS experiments operating at similar frequencies [46]. Therefore, using ν_{cog} to calculate turbulence velocity would give a gross underestimate. Although trends in ν_{cog} are observed which agree with previous results, an absolute measure of turbulent

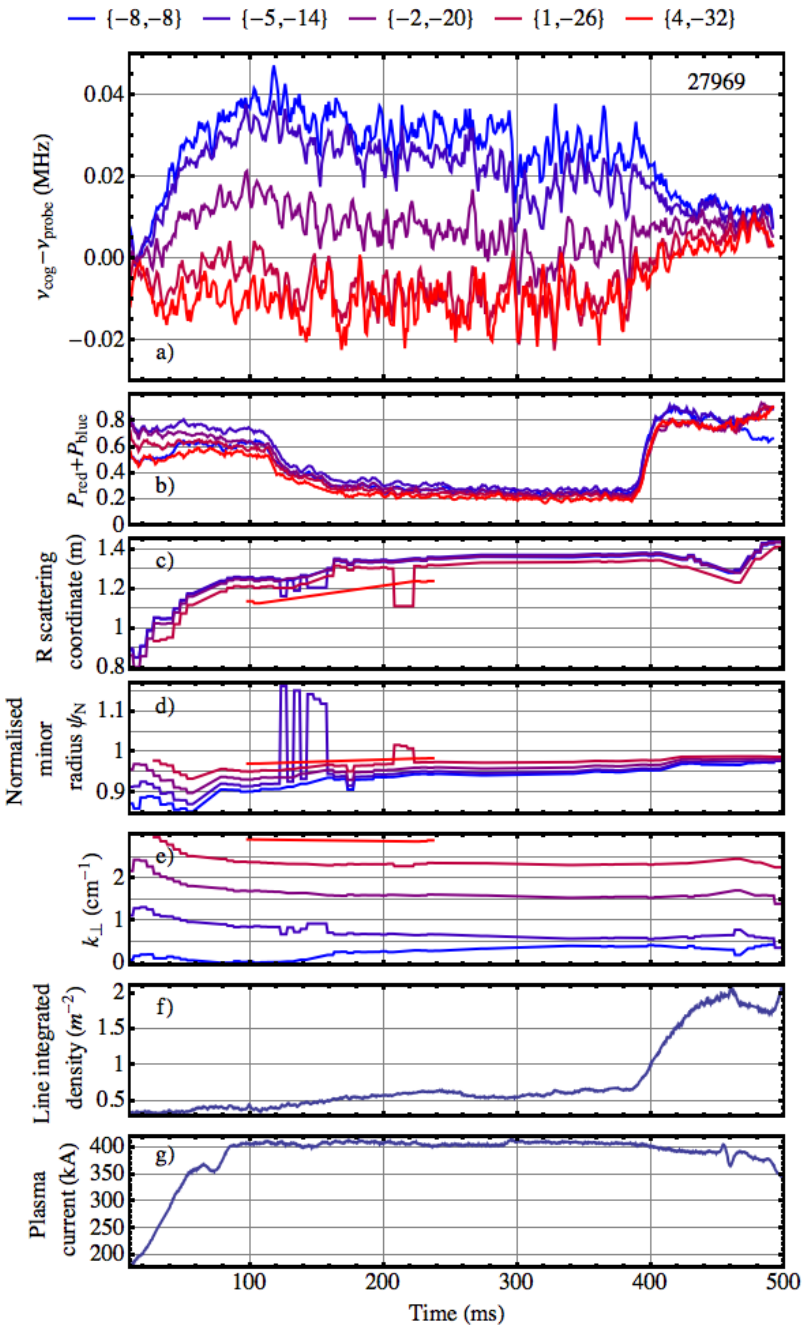

Figure 6.4: (a), (b) 4 ms moving average of ν_{cog} and $P_{\text{red}} + P_{\text{blue}}$ respectively as a function of time for five different probing orientations: {-8,-8}, {-5,-14}, {-2,-20}, {1,-26} and {4,-32} during the MAST fixed frequency, 16 GHz, Ohmic L-mode shot 27969. Parameters ν_{probe}, ν_{shift} and ν_{notch} are 12, 0.2 and 0.01 MHz respectively. (c) Major radius scattering location. (d) Normalised minor radius. (e) $k_\perp$ at the scattering location. (f) Temporal evolution of line integrated electron density. (g) Temporal evolution of plasma current.

velocity is not possible using SAMI in its current configuration. How a phased array device might be designed in order to make such measurements will be discussed in section 8.1.

6.3 2D "centre of mass" Doppler shift and DBS power (H-mode)

Figure 6.5(a) shows the 40 ms moving average of centre of gravity Doppler shift ($\nu_{\text{cog}} - \nu_{\text{probe}}$) from a receiving beam focused at {-20°,8°} in image coordinates during H-mode MAST shot 28100. This probing orientation was chosen as it had the greatest time averaged value of $\nu_{\text{cog}} - \nu_{\text{probe}}$. The parameters ν_{probe}, ν_{shift} and ν_{notch} were set to 10, 0.2 and 0.01 MHz respectively and data was digitised on four frequencies: 14, 15, 16 and 17 GHz with a switching time (times spent acquiring data on a single frequency channel before switching) of 200 µs. A gradual increase in ν_{cog} is observed from 70 ms onwards following 2.5 MW of NBI power being applied (figure 6.5(c)) by one of MAST's on axis, co-injected, positive ion neutral injectors (PINIs) [109]. The NBI system applies torque to the plasma resulting in spin up which leads to an increased observed Doppler shift through the second term in Equation 2.5. Once the plasma enters H-mode at 215 ms (indicated by a decrease in D_α in figure 6.5(d)) there is an abrupt decrease in $\nu_{\text{cog}} - \nu_{\text{probe}}$ resulting from an increase in the diamagnetic component of the turbulence velocity (first term in Equation 2.5) due to the formation of a steep edge pressure gradient.

Changes in Doppler shift coinciding with the application of NBI and at the onset of H-mode have been observed in previous conventional DBS experiments [38,46]. However, as with spontaneous spin up in section 6.2, never before have these phenomena been captured using a phased array system. As NBI was applied during this shot, charge exchange recombination spectroscopy (CXRS) data is available [68] which provides measurements of the radial and temporal evolution of the plasma toroidal rotation velocity. Unfortunately, a comparison with this data is not possible as it is not available in the outer edge region where scattering at SAMI frequencies takes place. A direct quantitative comparison in toroidal rotation velocity would not have been possible, but comparing qualitative trends in the velocity of the scattering

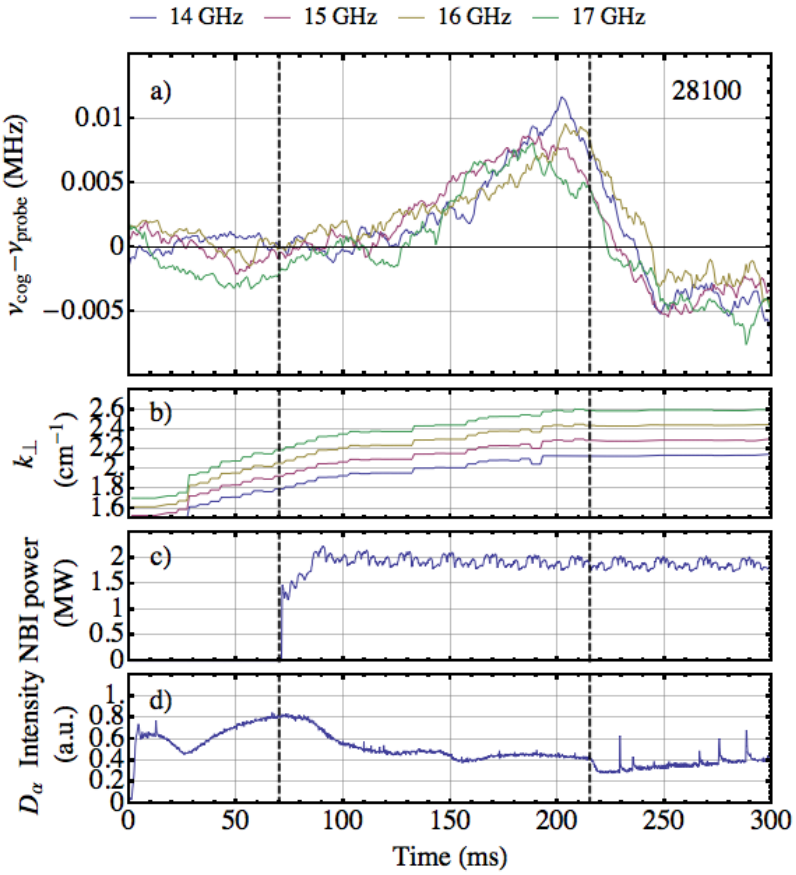

Figure 6.5: (a) 40 ms moving average of $\nu_{\text{cog}}-\nu_{\text{probe}}$ for four DBS frequency channels during MAST shot 28100. Data acquired with the receiving beam focused at {-20°, 8°} and switching in frequency every 200 µs. The black vertical dashed lines at 70 and 215 ms indicate when NBI power is applied and when the plasma enters H-mode respectively. (b) Probing beam $k_\perp$ at the scattering location. (c) Co-injected neutral beam power. (d) D_α emission.

layer could have been informative.

Figure 6.6(a) shows the 5 ms moving average of the total Doppler shifted power ($P_{red} + P_{blue}$) where the background passive emission has been subtracted. The parameters ν_{probe}, ν_{shift} and ν_{notch} were set to 10, 0.2 and 0.01 MHz respectively. The Doppler power steadily increases after the NBI is applied (70-215 ms). This is likely to be caused by an increase in the density (figure 6.6(f)) and the scattering location moving closer to the SAMI array (figure 6.6(b)) and/or an increase in the turbulence amplitude due to an increasing electron temperature gradient at the scattering location (figure 6.6(e)); the electron density gradient stays notably constant during this period (figure 6.6(d)). Temperature and electron density gradients are

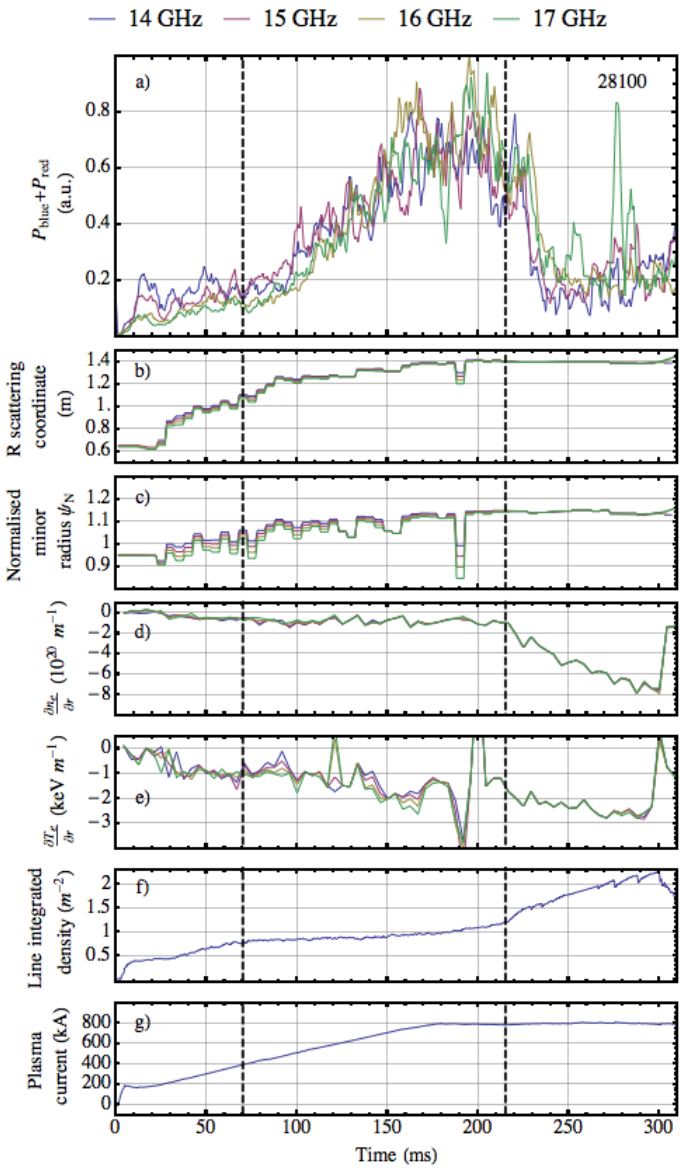

Figure 6.6: (a) 5 ms moving average Doppler shifted power ($P_{\text{blue}} + P_{\text{red}}$) when receiving beam focused at {-20°, 8°}. The two black vertical dashed lines at 70 and 215 ms indicate when NBI injection is applied and when the plasma enters H-mode respectively. A value of Doppler shifted power was calculated for each frequency step. (b) Major radius (R) scattering location. (c) Normalised minor radius of the scattering location. (d) The gradient of the electron density at the scattering location. (e) The electron temperature gradient at the scattering location. (f) The line integrated electron density using data from the MAST CO_2 interferometer system. (g) Temporal evolution of plasma current.

calculated from Thomson scattering data. There is a sharp drop in the power as the plasma enters H-mode at 215 ms despite the scattering location not changing significantly (figure 6.6(b)). This decrease is caused by the suppression of turbulence in the edge region. In figure 6.6(a) microwave bursts are observed after the plasma enters H-mode coinciding with Edge Localised Modes or ELMs (figure 6.5(d)). As shown in previous studies [103], each ELM is accompanied by a microwave burst up to four orders of magnitude above the thermal background. The H-mode spikes visible in figure 6.6(a) occur because, although the average background emission is subtracted, this will only nullify the ELM emission if the burst is evenly distributed across the IF.

The ramp up in power during NBI injection followed by a drop as the plasma enters H-mode has been observed in previous conventional DBS experiments [39].

6.4 Magnetic pitch angle measurements

6.4.1 Magnetic pitch angle: L-mode

In section 6.1.2 when discussing figure 6.2(a) it is noted that the slant in the orientation of the maximum and minimum values of $P_{\text{blue}} - P_{\text{red}}$ is dictated by the magnetic field pitch in the scattering layer. Therefore, it should be possible by observing the orientation of the blue and red-shifted radiation to make a radially localised pitch angle measurement. Figures 6.7 (a) and (b) show the distribution of P_{blue} and P_{blue} respectively during shot 27969. The maxima in P_{blue} and P_{red} are both marked with black crosses. A magnetic pitch angle measurement is made by measuring the locations of these two maxima considering their relative orientation. It is assumed that they lie perpendicular to the magnetic field lines due to backscattering's dependence on $k_{\|}$ at the reflecting layer.

This SAMI pitch angle measurement can then be compared with the pitch angle calculated by EFIT at the scattering location. The scattering location is decided upon as follows: the directions of the blue and red-shifted maxima are first measured by SAMI (blue and red dashed lines in figure 6.8), the direction immediately between these two orientations is then calculated (black dashed line in figure 6.8). Along this direction a beam is then launched using the TORBEAM code which returns

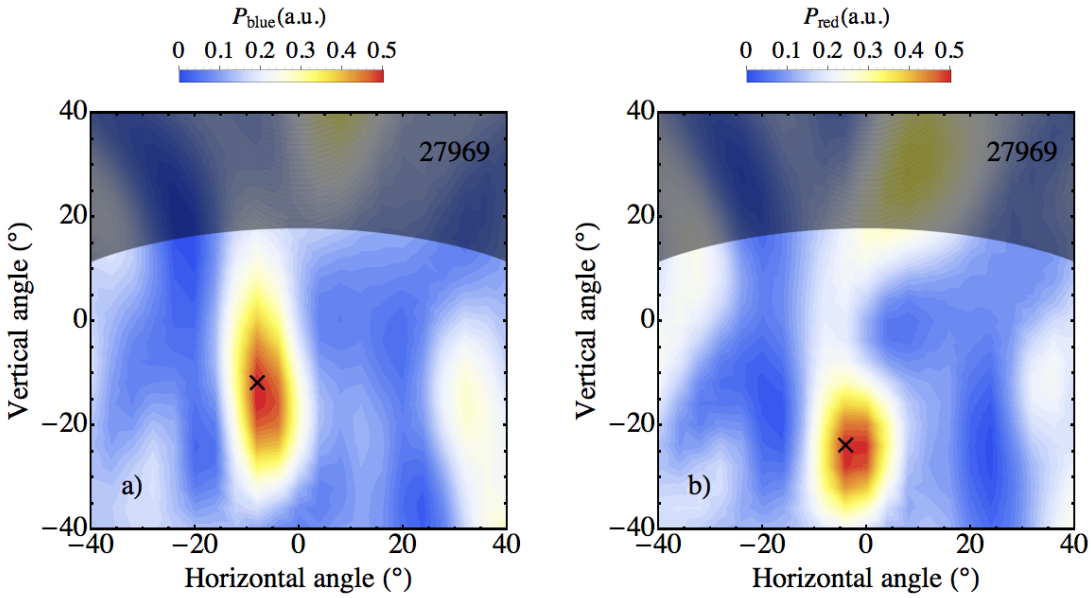

Figure 6.7: (a) and (b) show contour plots of P_{blue} and P_{red} respectively during the MAST 16 GHz fixed frequency shot 27969 where $\nu_{\text{probe}} = 12$ MHz, $\nu_{\text{shift}} = 0.2$ MHz and $\nu_{\text{notch}} = 0.01$ MHz. The maxima of P_{blue} in a) and P_{red} in (b) are marked with black crosses. Data used to plot (a) and (b) was acquired between 290 and 310 ms into the shot. The power is normalised to the peak observed value of $P_{\text{blue}} + P_{\text{red}}$

the scattering location.

Figures 6.9(a) and (b) show the temporal evolution of magnetic pitch angle as measured by SAMI (green line) and EFIT (dashed red line) for the double null discharge (DND) shots 27969 (fixed frequency 16 GHz) and 28856 (fixed frequency 10 GHz) respectively. The SAMI pitch angle time evolution was calculated using an 8 ms sliding data window. The ν_{probe}, ν_{shift} and ν_{notch} parameters were set to 10, 0.2 and 0.01 MHz respectively. A fine grid of 161 by 161 was used within the $\pm 40°$ viewing aperture for greater accuracy. The reliability of the SAMI pitch angle measurement relies on there being sufficient backscattered power. Figure 6.9(c) shows the normalised to peak value backscattered power during MAST shots 27969 and 28856 where the background passive emission has been subtracted (calculated as the sum of P_{red} and P_{blue} at each of the extrema locations). One can see that the large departure from EFIT by the SAMI pitch at 10 ms during shot 27969 coincides with a sharp drop in backscattered power. It is also apparent that departures between SAMI and EFIT during shot 28856 occur between 60-130 ms and 330-

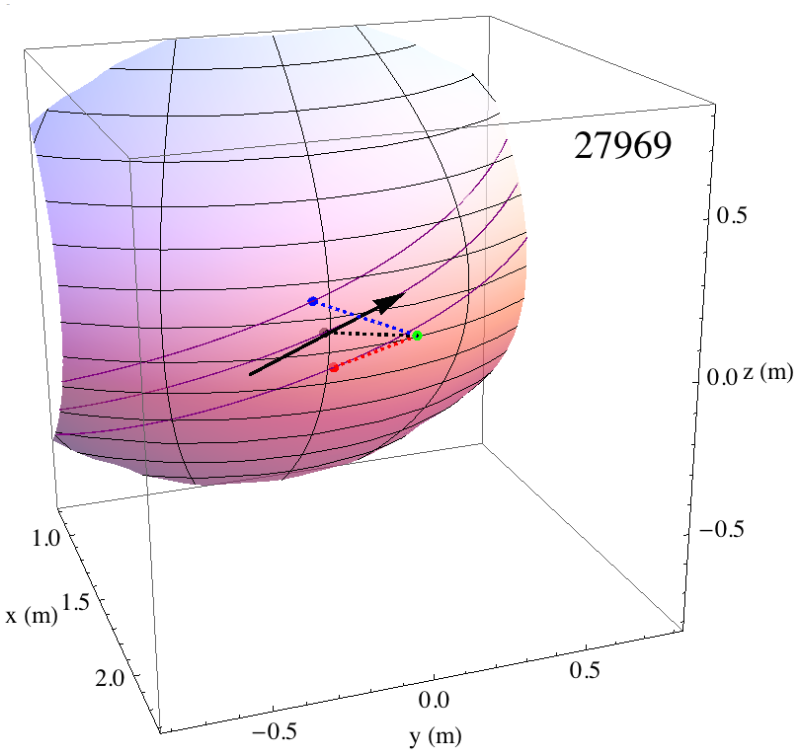

Figure 6.8: 3D illustration of the SAMI pitch angle measurement. Data shown is from 282 ms during MAST shot 27969. The centre of the SAMI array is indicated by the green dot positioned at (2.182, 0, 0.203). The 16 GHz red and blue maxima vectors, as measured by SAMI, are indicated by the red and blue dashed lines. A vector oriented directly inbetween the red and blue dashed lines is indicated by the black dashed line. The 16 GHz normal incidence O-mode cutoff surface, as calculated by Thomson scattering and EFIT is indicated by the pink-purple shaded mesh. The red, blue and black dots mark where the red, blue and black dashed lines intersect the normal incident cutoff surface respectively. The black arrow orientated perpendicular to the plane in which the red and blue vectors dashed lines lie indicates the SAMI pitch angle measurement. Magnetic field lines which lie in the cutoff surface are depicted as purple lines and show the magnetic pitch angle as calculated from EFIT.

350 ms when the DBS power is comparatively low. The fluctuation level in the SAMI pitch angle measurements during shot 28856 is noticeably higher than during 27969; the shot averaged modulus of the departure from EFIT by the SAMI pitch angle is 9.1° and 3.8° for shots 28856 and 27969 respectively. This is expected as, being a low frequency 10 GHz shot, more of the probing beam is backscattered in

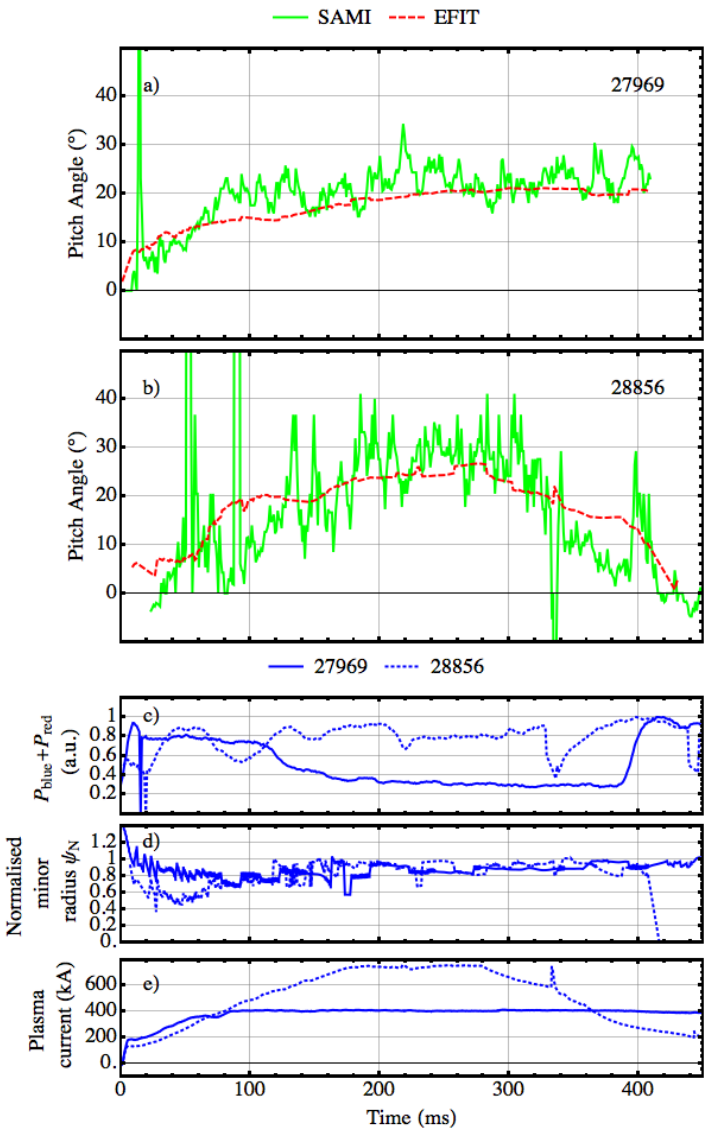

Figure 6.9: (a) and (b) show magnetic pitch angle as measured by SAMI (solid green line) and EFIT (red dashed line) at 16 GHz and 10 GHz during MAST shots 27969 and 28856 respectively. The SAMI pitch angle measurement was calculated using an 8 ms sliding data window which was moved forward 1 ms for each data point. The EFIT pitch angle was evaluated at the scattering location of a ray launched directly in-between the locations of the red and blue-shifted maxima and minima at each moment in time as calculated by TORBEAM. (c) Shows the backscattered power level at the red and blue-shifted Doppler power maxima during shot 27969 (continuous blue line) and 28856 (dashed blue line). Note that the power levels for each shot use different normalisations. (d) The normalised minor radius of the scattering location for shots 28856 and 27969.

the scrape off layer where the density fluctuation level is high. In addition, the shot averaged separation of the P_{blue} and P_{red} maxima were found to be 11.2° and 10.3° for shots 27869 and 28856 respectively. As these maxima are slightly closer together in 28856 this could also contribute to the higher fluctuation level observed. For a more exhaustive discussion of the factors affecting pitch angle accuracy see section 6.4.3. Though the radial scattering locations are similar in 27969 and 28856 (figure 6.9(d)) the pitch evolution varies due to different plasma current temporal profiles (figure 6.9(e)). Note that the pitch angle evolution is closely linked to the plasma current as larger toroidal current results in a greater poloidal field component increasing the pitch of the magnetic field (toroidal component assumed fixed).

6.4.2 Magnetic pitch angle: H-mode

Figure 6.10(a) shows the temporal evolution of magnetic pitch angle as measured by SAMI (green line), EFIT (dashed red line) and the MAST Motional Stark Effect (MSE) Diagnostic [110] (dashed purple line) during the 16 GHz fixed frequency, H-mode shot 27894. Note the extended vertical axis compared with figures 6.9(a) and (b). The ν_{probe}, ν_{shift} and ν_{notch} parameters were set to 12, 0.2 and 0.01 MHz respectively.

If one first considers the L-mode phase (0-242 ms), it is immediately apparent that fluctuation level in the SAMI pitch angle is much higher than in 27969 or 28856 (16.6° average disparity from EFIT during the L-mode phase). In figure 6.10(f) the magnetic axis is below mid-plane indicative of a lower single null discharge (SND) whose magnetic geometry results in the P_{red}, P_{blue} maxima being poorly separated: the average angular separation of the P_{red} and P_{blue} maxima was 4.1° in the L-mode phase of 27894. Any error in the position of the maxima is then amplified leading to a nosier SAMI pitch angle measurement.

During the L-mode phase where MSE data is available (MSE data is only available from 153 ms as it relies on the application of NBI) there is much better agreement between the SAMI pitch angle and the MSE data (10.5° average disparity) than the SAMI and EFIT data (16.6° average disparity). Before the onset of H-mode when MSE data is available (153-242 ms) there is a similar level of agreement between MSE and SAMI pitch angle measurements (10.5° average disparity) as there

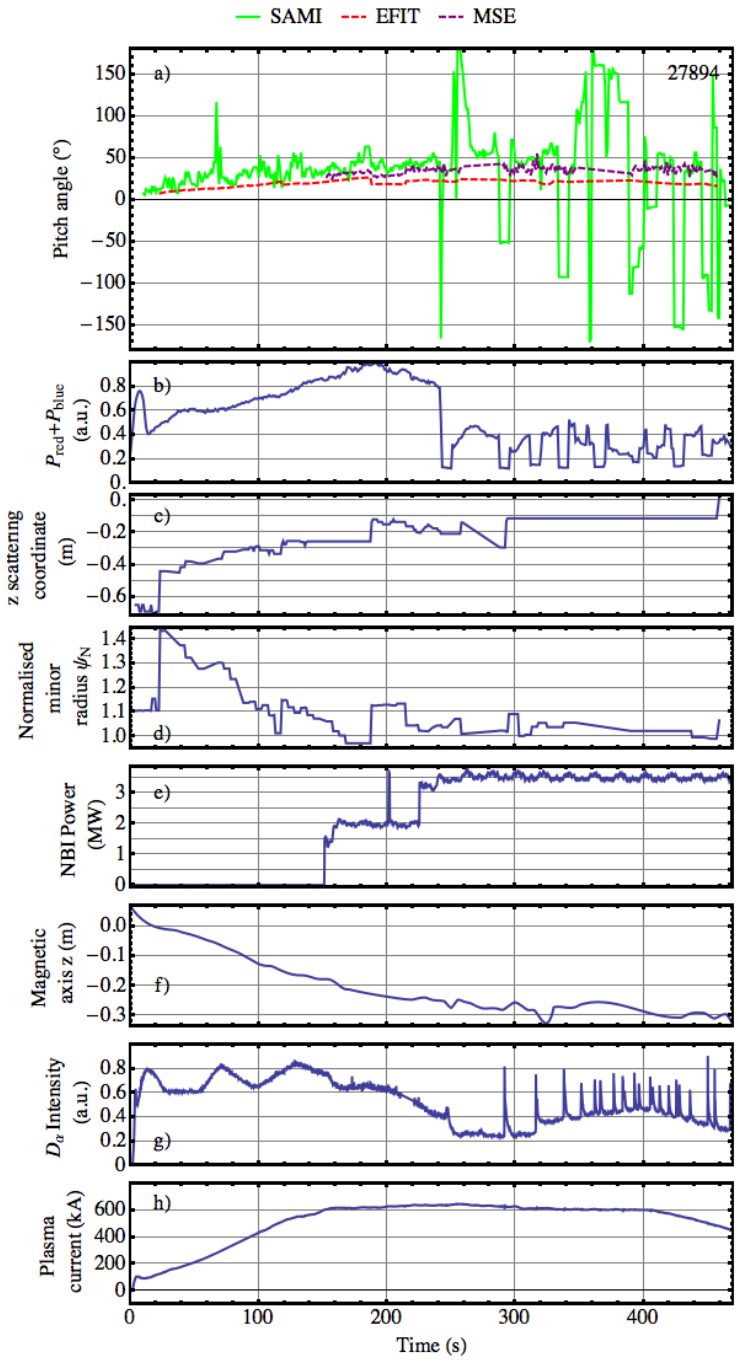

Figure 6.10: (a) Magnetic pitch angle as measured by SAMI (green line), EFIT (red dashed line) and mid-plane MSE (purple dashed line) during the 16 GHz fixed frequency MAST shot 27894. The SAMI pitch angle measurement was calculated using an 8 ms sliding data window which was moved forward 1 ms for each data point. (b) Backscattered power. (c) Vertical scattering coordinate. (d) Normalised minor radius of the scattering location. (e) NBI power. (f) The vertical coordinate of the magnetic axis. (g) D_α intensity. (h) Plasma current.

is between MSE and EFIT (10.0° average disparity). MSE and EFIT are known to be inconsistent, particularly in the edge region MAST [111]. MSE is often considered to be more reliable as it measures the magnetic pitch more directly. However, one should note that the MSE pitch information shown in figure 6.10(a) is at the radial scattering location on mid-plane as only here is data available.

Following application of the second PINI and total NBI power increasing to 3.5 MW (figure 6.10(e)) the plasma enters H-mode. As discussed before in section 6.3, this coincides with a large drop in the backscattered power (figure 6.10(b)) and bursts of passive emission (subtracted from figure 6.10(b)) coinciding with ELMs. There is a substantial increase in the fluctuation level in the SAMI data coinciding with the onset of H-mode with the average disparity to EFIT and MSE increasing to 66.9° and 60.6° respectively. These variations are not attributable to the presence of the ELMs (if the data points affected by ELMs are removed large fluctuations are still present). Most likely this increase in variability is attributable to the decrease in backscattered power during H-mode.

If one considers figure 6.11 we can see that the agreement between MSE and EFIT is good in the core while the two measurements diverge towards the edge region, particularly in H-mode. The radial resolution of the MSE diagnostic is ≃2.5 cm.

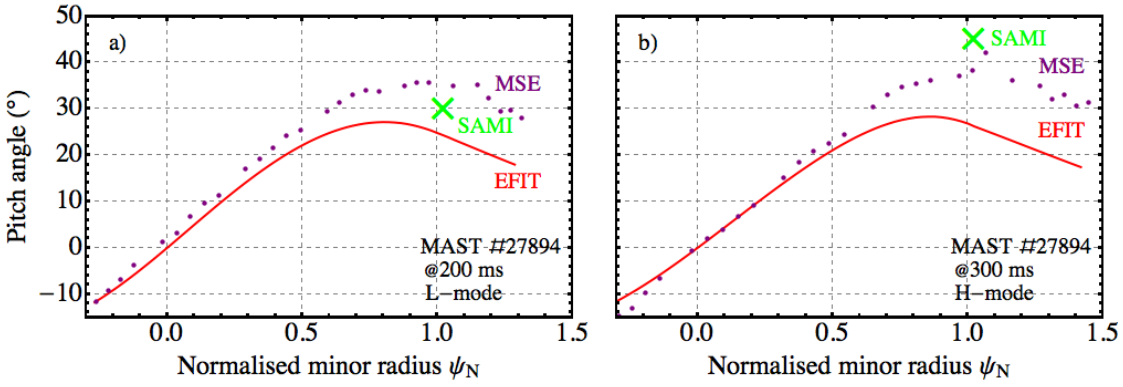

Figure 6.11: Pitch angle as a function of normalised minor radius as measured by MSE (purple dots), SAMI at 16 GHz (green cross) and EFIT (red line) for L (a) and H-mode (b) during MAST shot 27894.

6.4.3 Magnetic pitch angle accuracy

A quantitative comparison of accuracy between shots 28856 and 27969 is presented in figure 6.12(a). Data between 100-320 ms and 120-340 was considered for shots 27969 and 28856 respectively. These data windows were chosen as the pitch angle is comparatively stable during these periods. One can see that, in general, the longer the data window the better the agreement between SAMI and EFIT. This is due to randomised fluctuations with time scales of $\sim$0.5 ms causing errors in the SAMI pitch angle measurement being averaged out. These fluctuations impose a lower bound on the temporal resolution of SAMI pitch angle measurements.

If the data window is long then time resolution will be low, whereas if the data windows are short then pitch angle accuracy is affected. Figure 6.12(a) shows that given a specific time resolution (x-axis) a certain degree of agreement between SAMI and EFIT results can be expected on average during shots 27969 and 28856. The decrease in discrepancy from EFIT saturates at long integration times; by considering the c constants in each of the fits it is apparent that at large time windows the agreement will saturate with approximately one degree of disparity.

Figure 6.12(b) shows the SAMI pitch angle measurement at 80 ms during shot 27969 as the length of the data window is increased. A notable decrease in the variability of the pitch angle measurement is apparent as the data window length is increased. Before 0.7 ms the variability is extremely large with a standard deviation of $\sim$60° (figure 6.12(c). After 0.7 ms the variability rapidly decreases to a standard deviation of $\sim$10° which then slowly decreases saturating at $\sim$1° after 15 ms of time integration. Analysis such as that presented in figure 6.12 was used to decide an 8 ms time integration to be used in figures 6.9(a)and (b). In this way, a comparatively smooth measurement of pitch angle, in good agreement with EFIT, was achieved without unnecessarily compromising the temporal resolution.

6.5 Other observations

The main thrust of the analysis presented in this thesis has been to investigate the capabilities of SAMI in its active probing mode to act as a 2D Doppler backscattering diagnostic. However, many other phenomena are visible in the SAMI backscattered

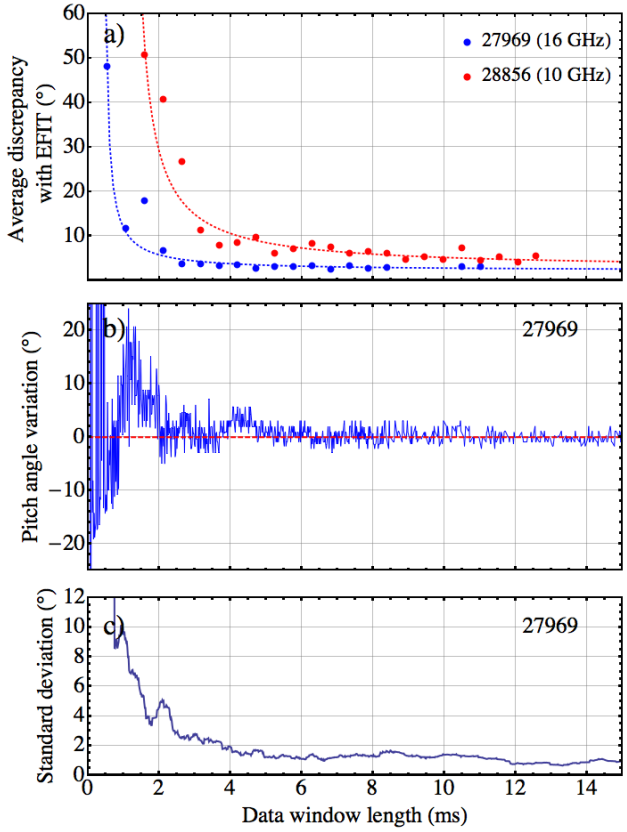

Figure 6.12: (a) Average SAMI pitch angle disparity with EFIT as a function of data window length for fixed frequency shots 10 GHz, 28856 (red dots) and 16 GHz, 27969 (blue dots). The disparity is defined as the magnitude of the difference between the SAMI pitch angle measurement and the EFIT pitch angle measurement. The average error was calculated by using data between 100 and 320 ms during shot 27969 and between 120 and 340 ms during shot 28856. Non overlapping data windows where then defined along the length of these time periods and the pitch error was averaged over the windows. The dashed blue and red lines are fits to the data of the form $\frac{a}{x+b} + c$ where x is the data window length and a, b and c are constants. The constants a, b, and c are 10.5, -0.3, 1.4 and 39.5, -0.8, 0.4 for shots 27969 and 28856 respectively. (b) The SAMI pitch angle measurement at 80 ms during shot 27969 as the length of the data window is increased (blue); the 15 ms data window value (red, dashed) has been taken away so that the departure from the 15 ms data window value is shown. From zero the length of the data window is increased by 0.02 ms increments. (c) Standard deviation of (b) using a 0.5 ms running data window.

spectrum which have physics relevance. A short overview is given here; we leave in-depth analysis of these effects to future publications.

6.5.1 Magnetohydrodynamic (MHD) phenomena

Figures 6.13(a), (b), (c), (d) and (e) show the power spectrogram of radiation incident on antenna one in the SAMI array, the power spectrogram of outboard Mirnov coil *xmc_omv/210*, total power received on antenna one, D_α emission and total neutral beam injected power respectively during the 16 GHz fixed frequency shot 27918.

Coherent structures are visible in figure 6.13(a) between 260-310 ms (arrows numbered 1 and 2) and 360-410 ms (arrow number 3). Accompanying power spectra between 260-310 ms and 360-410 ms are shown in figures 6.14(a) and (b) respectively where the same coherent structures are indicated by the numbered arrows accordingly. The coherent structures labelled 1 appear between the onset of H-mode and the first ELM which coincides with the plasma's transition back into L-mode. These structures take the form of sharp spikes in power located $\pm$21.5 kHz and $\pm$43 kHz either side of the active probing frequency. Interestingly, two long lived internal kink modes are visible in the Mirnov spectrogram at $\sim$21.5 kHz and $\sim$43 kHz during the same temporal period. However, although the kink modes are chirping in frequency, the coherent structures in the SAMI spectrogram appear constant. The 21.5 kHz and 43 kHz modes disappear from the SAMI spectrum at 310 ms when the plasma re-enters L-mode though they remain in the Mirnov signal. The modes likely become obscured by the higher level of turbulence in the edge region brought about by the L-mode transition. Comparatively broad coherent structures are also visible at $\pm$160 kHz and $\pm$200kHz at 260-310 ms (arrow #2) and 260-410 ms (arrow #3) respectively. These are likely to be associated with Doppler shifted backscattered radiation off turbulent structures.

6.5.2 Resonant Magnetic Perturbation (RMP) coils effects

Figure 6.15(a) shows the power spectrogram and temporal evolution of ν_{cog} for a SAMI receiving beam focused at {-10°,16°} during the 16 GHz fixed frequency MAST shot 27897. This orientation was selected as it had the largest value of time averaged ν_{cog} over the whole shot. Figures 6.15(b), (c), (d) and (e) show

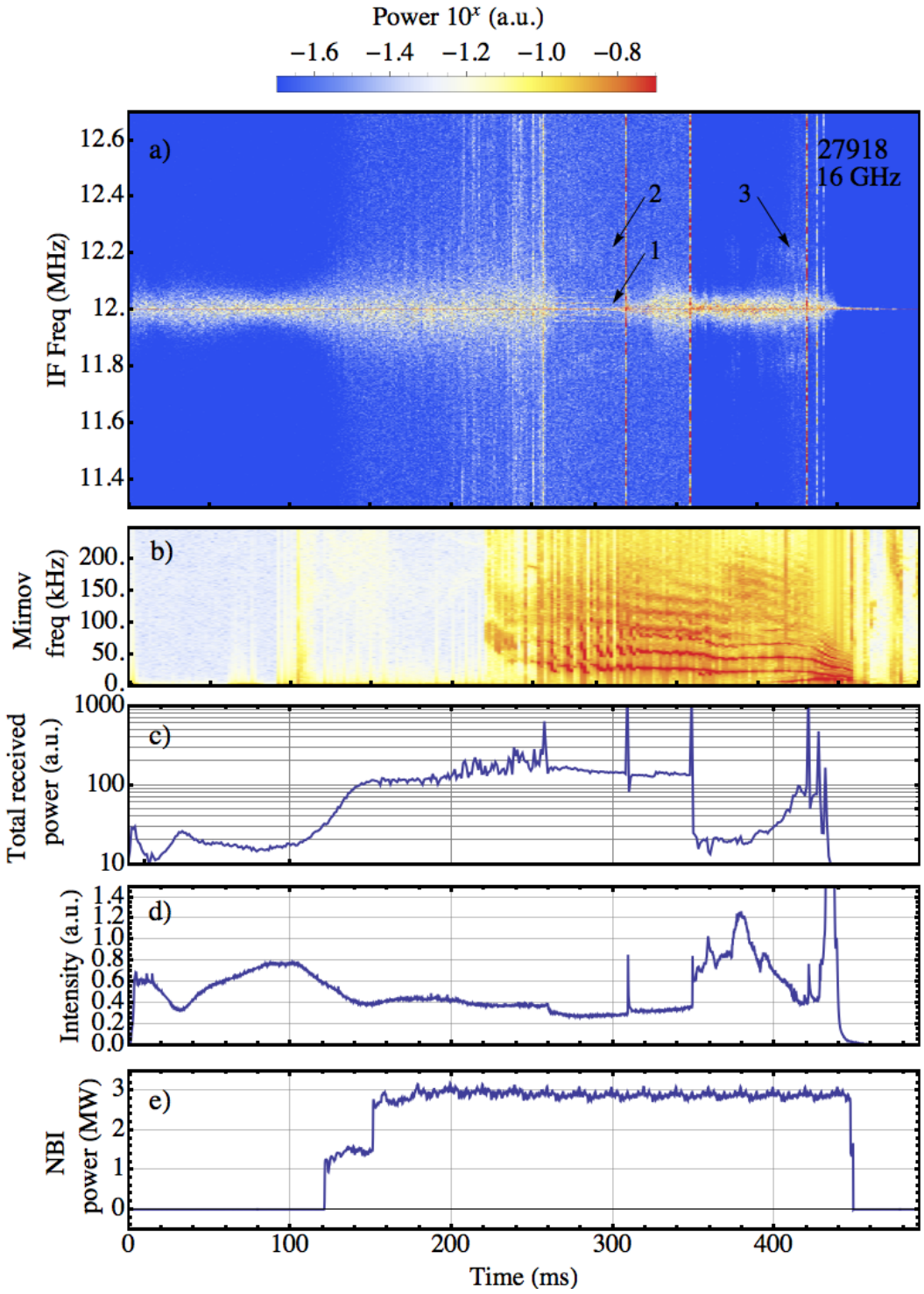

Figure 6.13: (a) Power spectogram of radiation incident on a single SAMI antenna in the region of the active probing IF frequency (12 MHz) during the 16 GHz fixed frequency MAST shot 27918. (b) Power spectrum of pickup from outboard Mirnov coil *xmc_omv/210*. (c) Total incident power received by antenna. (d) D_α emission. (e) Total NBI power.

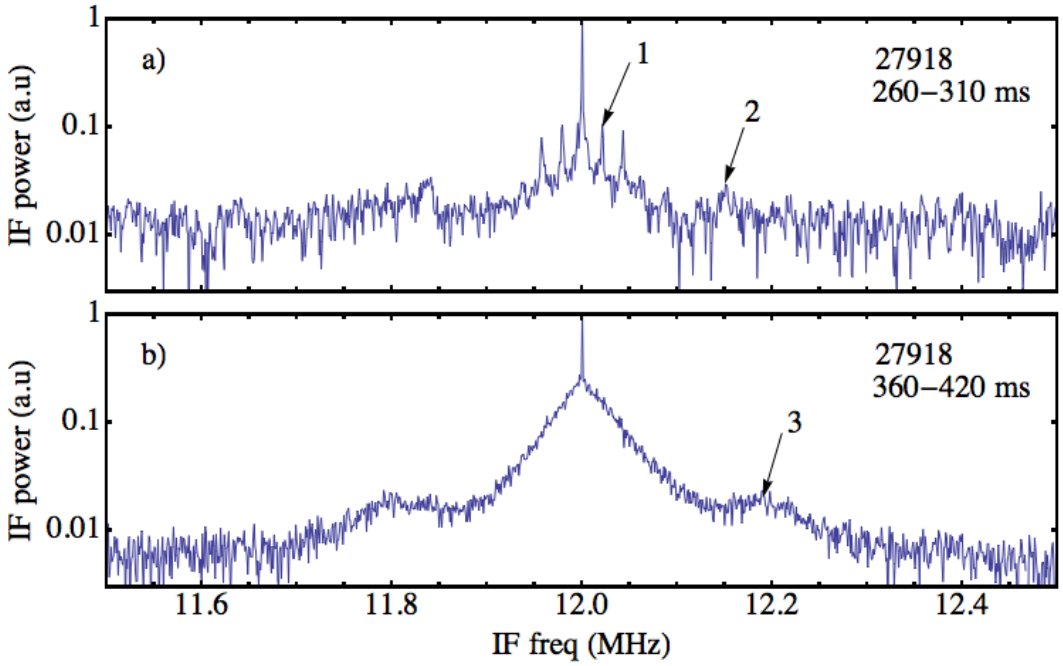

Figure 6.14: (a), (b) Power spectra of 16 GHz radiation incident on a single SAMI antenna during MAST shot 29718 for 260-310 ms and 360-420 ms respectively. Both spectra have been normalised to their peak value.

the accompanying total Doppler shifted power, D_α intensity, total NBI power, and current in the MAST RMP coils [112] respectively during 27897. Shot 27897 was an experiment to investigate the effect of RMP coils in a n=4 configuration on ELMs.

In figure 6.15 (a) one can see that the extent of the received red and blue Doppler shifted signals and ν_{cog} increase with time due to spontaneous plasma spin up up until the L-H transition. As seen before in section 6.3 the L-H transition is accompanied by a drop in the value of ν_{cog} and $P_{\text{blue}} + P_{\text{red}}$. Interestingly, as the ELM coils are applied ν_{cog} and total DBS power are observed to increase. This is likely due to the turbulence amplitude in the edge region being increased due to application of the RMPs as has been observed previously in DIII-D DBS experiments for $K_\perp$=2.5–4.5 cm^{-1} [113]. The wide distribution of the power in the spectrogram and large ν_{cog} indicates that the induced turbulence has relatively high velocity. The onset of turbulence appears gradual over a time-scale of ∼20 ms once the RMP coils are applied.

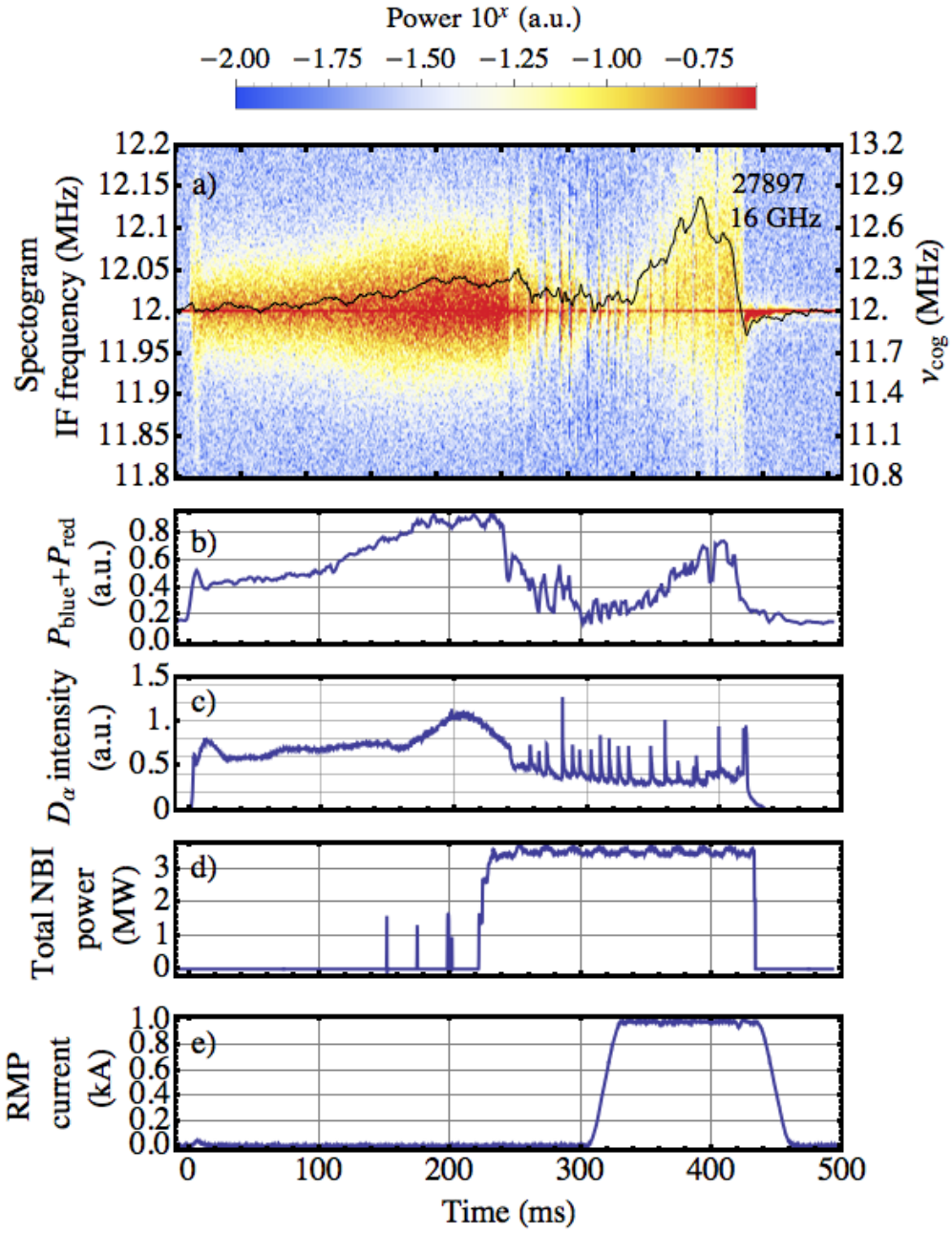

Figure 6.15: (a) IF power spectrogram of a receiving beam focused at {-10°,16°} during the 16 GHz fixed frequency shot 27897. The continuous black line shows the temporal evolution of ν_{cog} for the focused beam (the values of ν_{probe}, ν_{shift} and ν_{notch} were 12, 0.2 and 0.01 MHz respectively). (b) Total Doppler shifted power (background passive emission subtracted). (c) D_α intensity. (d) Total NBI power. (e) RMP coil current.

6.6 Reflectometry

SAMI digitises the phase and amplitude of the backscattered probing beam on an array of eight antennas. In this section we explore to what extent this information

can be used to constrain the shape and position of the reflecting layer. The SAMI diagnostic hardware is not capable of continuous fast frequency sweeping as might be conducted during a conventional profile reflectometry experiment. However, SAMI can measure the relative phase, and therefore relative path length, of backscattered signals between antennas on its receiving array. Information on the shape and position of the backscattering surface is contained within this data. This analysis may be referred to as reflectometry as we concern ourselves solely with the 0^{th} order backscattered peak in contrast to the -1^{th} peak considered in Doppler backscattering analysis. However, the method which we will outline in the next two sections differs markedly from that used in conventional reflectometry experiments [61, 114].

6.6.1 Theoretical feasibility model

Initially we consider an idealised theoretical model in order to test the feasibility of extracting shape and positional information from the phase of the backscattered un-Doppler shifted signal. We assume that, through time averaging, the reflection surface can be considered smooth. Furthermore, as many of SAMI's lower RF frequency channels are located in the outer edge of the plasma (see figures 5.3 and 5.6), we assume that refraction effects can be ignored. In addition, we assume that the shape of the reflecting layer can be described by the common parametrisation [115]:

$$\begin{aligned} x &= [R - b + (a + b\cos\theta)\cos(\theta + \delta\sin\theta)]\cos\phi \\ y &= [R - b + (a + b\cos\theta)\cos(\theta + \delta\sin\theta)]\sin\phi \\ z &= z_0 + \kappa a\sin\theta \end{aligned} \tag{6.4}$$

where R is the major radius, a is the minor radius, z_0 is the position of the plasma mid-plane, b is the indentation, κ is the ellipticity (elongation $= \kappa - 1$), δ is the triangularity, θ is the poloidal angle and ϕ is the toroidal angle. A 3D cartoon of the set-up used in the model is shown in figure 6.16.

The path difference information was utilised as follows: first, a "correct" shape of the plasma was decided upon, this initial shape was then perturbed, using only the path length differences (derived from the initial correct shape) and the perturbed

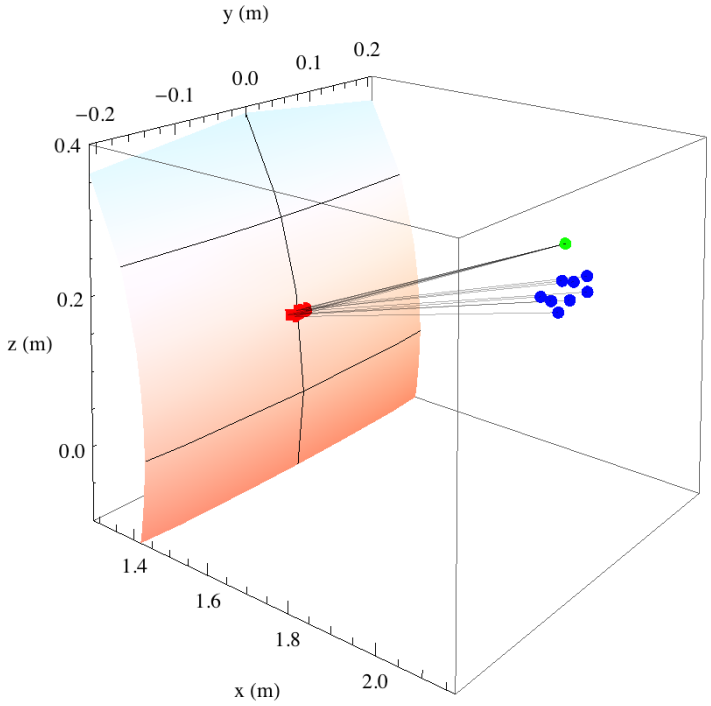

Figure 6.16: Cartoon depiction of the synthetic data set-up. The positions of the active probing antenna, reflection points and receiving antennas are shown by the green, red and blue points respectively. The probing antenna is connected to the reflection points and the reflection points to the receiving antennas by black translucent lines. The reflection surface in indicated by the pink-blue shading and is defined by the parameterisation in equation 6.4 where R, a, $z0$, b, κ and δ are 0.87, 0.59, 0.07, 0.08, 2.75 and 0.42. These values were obtained by fitting equation 6.4 to the 10 GHz normal incidence O-mode reflection surface averaged between 200 and 400 ms during MAST L-mode shot 28814.

shape it was then seen if the initial "correct" shape could be re-obtained. The "correct" shape used is defined by equation 6.4 where R, a, z_0, b, κ and δ are 0.87, 0.59, 0.07, 0.08, 2.75 and 0.42. These parameters result from equation 6.4 being fitted to the 10 GHz normal incidence O-mode reflection surface averaged between 200 and 400 ms during MAST L-mode shot 28814. This shot was used due to its extended flat top where density profiles and plasma current were held constant.

Gaussian distributed noise was added to each of the path length differences (from which phase differences are calculated) to simulate the experimental error present in a real measurement. These path length differences were then used in a minimisation procedure where the perturbed shape of the plasma was used as an initial guess

(when applied to real data this initial guess could be provided by a combination of magnetic equilibria and density profile data). The "cost" function (to be minimised with respect to R, a, z_0, b, κ and δ) was defined as follows:

$$\sum_{i=1}^{N-1} \sum_{j=i+1}^{N} [\phi_{ij} - \phi_{ij}^{\text{fit}}(R, a, z_0, b, \kappa, \delta)]^2, \tag{6.5}$$

where ϕ_{ij} is the "measured" phase difference between the i^{th} and j^{th} antenna channels and $\phi_{ij}^{\text{fit}}(R, a, z_0, b, \kappa, \delta)$ is the phase difference between the antenna channels resulting from the fit. The Mathematica function "FindMinimum" was used to find the best fit (corresponding to a local minimum of the cost function in R-a-z_0-b-κ-δ space). "FindMinimum" automatically selects either the conjugate gradient, principal axis, Levenburg Marquarddt, Newton, quasi-Newton, interior point or linear programming minimisation method depending on which one is optimal. An example of a "correct" plasma shape, an initial guess and a fitted solution is shown in figure 6.17. We can see that in the region of the reflection points the fit is much more accurate than the initial guess.

The fit was found to converge as long as the initial guess values of R, a, z_0, b, κ and δ were within 10% of the "correct" values. Using an initial guess where R, a, z_0, b, κ and δ were increased to 105% of their correct values, the accuracy of the subsequent fit was investigated for different levels of phase noise. This was done for one and two probing antennas (a second probing antenna was added to the SAMI array in August 2013). The results from this analysis are shown in figure 6.18. Phase error is defined as standard deviation of the Gaussian distributed noise added to the phase differences prior to fitting. Fit error is defined as the average distance between the "correct" position of the plasma and the plasma fit in the region of the reflection points. For each value of phase error the cost function was minimised from the 5% perturbed initial guess 10 times. The average accuracy of these 10 fits was then used as the fit error (constituting a single red or blue point in figure 6.18). A linear fit was made to both the single and two antenna points (shown by the red and blue lines in figure 6.18 respectively). From this analysis we can see that it is possible, in theory, to obtain additional information on the shape and position of the backscattering surface provided an initial guess within 10% of the correct value is available.

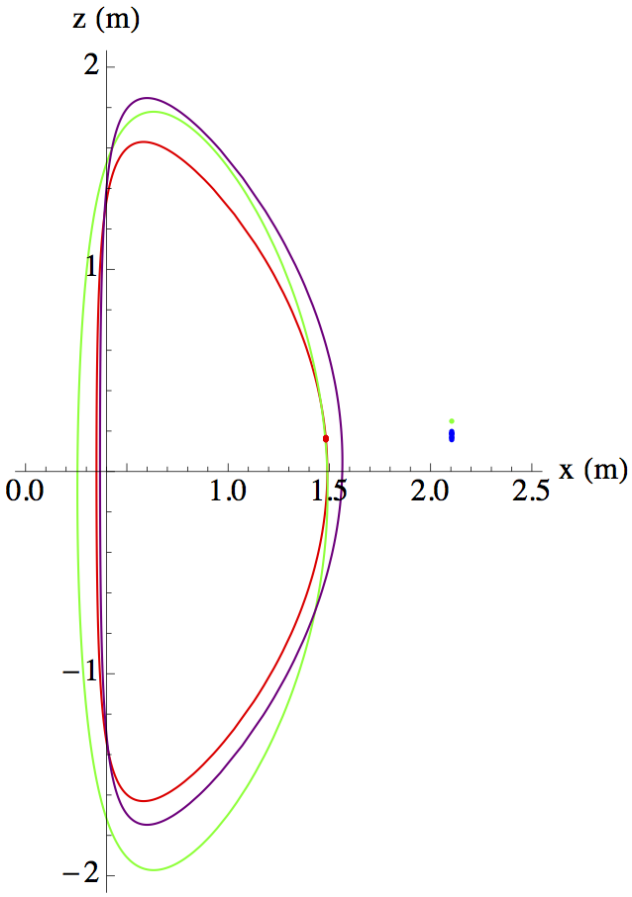

Figure 6.17: Poloidal cross-section showing the correct shape of the plasma (red), an intial guess (purple) and a curve fitted using the minimisation of equation 6.5 (green). The postions of the probing antenna, receiving antennas and reflection points are also indicated by the green, blue and red dots.

6.6.2 Application to data

Applied to real data the technique outlined in section 6.6.1 has some clear limitations. That reflected beam of each antenna channel takes a slightly different path through the plasma. Therefore each path has a slightly different length and refractive index. This will result in a phase difference in each antenna channel not attributable to the shape of the reflection layer. However, as seen in figures 5.3 and 5.6 the normal incidence cutoffs are concentrated in the outer edge region of the plasma. Therefore, the plasma path length will be short, limiting the extent of phase shift applied. Error could also arise due to SAMI's inability to separate polarisations. This would delocalises the reflection point potentially preventing the cost function outlined in section 6.6.1 from converging. However, as discussed in

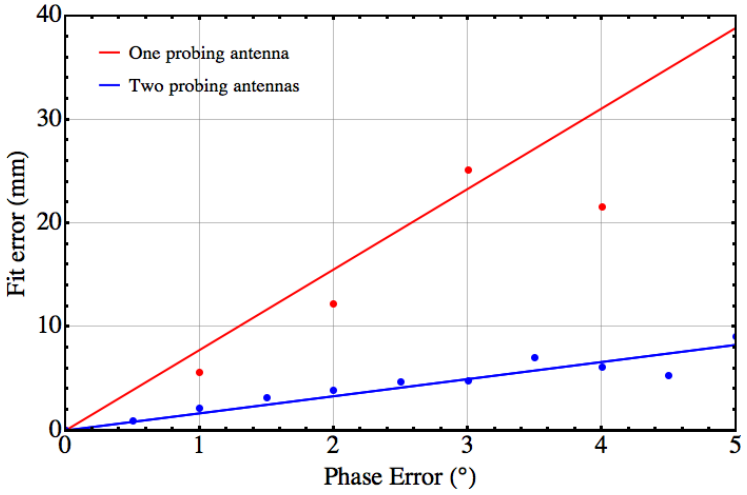

Figure 6.18: Fit error plotted against phase error for one probing antenna (red dots) and two probing antennas (blue dots). Lines fitted to the one and two probing antenna data are also shown (red and blue respectively).

sections 5.1 and 5.2 the O and X-mode cutoffs are often in close proximity limiting the phase shift between them. Despite these potential limitations, the extent to which this technique can be applied is still worthy of investigation.

When conducting Doppler backscattering experiments one is concerned with the Doppler shifted side-lobes (red and blue shaded regions in figure 6.1(b)), when conducting reflectometry experiments one is concerned with the unshifted backscattered signal (grey region in figure 6.1(b)). When analysing the un-Doppler shifted part of the SAMI spectrum one has to take into account the numerous ways that the signal can arrive at the receiving antennas other than reflecting off the surface of the plasma such as: leakage through the microwave electronics, direct cross-talk between emitting and receiving antennas and window reflections. Henceforth we will refer to this spurious signal as noise. In order to accurately measure the phase of the reflected plasma signal, the noise must first be subtracted. On MAST SAMI was configured to start acquiring 10 ms before the start of shot. This allowed the noise to be measured in the absence of plasma (allowing it to be subtracted off the plasma data later in the shot). However, this method only works if the phase of the noise remains stable throughout the shot. Unfortunately, it was found that the phase of the noise signal drifts as a function of time. It was found subsequently that for all SAMI MAST data the digitisation clock was generated separately from the

active probing signal clock. As a result of using two clocks, the timing of the digitisation drifts with respect to that of the active probing signal. This manifests itself in the data as a phase drift. The phase of 10 MHz (the active probing frequency) IF signal measured during MAST L-mode shot 28816 is shown in figure 6.19(a). The noise could still be subtracted if the rate of drift was constant as it could then be extrapolated. However, as is evident from figure 6.19(b), the rate of this drift is not constant but varies unpredictably throughout the shot. This means that it is very difficult to reliably subtract off noise at the active probing frequency. The method outlined above in section 6.6.1 cannot be implemented without reliable subtraction of this noise signal. Prior to SAMI's installation on NSTX-U the way the FPGA clocks were distributed was changed so that the active probing frequency and digitisation frequency were both set by the same clock eliminating the drift. This will be discussed further in section 8.1.

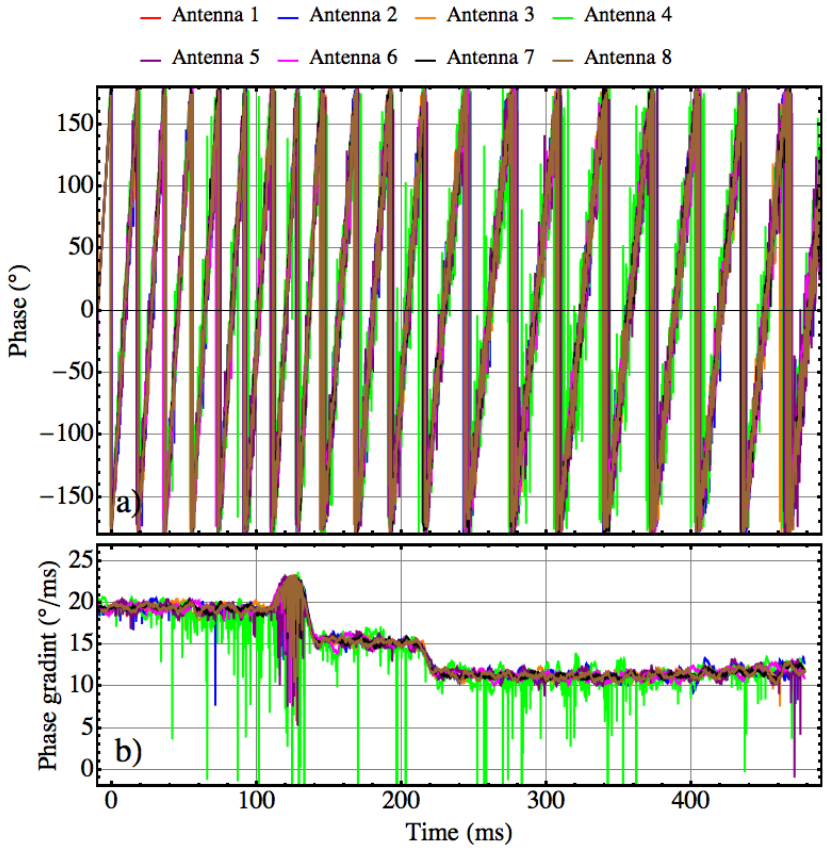

Figure 6.19: (a) The phase of the active probing frequency as measured on each of the eight receiving antennas during MAST shot 28816. (b) Rate of phase drift.

Chapter 7

NSTX-U results

Declaration

Figures 7.1, 7.2, 7.3, 7.3 and 7.4 and the accompanying discussion have been previously published in [106, 116].

7.1 DBS power comparison with MAST data

Initially, so that direct comparisons with MAST data could be made, the sinuous antennas and polarisation switches were not installed on NSTX-U. Vivaldi antennas were installed in the same configuration as that used on MAST (see figure 3.7). The first SAMI NSTX-U data was acquired on the 3rd May 2016.

Figures 7.1(a) and (b) show the power spectrum of 10 GHz radiation incident on a single SAMI antenna during the L-mode phase of NSTX-U shot 204620 and MAST shot 28856 respectively. Immediately apparent is a significant increase in DBS power above the noise floor on NSTX-U compared to MAST. This increase is expected due to the closer proximity of the SAMI array to the plasma on NSTX-U ($\sim$45 cm) compared to MAST ($\sim$77 cm). Other factors that could potentially affect the level of backscattered power are probing geometry (mid-plane port NSTX-U, above mid-plane port MAST) and the prevalence of turbulence in the scattering later. In addition to increased power, it is clear from figure 7.1(a) that much higher Doppler shifts (>1.5 MHz) are visible in the NSTX-U power spectra compared to MAST. It is reasonable to assume that such Doppler shifts are present in the MAST

spectra but not visible above the noise floor due to insufficient power (>1.5 MHz Doppler shifts have been observed during conventional MAST DBS experiments at similar frequencies [46]). The increased DBS power level and Doppler shifts (shown for 10 GHz in figure 7.1) are visible on all operating frequency channels in SAMI NSTX-U data.

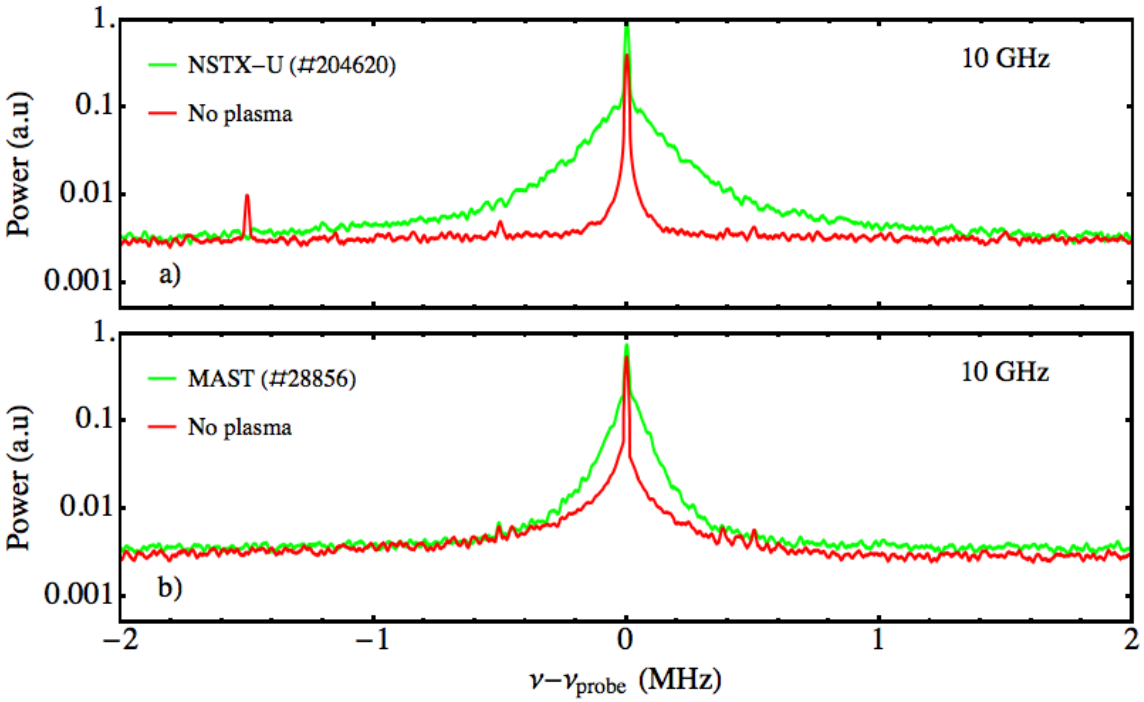

Figure 7.1: (a) NSTX-U power spectra of 10 GHz radiation incident on a single SAMI antenna during the L-mode phase of shot 204620 (green) and when no plasma is present (red). (b) MAST power spectra of 10 GHz radiation on a single SAMI antenna recieved during the L-mode phase of shot 28856 (green) and when no plasma is present (red). Each plot shows the Fourier power spectrum of data recived during a 4.19 ms time interval.

7.2 2D "centre of mass" Doppler shift and DBS power

On NSTX-U as on MAST, the "centre of mass" Doppler shift was investigated as a function of time at a fixed viewing orientation (see figure 7.2(a)). In figure 7.2 the receiving beam is focused in the {-16°,8°} direction (orientation of maximum

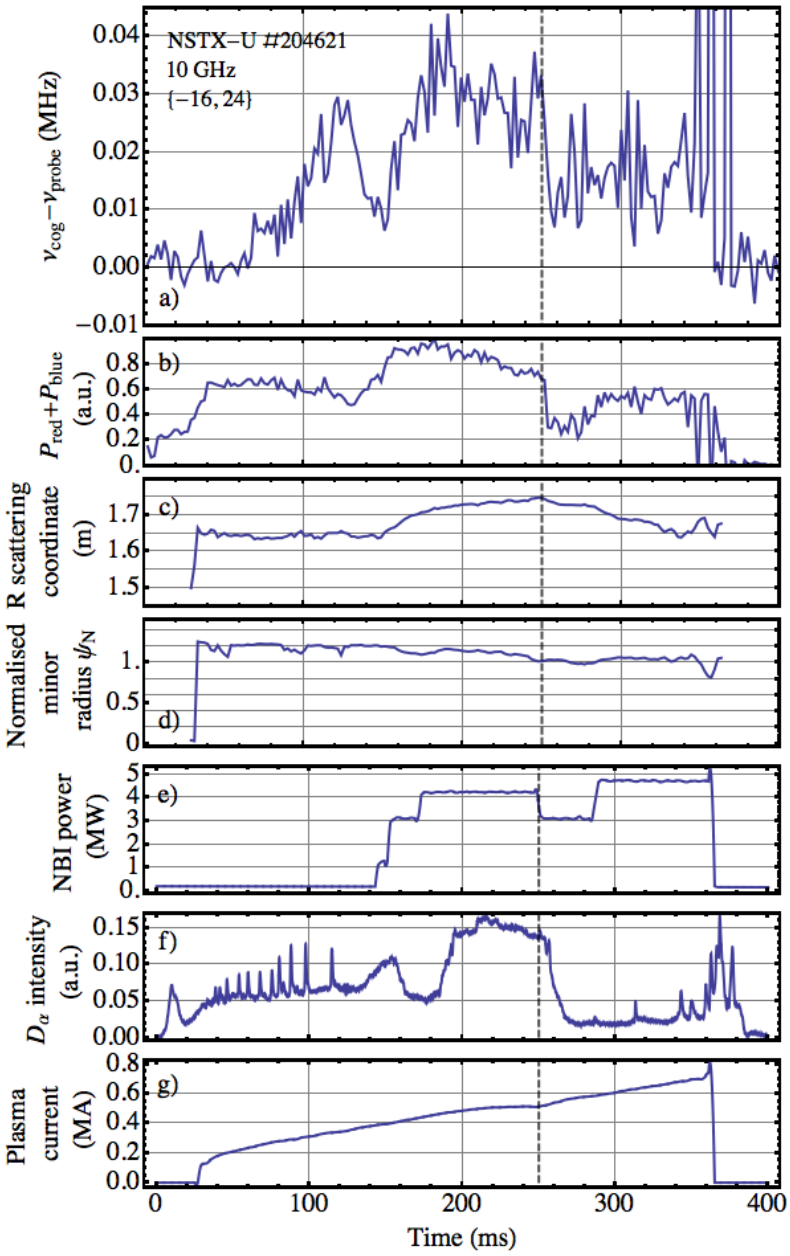

Figure 7.2: (a) Centre of mass Doppler shift ($\nu_{\text{cog}} - \nu_{\text{probe}}$) during the fixed frequency 10 GHz NSTX-U shot 204621 plotted with 2 ms time resolution. The data was acquired with the receiving beam focused at {-16°,8°}. The black dashed vertical line at 250 ms marks the L-H transition. The ν_{probe}, ν_{shift} and ν_{notch} parameters are 12.5, 0.6 and 0.01 MHz respectively. (b) Total Doppler shifted power ($P_{\text{red}} + P_{\text{blue}}$) plotted every 2 ms. (c) Major radius (R) scattering coordinate. (d) Normalised minor radius at the scattering location. (e) Total NBI power. (f) D_α intensity. (g) Plasma current.

$\nu_{\text{cog}} - \nu_{\text{probe}}$ averaged over the shot). In figure 7.2 we can see that many of the phenomena observed on MAST are also seen on NSTX-U: a gradual rise in $\nu_{\text{cog}} - \nu_{\text{probe}}$ at the start of the shot corresponding to intrinsic spin up is observed (seen on MAST in figure 6.4) followed by additional spin up at 150 ms coinciding with application of NBI (observed on MAST in figure 6.5). An increase in DBS power is also seen coinciding with NBI (observed on MAST in figure 6.6). A sudden decrease in observed power and $\nu_{\text{cog}} - \nu_{\text{probe}}$ is observed following the onset of H-mode at 250 ms (observed on MAST in figures 6.6 and 6.5). In figures 7.2(c)-(d) we can see, as on MAST, that H-mode causes little difference in the scattering radius which is located in the far edge region throughout. During this analysis Thomson data is often not available at the 10 GHz cutoff. The scattering locations given in figures 7.2(c) and (d) were calculated through interpolation reducing their reliability. Electron temperature and density gradients calculated at the scattering location are not given in figure 7.2 as, if provided, they would be calculated from a function extrapolated beyond the region where data is available and would therefore have little meaning. By comparing figures 7.2(a) and 6.5(a) it is apparent that the magnitude of the observed Doppler shift ($|\nu_{\text{cog}} - \nu_{\text{probe}}|$) is much greater on NSTX-U than on MAST. This is due to the higher observed DBS power on NSTX-U allowing the higher Doppler shifts (not observed on MAST) to be distinguishable above the noise floor; this pulls the centre of gravity of the observed Doppler shift out to larger values. The agreement that we have seen between the MAST and NSTX-U data by comparing figures 6.6, 6.5 and 7.2 gives us confidence that SAMI has been installed on NSTX-U correctly and that the SAMI NSTX-U data are reliable.

7.3 Magnetic pitch angle

The distribution of the DBS radiation observed on NSTX-U (see figure 7.3) closely resembles that seen on MAST (see figure 6.7). Assuming that the red and blue shifted extrema are aligned perpendicular to the magnetic field allows a magnetic pitch angle to be measured via the procedure outlined in section 6.4.1.

Figure 7.4(a) shows the magnetic pitch angle as measured by SAMI (green line) and EFIT (red dashed line) at 10 GHz during NSTX-U shot 204620. A fixed fre-

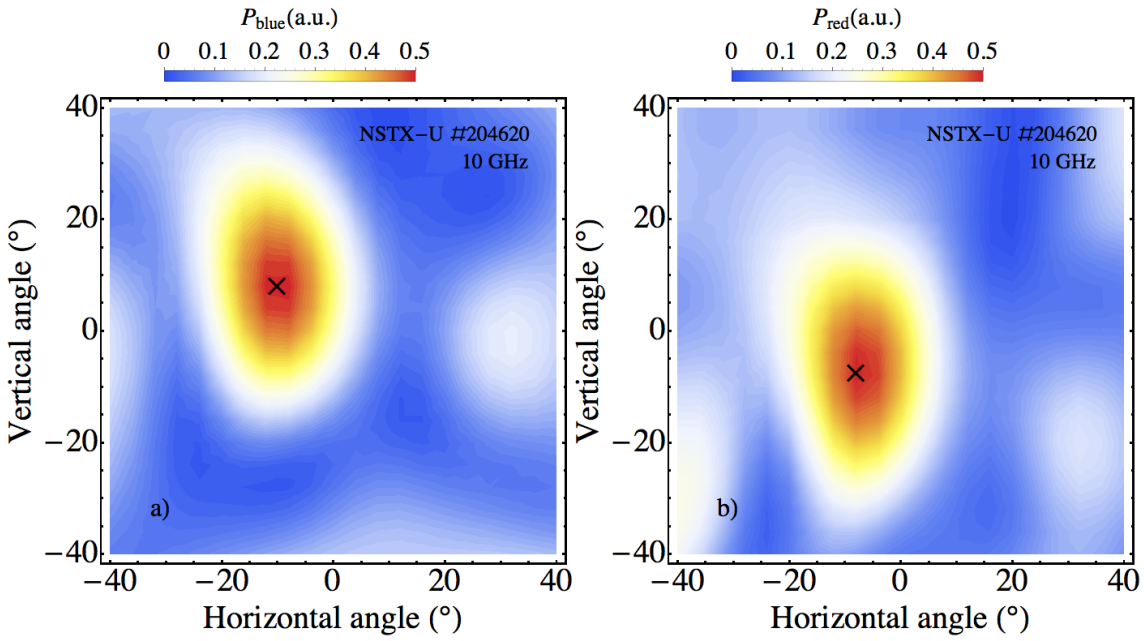

Figure 7.3: (a) and (b) show a contour plots of P_{blue} and P_{red} respectively at 10 GHz 240 ms into NSTX-U shot 204620. The ν_{probe}, ν_{shift} and ν_{notch} parameters are 12.5, 0.6 and 0.01 MHz respectively. The maxima in P_{blue} and P_{red} are indicated by black crosses.

quency SAMI data acquisition and a 8 ms sliding data window were used, as done on MAST (see figures 6.9 and 6.10). The reflection points were calculated as follows: firstly, two lines were considered emanating from the position of the SAMI array directed towards the red and blue maxima (see red and blue dashed lines in figure 6.8). A line positioned directly between these two lines was then calculated (see black dashed line in figure 6.8). The intersection point of this line and the O-mode normal incidence cutoff was then taken as the reflection point. The O-mode normal incidence cutoff surface was calculated using a combination of EFIT and Thomson data. However, one should note that, as with the 10 GHz data presented in figure 7.2, Thomson data was often not available in the region of the 10 GHz normal incidence cutoff. Therefore, extrapolation was implemented reducing the reliability of this measurement.

Figure 7.4(a) shows relatively good agreement between the SAMI measured magnetic pitch angle and EFIT at early times (<100 ms). However, this agreement breaks down at later times (>100 ms) when the SAMI measurement grossly overvalues the magnetic pitch. The EFIT magnetic pitch angle should not necessarily

be taken as "correct": see disagreement between EFIT and MSE pitch angle measurements in figure 6.10 for example. Nevertheless, this level of disparity with EFIT ($\sim$30°) and SAMI's high pitch angles (>60°) is unlikely to be physical. High overvalued pitch angles were observed on all analysed NSTX-U 10 GHz shots; 204331, 204620 and 204621. Over estimation of pitch angles ($\sim$17°) was observed on MAST (see figure 6.10) although not to the same extent as observed here ($\sim$30°). Unfortunately, at the time of writing (July 2016) we cannot make comparisons between SAMI and MSE pitch because the NSTX-U MSE system [117] is non-operational (it is expected to come online later this year).

If one considers the 10 GHz normal incidence cutoffs on NSTX-U (figure 5.6) and the measured scattering location during shot 204620 (figure 7.4(d)) one can see that scattering occurs in the outer scrape off layer. This could potentially decrease the reliability of the SAMI pitch angle measurement and account for the large disparity with EFIT. Near field effects are another potential source of error; these result from the SAMI array's close proximity to the NSTX-U plasma. In addition, Thomson scattering data was often not available in the reflection region meaning that interpolation had to be used resulting in uncertainty in the scattering location.

Despite the disparity between the SAMI and EFIT pitch, the SAMI data does show a trend of increasing pitch angle with time as the plasma current is gradually increased (figure 7.4(g)). On MAST the onset of H-mode resulted in a sharp drop in the received DBS power as well as a large increase in the uncertainty of the SAMI pitch angle measurement (see figure 6.10). On NSTX-U the onset of H-mode ($\sim$250 ms) results in no visible drop in power (see figure 7.4(b)) and the fluctuation level in the SAMI pitch angle measurement does not noticeably increase. As well as being inconsistent with MAST this result is also inconsistent with the 10 GHz data presented in figure 7.2 where H-mode is accompanied by a sharp drop in DBS power. The NSTX-U experiment log records the onset of H-mode at 250 ms during 204620 and 204621. Shot 204620 is also very similar to 204621 in a number of other regards such as plasma current, D_α intensity and NBI power. However, the response in the SAMI data differs markedly between these two shots. The data is not directly comparable as longer time integration is used in figure 7.4 than in figure 7.2 and the receiving beam direction is not fixed in figure 7.4. However, a drop in power

would still be expected as seen on MAST in figure 6.10. Further investigation into this disagreement is required.

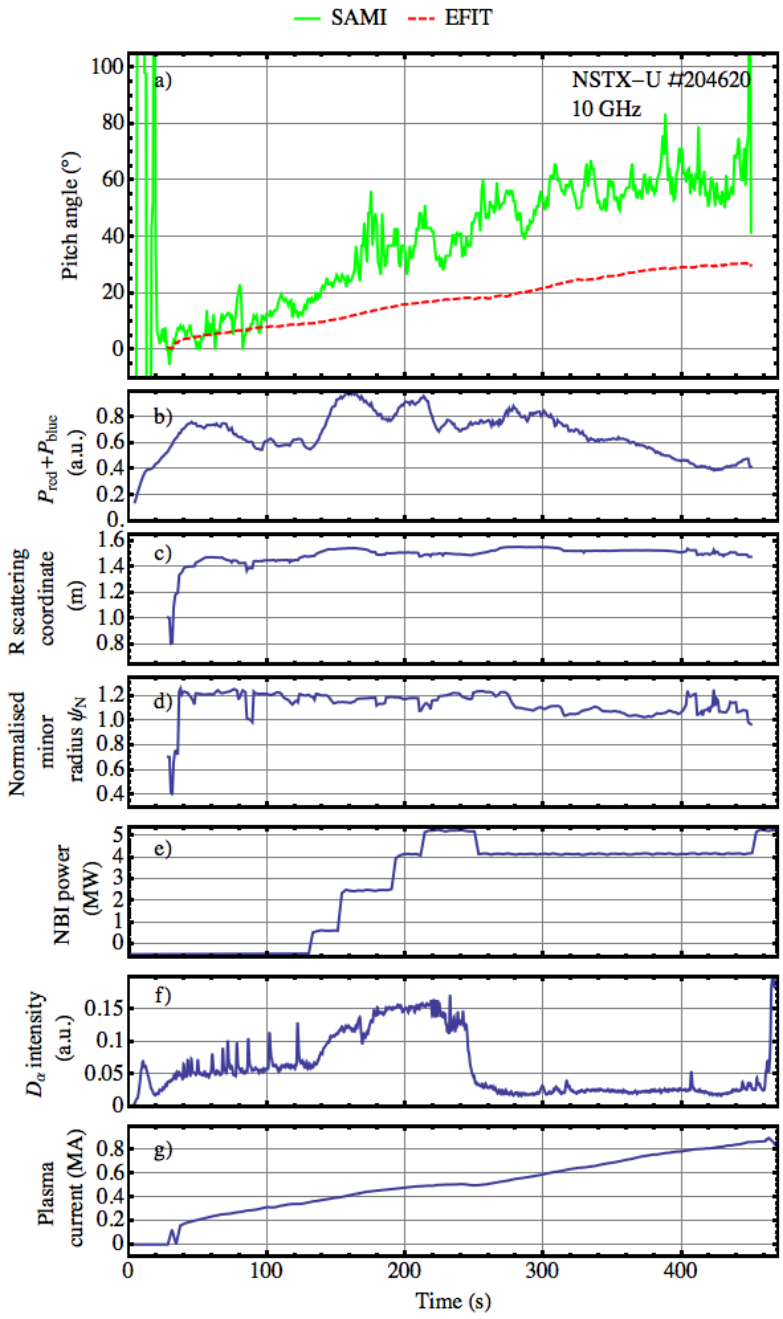

Figure 7.4: (a) Magnetic pitch angle as measured by SAMI (green line) and EFIT (red dashed line) during the 10 GHz fixed frequency NSTX-U shot 204620. The SAMI pitch angle measurement was calculated using an 8 ms sliding data window which was moved forward 1 ms for each data point. (b) Total backscattered power. (c) Major radius scattering coordinate. (d) Normalised minor radius of scattering location. (e) NBI power. (f) D_α intensity. (g) Plasma current.

Figure 7.5(a) shows the magnetic pitch angle as measured by SAMI (green line) and EFIT (red dashed line) during the 16 GHz NSTX-U shot 204944. There is a notable improvement in agreement between the SAMI and EFIT pitch angle measurements compared to that seen at 10 GHz (see figure 7.4). The greatest disparity between SAMI and EFIT is observed between 300 and 400 ms where the DBS power is low. The improvement in SAMI pitch angle between 10 and 16 GHz indicates that the 10 GHz backscattering layer is too far out in the scrape off layer on NSTX-U to provide an accurate pitch measurement.

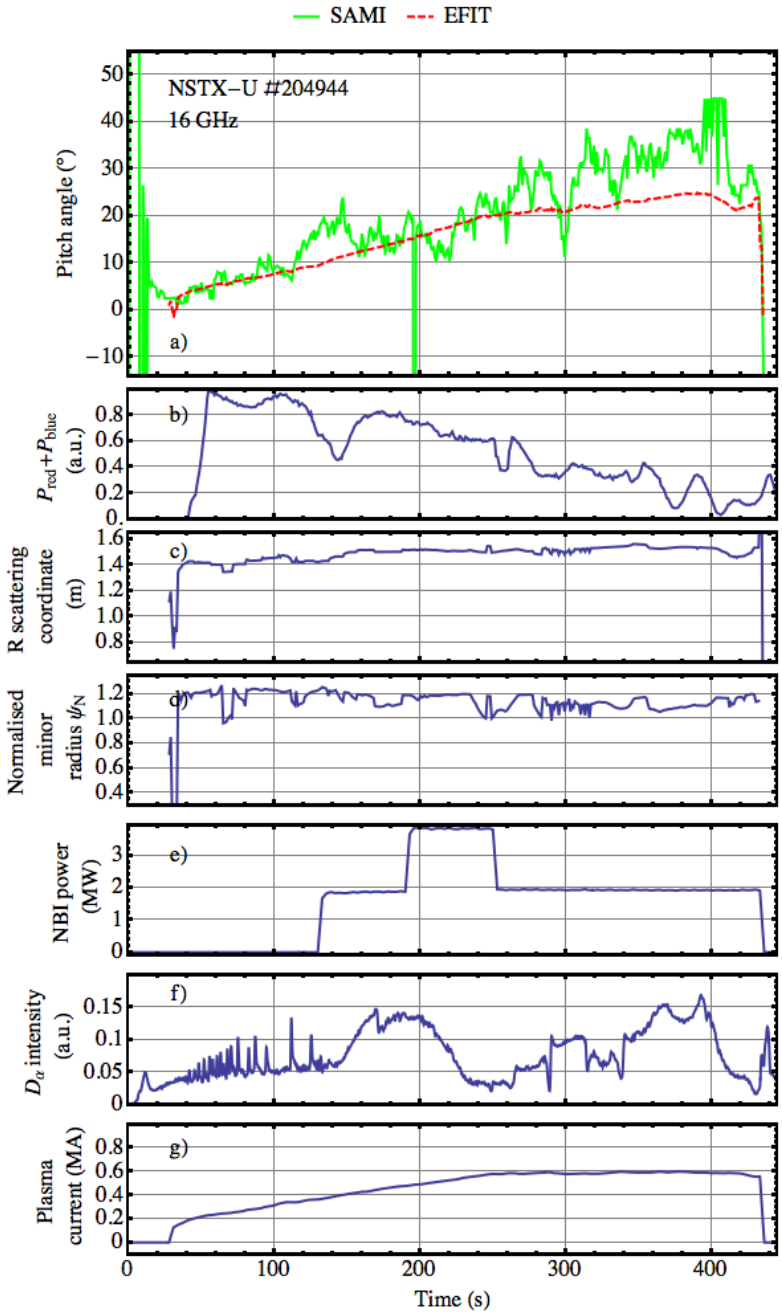

Figure 7.5: (a) Magnetic pitch angle as measured by SAMI (green line) and EFIT (red dashed line) during the 16 GHz fixed frequency NSTX-U shot 204944. The SAMI pitch angle measurement was calculated using an 8 ms sliding data window which was moved forward 1 ms for each data point. (b) Total backscattered power. (c) Major radius scattering coordinate. (d) Normalised minor radius of scattering location. (e) NBI power. (f) D_α intensity. (g) Plasma current.

Chapter 8

Conclusions and further work

The aim of this thesis was to explore the feasibility of using a phased array microwave imaging device to conduct 2D Doppler backscattering experiments. It has been found that, as well as rediscovering trends in backscattered power and Doppler shift that have been observed on previous conventional DBS experiments, SAMI's 2D capability has allowed magnetic pitch angle to be measured; the first time this has been achieved using a microwave device.

Although the use of a phased array has enabled exciting new capabilities, it is also subject to limitations. Conventional DBS diagnostics, through implementation of steerable antennas and sweeping in probing frequency, have provided $K_\perp$-spectra measurements and turbulent velocity radial profiles. The use of a narrow O or X-mode probing beam leads to a well defined scattering location and wave-number. In contrast SAMI illuminates the plasma using a very broad beam ($\pm 40^\circ$ in the horizontal and vertical directions) which is then backscattered at many locations towards the linearly polarised receiving array. Though the receiving array applies a directional weighting, the central maximum is broad (FWHM is 24-6° for frequencies 10-34.5 GHz) with a side-lobe level as high as 50% of the central maximum. This greatly delocalises the spatial scattering location and prevents the measurement of $K_\perp$-spectra. In addition, SAMI's limited directionality smears out Doppler shifted signals to the extent that no discrete peaks are visible in backscattered spectra. Therefore, no specific turbulent velocity can be linked to a particular spectrum and the trends shown in figures 6.5 and 7.2 have to be given in terms of a centre of mass Doppler shift (ν_{cog}).

However, one has to take these results in context. SAMI was never designed to conduct 2D DBS and is therefore far from optimised for this purpose. SAMI's receiving array is limited to eight antennas in a suboptimal layout (see discussion in section 8.1.2) and lacks polarisation separation. In this light, it is highly encouraging that SAMI resolved the trends in DBS power and centre of mass Doppler shift presented in figures 6.4, 6.5, 6.6 and 7.2. It shows the field of 2D DBS using purpose-built phased array devices holds great promise. There is no foreseeable reason why a future 2D DBS system would not be capable of combining the numerous advantages of conventional DBS with the alignment flexibility of a 2D phased array device through a combination of hardware upgrades and appropriate modelling.

The work outlined in this thesis has also shown that, through conducting 2D DBS, it is possible to measure magnetic pitch angle, a feat never before achieved using a microwave diagnostic. The SAMI pitch angle measurements shown in figures 6.9, 6.10, 7.4 and 7.5 are limited to a single frequency and 8 ms time integration. However, in most cases, the SAMI-EFIT and SAMI-MSE agreement is excellent (comparable to agreement typically observed between unconstrained EFIT and MSE, see discussion in section 6.4.2). This procedure constitutes a new independent channel for diagnosing pitch angle which is more direct than EFIT and, unlike MSE, does not rely on NBI.

In light of the results presented in this thesis, phased array systems such as SAMI provide an exciting and promising range of new capabilities for DBS diagnostics.

8.1 Further work

8.1.1 Investigations with existing SAMI hardware

As mentioned previously in section 6.1.2, full wave DBS modelling is currently being developed at the University of York [108, 118]. This work has the potential to aid in understanding and interpretation of SAMI spectra as well as enabling turbulent velocity radial profiles, radial electric field and $K_\perp$ spectra measurements. Further analysis of existing SAMI data in the light of this modelling offers a potentially fruitful avenue of research.

MHD and RMP effects are present in SAMI spectra and were briefly discussed

in section 6.5. This offers the possibility of using the SAMI data to assist in the identification of MHD instabilities as well as investigating the effects of RMPs on edge turbulence.

Edge turbulence velocity shear could be investigated using fast frequency switching (∼1 ms) through all available SAMI channels. Even a study of centre of mass Doppler shift as a function of frequency could potentially yield some interesting results.

A theoretical procedure for constraining the plasma's surface using SAMI data was outlined in section 6.6. Applying this method to SAMI data was found to be infeasible due to drift between the digitisation and active probing clocks. A FPGA firmware upgrade applied prior to SAMI's installation on NSTX-U (see section 5.2) eliminated this clock drift by using a single clock for digitisation and active probing. Post firmware upgrade this method can be revisited and, the extent to which the reflection surface can be constrained, explored. Furthermore, one way would be to consider using a different parameterisation of the plasma reflection layer other than that defined by equation 6.4. A simpler parameterisation, such as a quadratic, may aid cost function convergence as it would then occupy a lower dimensional space while still accurately modelling the shape of the cutoff layer.

The accuracy of MAST SAMI pitch angle measurements at 10 and 16 GHz are shown in figure 6.12. This analysis is limited to the few appropriate (in terms of frequency switching period) MAST shots available. A more comprehensive study should be possible using the SAMI NSTX-U data as larger library of appropriate data becomes available. Such a study is of particular interest as it is likely that temporal integration of 8 ms is excessive when considering NSTX-U data due to the higher level of DBS power received (see section 7.1). The dependence of SAMI pitch angle accuracy on temporal integration, DBS power, and probing frequency we leave to future study.

Using the existing hardware and firmware low temporal resolution (128 ms) magnetic pitch radial profiles are obtainable. Slow frequency switching (∼8 ms), 5 s data acquisition and a plasma scenario with an extended (>128 ms) steady state period would be required. Unfortunately, at the time of writing (July 2016), such a data set has not been acquired. However, if such a data set were analysed this

could potentially provide the first edge current density measurement acquired using a microwave diagnostic.

Once MSE data becomes available on NSTX-U, a comparison with the SAMI pitch angle measurement can be made. Ideally, this comparison should be made using an MSE constrained EFIT equilibrium as this will not only provide more accurate pitch values, it will also increase the accuracy of inferred scattering locations.

In 6.10 and figure 7.4 we assumed that the SAMI pitch measurement is incorrect. However, another approach would be to use the SAMI pitch angle to constrain the EFIT equilibrium solver and see if a better or worse fit results (quantified by the χ^2 parameter). Indeed, this analysis could be done for all the SAMI pitch angle measurements given in this thesis and compared to unconstrained and MSE contained EFIT results. The value of the χ^2 parameter could then give a relative measure of how "correct" the SAMI, MSE and unconstrained EFIT values are.

Only a limited analysis of the NSTX-U data has been presented in chapter 7. Many more avenues of research remain unexplored, such as the temporal evolution of centre of mass Doppler shift's (ν_{cog}) dependence on probing frequency at fixed orientation. In addition, current apparent inconsistencies in the data, such as no drop in power in the 10 GHz NSTX-U pitch measurement at the onset of H-mode during shot 204620 (see figure 7.4), remain to be explained.

As outlined in section 5.2, polarisation switches, sinuous antennas and a new array configuration are intended to be installed on NSTX-U. The necessary components have already been purchased and are on site at PPPL. However, at the time of writing (July 2016) these components are yet to be installed. Installation will take place once a sufficiently comprehensive NSTX-U Vivaldi single polarisation data set has been acquired. Moving to this new set-up presents risks, such as lower gain (discussed in section 4.3). However, making these changes increases the capability of the SAMI diagnostic and potentially improves the quality of the data acquired. It is likely that the reliability of the SAMI pitch angle measurement is affected by the lack of polarisation separation and it is known that scattering within the Vivaldi array has an adverse effect on the acquired data (see section 4.2).

As discussed in section 7.3, it is possible that near field effects are having an adverse effect on the SAMI NSTX-U data. These effects can be accounted for in

the analysis code. For example, the SAMI beam forming code currently focuses onto a sphere with a radius approximately equal to that of the distance from the SAMI array to the plasma. This could be altered so that the beam is focused onto a toroidal density surface provided by Thomson data and EFIT eliminating any potential near field errors.

The work in the thesis has been done as part of a collaboration with Durham University's Centre for Advance Instrumentation. Joanne Chorley has been working with the SAMI team to parallelise much of the analysis code used to derive the experimental results presented in this thesis using the CUDA parallel computing platform [119]. This enables the data processing to be sped up by a factor of $\sim$60 relative to the IDL analysis code enabling inter-shot analysis. Full implementation of a frequency domain beam forming CUDA analysis code is yet to be realised and is left for future development.

In sections 5.1 and 5.2 we gave crude estimates of SAMI's radial resolution by considering the separation of normal incidence cutoffs at SAMI frequencies. In order to obtain more reliable values, there are many further considerations to be made. For example, the probing beam is typically at oblique incidence to the cutoff surface with the angle of incidence affecting the location of the scattering region. If one is measuring magnetic pitch angle then the technique proposed in section 6.4.1 relies on scattering turbulence structures being aligned perpendicular to the magnetic field. If the magnetic field vector changes abruptly with radius it is likely that interactions between these turbulent structures could affect the SAMI measurement. The radial resolution in further complicated if O and X-mode radiation is not separated as this delocalises the scattering location.

8.1.2 Hardware development

Though the capabilities of the SAMI diagnostic have not yet been explored in full, this system is ultimately limited and could be upgraded or overhauled in a number of ways.

Increased directionality could be achieved by (as discussed in section 3.3) increasing the number of antennas in the receiving array. Additional antenna channels using existing SAMI RF components would require a significant financial investment.

One way such a cost could be avoided is through the use of monolithic microwave integrated circuits (MMICs) [120]. These circuits can, once designed, be manufactured at significantly lower cost than conventional RF components. A large number of antenna channels would present significant digitisation and data storage requirements. However, FPGA digital pre-processing has already been developed for active probing using SAMI (discussed previously in section 5.2). A combination of digital down conversion, lower bit sampling and decreased digitisation rates could reduce the memory and digitisation requirements. With the use of a large number of antennas a narrow Gaussian beam, as used on conventional DBS experiments, could be constructed using the receiving array. If the receiving array was also capable of selecting a single mode of radiation then this would highly localise the scattering location allowing for measurements of turbulent velocity, radial electric field and $K_\perp$ spectra. If such a system could also operate at high power (relative to SAMI) then, as we have seen in sections 6.4.1 and 7.3, this would improve data quality. If a system could acquire several frequencies simultaneously (as opposed to frequency switching) this would increase temporal resolution as well as avoiding complications associated with frequency switching such as switching noise and data stitching.

As mentioned previously, the existing SAMI array designs (see figures 5.7 and 3.7) are not optimised for 2D Doppler backscattering experiments. The layout of an array optimised for measuring pitch angle, for example, may be elongated along the direction approximately perpendicular to a typical magnetic field inclination. This would give it better resolution along this axis. However, as discussed in section 3.3, array optimisation is an involved process and we leave this for future work.

Appendix A

Derivation of the force balance equation

By considering a distribution function f for a collection of particles of equal mass, one can derive the collisionless kinetic or *Vlasov* equation (sources of heat, sources of particles and collisions are neglected):

$$\frac{\partial f}{\partial t} + (\boldsymbol{v}_\mathrm{p} \cdot \boldsymbol{\nabla} f) + \frac{1}{m}(\boldsymbol{F} \cdot \boldsymbol{\nabla}_{v_\mathrm{p}}) f = 0 \tag{A.1}$$

The force vector, particle mass and particle velocity are given by $\boldsymbol{F}$, m and $\boldsymbol{v}_\mathrm{p}$ respectively ($\boldsymbol{\nabla}_{v_\mathrm{p}} = \partial/\partial \boldsymbol{v}_\mathrm{p}$). Multiplying Equation A.1 by $m\boldsymbol{v}_\mathrm{p}$ and integrating over velocity space gives:

$$m\frac{\partial}{\partial t}(n\boldsymbol{v}) + m\int \boldsymbol{v}_\mathrm{p}(\boldsymbol{v}_\mathrm{p} \cdot \boldsymbol{\nabla}) f \mathrm{d}^3\boldsymbol{v} + \int \boldsymbol{v}_\mathrm{p}(\boldsymbol{F} \cdot \boldsymbol{\nabla}_{v_\mathrm{p}}) f \mathrm{d}^3\boldsymbol{v}_\mathrm{p} = 0. \tag{A.2}$$

where $\boldsymbol{v}$ is the flow velocity of a fluid element and n is the density. Since the spatial gradient $\boldsymbol{\nabla}$ does not act on $\boldsymbol{v}_\mathrm{p}$, the second term in Equation A.2 can be written as:

$$m\int \boldsymbol{v}_\mathrm{p}(\boldsymbol{v}_\mathrm{p} \cdot \boldsymbol{\nabla}) f \mathrm{d}^3\boldsymbol{v} = m\int \boldsymbol{\nabla} \cdot (f\boldsymbol{v}_\mathrm{p}\boldsymbol{v}_\mathrm{p}) \mathrm{d}^3\boldsymbol{v} \tag{A.3}$$

$$= m\boldsymbol{\nabla} \cdot \int (f\boldsymbol{v}_\mathrm{p}\boldsymbol{v}_\mathrm{p}) \mathrm{d}^3\boldsymbol{v}_\mathrm{p} \tag{A.4}$$

$$= m\boldsymbol{\nabla} \cdot (n\overline{\boldsymbol{v}_\mathrm{p}\boldsymbol{v}_\mathrm{p}}) \tag{A.5}$$

where the bar over the quantity indicates velocity "averaging" $n\overline{\boldsymbol{v}_\mathrm{p}\boldsymbol{v}_\mathrm{p}} = \int f\boldsymbol{v}_\mathrm{p}\boldsymbol{v}_\mathrm{p}\mathrm{d}^3\boldsymbol{v}_\mathrm{p}$. The particle velocity can be written as the sum of the fluid velocity and random

thermal velocity: $\boldsymbol{v}_\mathrm{p} = \boldsymbol{v} + \boldsymbol{w}$. This allows the second term of Equation A.2 to be rewritten as

$$m\boldsymbol{\nabla}\cdot(n\overline{\boldsymbol{v}_\mathrm{p}\boldsymbol{v}_\mathrm{p}}) = m[\boldsymbol{\nabla}\cdot(n\boldsymbol{v}\boldsymbol{v}) + \boldsymbol{\nabla}\cdot(n\overline{\boldsymbol{w}\boldsymbol{w}}) + \boldsymbol{\nabla}\cdot n(\boldsymbol{v}\overline{\boldsymbol{w}} + \overline{\boldsymbol{w}}\boldsymbol{v})] \tag{A.6}$$

$$= m[\boldsymbol{\nabla}\cdot(n\boldsymbol{v}\boldsymbol{v}) + \boldsymbol{\nabla}\cdot(n\overline{\boldsymbol{w}\boldsymbol{w}}) \tag{A.7}$$

where we have used the fact that $\overline{\boldsymbol{w}} = 0$ by definition. Applying the product rule to the first term of Equation A.7 and using $\boldsymbol{w} = \boldsymbol{v}_\mathrm{p} - \boldsymbol{v}$ results in:

$$m\boldsymbol{\nabla}\cdot(n\overline{\boldsymbol{v}_\mathrm{p}\boldsymbol{v}_\mathrm{p}}) = m[\boldsymbol{\nabla}\cdot(n\boldsymbol{v})\boldsymbol{v} + n(\boldsymbol{v}\cdot\boldsymbol{\nabla})\boldsymbol{v}] + \boldsymbol{\nabla}\cdot\underline{\mathbf{P}} \tag{A.8}$$

where $\underline{\mathbf{P}} = mn(\overline{\boldsymbol{v}_\mathrm{p}\boldsymbol{v}_\mathrm{p}} - \boldsymbol{v}\boldsymbol{v}) = m\int f(\boldsymbol{v}_\mathbf{p}\boldsymbol{v}_\mathbf{p} - \boldsymbol{v}\boldsymbol{v})\mathrm{d}^3\boldsymbol{v}$ is the pressure tensor. If we now consider Equation A.2 once again, the third term can be written as

$$\int \boldsymbol{v}_\mathrm{p}(\boldsymbol{F}\cdot\boldsymbol{\nabla}_{v_\mathrm{p}})f\mathrm{d}^3\boldsymbol{v}_\mathrm{p} = \int \boldsymbol{\nabla}_{v_\mathrm{p}}(f\boldsymbol{v}_\mathrm{p}\mathbf{F})\mathrm{d}^3\boldsymbol{v}_\mathrm{p} - \int f\boldsymbol{v}_\mathrm{p}\boldsymbol{\nabla}_{v_\mathrm{p}}\cdot\mathbf{F}\mathrm{d}^3\boldsymbol{v} - \int f\mathbf{F}\cdot\boldsymbol{\nabla}_{v_\mathrm{p}}\boldsymbol{v}_\mathrm{p}\mathrm{d}^3\boldsymbol{v}_\mathrm{p} \tag{A.9}$$

where the product rule has been invoked. The first and second terms in Equation A.9 can be shown to be zero by applying the divergence theorem leaving only the third term as non zero. In addition by noting that the force vector is given by $\mathbf{F} = q(\mathbf{E} + \boldsymbol{v}_\mathrm{p}\times\mathbf{B})$:

$$\int \boldsymbol{v}_\mathrm{p}(\boldsymbol{F}\cdot\boldsymbol{\nabla}_{v_\mathrm{p}})f\mathrm{d}^3\boldsymbol{v}_\mathrm{p} = -\int f\mathbf{F}\cdot\boldsymbol{\nabla}_{v_\mathrm{p}}\boldsymbol{v}_\mathrm{p}\mathrm{d}^3\boldsymbol{v}_\mathrm{p} \tag{A.10}$$

$$= -\int f\mathbf{F}\mathrm{d}^3\boldsymbol{v}_\mathrm{p} \tag{A.11}$$

$$= -\int fq(\mathbf{E} + \boldsymbol{v}_\mathrm{p}\times\mathbf{B})\mathrm{d}^3\boldsymbol{v}_\mathrm{p} \tag{A.12}$$

$$= -nq(\mathbf{E} + \boldsymbol{v}\times\mathbf{B}) \tag{A.13}$$

Now, if we substitute the right-hand side of Equations A.8 and A.13 for the second and third terms in Equation A.2 respectively then the following results:

$$mn\frac{\partial\boldsymbol{v}}{\partial t} + m\boldsymbol{v}\frac{\partial n}{\partial t} + m\boldsymbol{v}\boldsymbol{\nabla}\cdot(n\boldsymbol{v}) + mn(\boldsymbol{v}\cdot\boldsymbol{\nabla})\boldsymbol{v} + \boldsymbol{\nabla}\cdot\underline{\mathbf{P}} - nq(\mathbf{E} + \boldsymbol{v}\times\mathbf{B}) = 0 \tag{A.14}$$

The second and third terms are equal to zero due to the continuity equation $\left(\frac{\partial n}{\partial t} + \boldsymbol{\nabla} \cdot (n\boldsymbol{v}) = 0\right)$ leaving us with the force balance equation.

$$m_j n_j \left[\frac{\partial \boldsymbol{v}_j}{\partial t} + (\boldsymbol{v}_j \cdot \nabla)\boldsymbol{v}_j \right] = n_j q_j (\mathbf{E} + \boldsymbol{v}_j \times \mathbf{B}) - \boldsymbol{\nabla} \cdot \underline{\mathbf{P}}_j \tag{A.15}$$

where $j = e$ for electrons $j = i$ for ions.

Appendix B

Acronyms and definitions of variables

ICF ..... Inertial Confinement Fusion
MCF ..... Magnetic Confinement Fusion
JET ..... Joint European Torus
MAST ..... Mega Ampère Spherical Tokamak
NSTX-U ..... National Spherical Torus eXperiment Upgrade
DEMO ..... DEMOnstration fusion power plant
ASDEX ..... Axially Symmetric Divertor EXperiment
AUG ..... ASDEX Upgrade
$\boldsymbol{\beta}$ ..... The ratio of plasma pressure to magnetic pressure
ELM ..... Edge Localised Mode
$\boldsymbol{p'_{\mathrm{ped}}}$ ..... Pedestal pressure gradient
$\boldsymbol{J_{\mathrm{ped}}}$ ..... Pedestal current density
$\boldsymbol{P_{\mathrm{i}}, P_{\mathrm{e}}}$ ..... Ion and electron pressures
$\boldsymbol{T_{\mathrm{i}}, T_{\mathrm{e}}}$ ..... Ion and electron temperatures
$\boldsymbol{E}$ ..... Electric field
$\boldsymbol{n_e}$ ..... Electron number density
$\parallel$ ..... Denotes component parallel to the magnetic field
$\perp$ ..... Denotes component perpendicular to the magnetic field
$\boldsymbol{e}$ ..... Electronic charge
$\boldsymbol{c}$ ..... Speed of light in vacuum
$\boldsymbol{j}$ ..... $\sqrt{-1}$
$\boldsymbol{K}$ ..... Turbulence wave vector
$\boldsymbol{\rho_{\mathrm{i}}}$ ..... Ion Larmor radius
$\boldsymbol{\lambda}$ ..... Wavelength of radiation

$\boldsymbol{\omega}$ ..... Frequency of radiation
$\boldsymbol{\omega_{\mathrm{i}}}$ ..... Frequency of incident radiation
$\boldsymbol{\omega_{\mathrm{s}}}$ ..... Frequency of scattered radiation
$\boldsymbol{\omega_{\mathrm{pe}}}$ ..... Plasma frequency
$\boldsymbol{\omega_{\mathrm{ce}}}$ ..... Electron cyclotron frequency
$\boldsymbol{\Delta\omega}$ ..... Frequency Doppler shift
$\boldsymbol{X}$ ..... ratio of plasma frequency to radiation frequency squared
$\boldsymbol{Y}$ ..... ratio of cyclotron frequency to radiation frequency
DBS ..... Doppler Backscattering
SAMI ..... Synthetic Aperture Microwave Imaging
FPGA ..... Field Programmable Gate Array
IF ..... Intermediate Frequency
LO ..... Local Oscillator
RF ..... Radio Frequency
DRO ..... Dielectric Resonance Oscillators
$\boldsymbol{\nu_{\mathrm{probe}}}$ ..... IF active probing frequency
BES ..... Beam Emission Spectroscopy
NBI ..... Neutral Beam Injection
LCFS ..... Last Closed Flux Surface
O-mode ..... Ordinary mode
X-mode ..... eXtraordinary mode
ST ..... Spherical Tokamak
$\boldsymbol{\lambda_D}$ ..... Debye Length
$\boldsymbol{\theta}$ ..... Horizontal angle in SAMI image coordinates
$\boldsymbol{\phi}$ ..... Vertical angle in SAMI image coordinates
$\boldsymbol{E_{\mathrm{r}}}$ ..... Radial electric field
$\boldsymbol{v_\theta, v_\phi}$ ..... Poloidal and toroidal components of the turbulence velocity
$\boldsymbol{B_\theta, B_\phi}$ ..... Poloidal and toroidal components of the magnetic field
$\boldsymbol{N}$ ..... Refractive index
$\boldsymbol{r}$ ..... Beam forming focal point
$\boldsymbol{x_i}$ ..... Position of the i^{th} antenna in the SAMI array
$\boldsymbol{\psi_i}$ ..... Phase shift applied to the i^{th} antenna channel whilst beam forming
$\boldsymbol{S_i^{\mathrm{A}}, \hat{S}_i^{\mathrm{A}}}$ ..... The signal from the i^{th} antenna in time and frequency domains
$\boldsymbol{S_{\mathrm{B}}, \hat{S}_{\mathrm{B}}}$ ..... Beam formed signal in the time and frequency domains
$\boldsymbol{w_i}$ ..... Complex calibration factor for the i^{th} antenna
$\boldsymbol{k}$ ..... Wave vector of the probing beam
$\boldsymbol{k_{\mathrm{i}}, k_{\mathrm{s}}}$ ..... Wave vector of the incident and scattered probing beam
$\boldsymbol{k_0}$ ..... Wave vector of probing beam in vacuum
$\boldsymbol{k_{\mathrm{sc}}}$ ..... Wave vector of probing beam at scattering location

$\boldsymbol{K}$ ..... Wave vector of the turbulence

$\boldsymbol{K}_{\perp}^{\mathbf{B}}$ Binormal component of turbulent wave vector perpendicular to the magnetic field and density surface normal

$\boldsymbol{\Omega}$ ..... Frequency of the turbulence

$\boldsymbol{v}_{\mathbf{turb}}$ ..... Turbulence velocity

$\boldsymbol{I}$ ..... In-phase signal component

$\boldsymbol{Q}$ ..... Quadrature signal component

$\boldsymbol{\theta}_{\mathbf{max}}$ ..... Field of view

$\boldsymbol{\theta}_{\mathbf{3dB}}$ ..... 3 dB width

$\boldsymbol{v}_{\mathrm{p}}$ ..... Particle velocity

$\boldsymbol{v}$ ..... Flow velocity of fluid element

SND ..... Single Null Discharge

DND ..... Double Null Discharge

RMP ..... Resonant Magnetic Perturbation

FWHM ..... Full Width Half Maximum

Bibliography

[1] J. P. H. E. Ongena and G. Van Oost. Energy for future centuries. Will fusion be an inexhaustible, safe and clean energy source? *Fusion Technology*, 37(2T), 2000.

[2] R. F. Post. The magnetic mirror approach to fusion. *Nuclear Fusion*, 27(10):1579, 1987.

[3] G. Grieger, W. Lotz, P. Merkel, J. Nührenberg, J. Sapper, E. Strumberger, H. Wobig, R. Burhenn, V. Erckmann, U. Gasparino, L. Giannoe, H. J. Hartfuss, R. Jaenicke, G. Kuhner, H. Ringler, A. Weller, F. Wagner, the W7X Team, and the W7-AS Team. Physics optimization of stellarators. *Physics of Fluids B*, 4(7):2081–2091, 1992.

[4] A. Isayama, Y. Kamada, N. Hayashi, T. Suzuki, T. Oikawa, T. Fujita, T. Fukuda, S. Ide, H. Takenaga, K. Ushigusa, T. Ozeki, Y. Ikeda, N. Umeda, H. Yamada, M. Isobe, Y. Narushima, K. Ikeda, S. Sakakibara, K. Yamazaki, K. Nagasaki, and the JT-60 Team. Achievement of high fusion triple product, steady-state sustainment and real-time NTM stabilization in high-βp ELMy H-mode discharges in JT-60U. *Nuclear Fusion*, 43(10):1272, 2003.

[5] M. Keilhacker, A. Gibson, C. Gormezano, P. J. Lomas, P. R. Thomas, M. L. Watkins, P. Andrew, B. Balet, D Borba, C. D. Challis, I. Coffey, G.A. Cottrell, H.P.L. De Esch, N. Deliyanakis, A. Fasoli, C.W. Gowers, H.Y. Guo, G.T.A. Huysmans, T.T.C. Jones, W. Kerner, R.W.T. König, M.J. Loughlin, A. Maas, F.B. Marcus, M.F.F. Nave, F.G. Rimini, G.J. Sadler, S.E. Sharapov, G. Sips, P. Smeulders, F.X. Söldner, A. Taroni, B.J.D. Tubbing, M.G. von Hellermann, D.J. Ward, and JET Team. High fusion performance from deuterium-tritium plasmas in JET. *Nuclear Fusion*, 39(2):209, 1999.

[6] T. Casper, Y. Gribov, A. Kavin, V. Lukash, R. Khayrutdinov, H. Fujieda, C. Kessel, and ITER Domestic Agencies. Development of the ITER baseline inductive scenario. *Nuclear Fusion*, 54(1):013005, 2014.

[7] F. Romanelli. Fusion Electricity: A Roadmap to the Realisation of Fusion Energy, European Fusion Development Agreement. Technical report, EFDA, 2012. ISBN 978-3-00-040720-8.

[8] A. Darke, M. Cox, J. Harbar, J. Hay, J. Hicks, J. Hill, D. Hutford, J. McKenzie, A. Morris, and M. Nightingale. The Mega Amp Spherical Tokamak. In *Symposium on Fusion Engineering*, volume 16, pages 1456–1459. Institute of Electrical & Electronics Engineers, Inc, 1995.

[9] J. E. Menard, S. Gerhardt, M. Bell, J. Bialek, A. Brooks, J. Canik, J. Chrzanowski, M. Denault, L. Dudek, D. A. Gates, N. Gorelenkov, W. Guttenfelder, R. Hatcher, J. Hosea, R. Kaita, S. Kaye, C. Kessel, E. Kolemen, H. Kugel, R. Maingi, M. Mardenfeld, D. Mueller, B. Nelson, C. Neumeyer, M. Ono, E. Perry, R. Ramakrishnan, R. Raman, Y. Ren, S. Sabbagh, M. Smith, V. Soukhanovskii, T. Stevenson, R. Strykowsky, D. Stutman, G. Taylor, P. Titus, K. Tresemer, K. Tritz, M. Viola, M. Williams, R. Woolley, H. Yuh, H. Zhang, Y. Zhai, A. Zolfaghari, and the NSTX Team. Overview of the physics and engineering design of NSTX upgrade. *Nuclear Fusion*, 52(8):083015, 2012.

[10] P. H. Rebut, R. J. Bickerton, and B. E. Keen. The Joint European Torus: installation, first results and prospects. *Nuclear Fusion*, 25(9):1011, 1985.

[11] R. Aymar, P. Barabaschi, and Y. Shimomura. The ITER design. *Plasma Physics and Controlled Fusion*, 44(5):519, 2002.

[12] Y. K. M. Peng and D. J. Strickler. Features of spherical torus plasmas. *Nuclear Fusion*, 26(6):769, 1986.

[13] J. A. Wesson and A. Sykes. Tokamak beta limit. *Nuclear Fusion*, 25(1):85, 1985.

[14] Y. K. M. Peng, P. J. Fogarty, T. W. Burgess, D. J. Strickler, B. E. Nelson, J. Tsai, C. A. Neumeyer, R. Bell, C. Kessel, J. Menard, D. Gates, B. LeBlanc, D. Mikkelsen, E. Fredrickson, L. Grisham, J. Schmidt, P. Rutherford, S. Sabbagh, A. Field, A. Sykes, I. Cook, O. Mitarai, and Y. Takase. A component test facility based on the spherical tokamak. *Plasma Physics and Controlled Fusion*, 47(12B):B263, 2005.

[15] P. B. Snyder, H. R. Wilson, J. R. Ferron, L. L. Lao, A. W. Leonard, T. H. Osborne, A. D. Turnbull, D. Mossessian, M. Murakami, and X. Q. Xu. Edge localized modes and the pedestal: A model based on coupled peeling–ballooning modes. *Physics of Plasmas*, 9(5):2037–2043, 2002.

[16] F. Wagner. A quarter-century of H-mode studies. *Plasma Physics and Controlled Fusion*, 49(12B):B1, 2007.

[17] H. Zohm. Edge localized modes (ELMs). *Plasma Physics and Controlled Fusion*, 38(2):105, 1996.

[18] P. B. Snyder, H. R. Wilson, and X. Q. Xu. Progress in the peeling-ballooning model of edge localized modes: Numerical studies of nonlinear dynamicsa). *Physics of Plasmas*, 12(5):056115, 2005.

[19] R. Scannell, M. J. Walsh, M. R. Dunstan, J. Figueiredo, G. Naylor, T. O'Gorman, S. Shibaev, K. J. Gibson, and H. Wilson. A 130 point Nd: YAG Thomson scattering diagnostic on MAST. *Review of Scientific Instruments*, 81(10):10D520, 2010.

[20] O. Sauter, C. Angioni, and Y. R. Lin-Liu. Neoclassical conductivity and bootstrap current formulas for general axisymmetric equilibria and arbitrary collisionality regime. *Physics of Plasmas*, 6(7):2834–2839, 1999.

[21] J. Wesson and D. J. Campbell. *Tokamaks*. Oxford University Press, 2011.

[22] S. C. Cowley, R. M. Kulsrud, and R. Sudan. Considerations of ion-temperature-gradient-driven turbulence. *Physics of Fluids B*, 3(10):2767–2782, 1991.

[23] J. C. Hillesheim. *Studies of turbulence and flows in the DIII-D tokamak*. PhD thesis, University of California, 2012.

[24] D. J. Applegate. *Gyrokinetic studies of a spherical tokamak H-mode plasma*. PhD thesis, Imperial College London, 2007.

[25] W. Dorland, F. Jenko, M. Kotschenreuther, and B. N. Rogers. Electron temperature gradient turbulence. *Physical Review Letters*, 85(26):5579, 2000.

[26] W. Guttenfelder, J. Candy, S. M. Kaye, W. M. Nevins, E. Wang, R. E. Bell, G. W. Hammett, B. P. LeBlanc, D. R. Mikkelsen, and H. Yuh. Electromagnetic transport from microtearing mode turbulence. *Physical Review Letters*, 106(15):155004, 2011.

[27] P. B. Snyder, N. Aiba, M. Beurskens, R. J. Groebner, L. D. Horton, A. E. Hubbard, J. W. Hughes, G. T. A. Huysmans, Y. Kamada, A. Kirk C. Konz, A.W. Leonard, J. Lönnroth, C.F. Maggi, R. Maingi, T.H. Osborne, N. Oyama, A. Pankin, S. Saarelma, G. Saibene, J.L. Terry, H. Urano, and H.R. Wilson. Pedestal stability comparison and ITER pedestal prediction. *Nuclear Fusion*, 49(8):085035, 2009.

[28] B. Coppi, H. P. Furth, M. N. Rosenbluth, and R. Z. Sagdeev. Drift instability due to impurity ions. *Physical Review Letters*, 17(7):377, 1966.

[29] F. Chen. *Introduction to Plasma Physicsc and Controlled Fusion*. World Scientific Publishing Co, 1987.

[30] P. C. Clemmow & J. P. Dougherty. *Electrodynamics of Particles and Plasmas*. Adison-Wesley, 1969.

[31] S. J. Freethy. *Synthetic aperture imaging of B-X-O mode conversion*. PhD thesis, The University of York, March 2012.

[32] V. L. Ginzburg. *The propagation of electromagnetic waves in plasmas*. Pergamon Press, 1970.

[33] T. H. Stix. *Waves in Plasmas*. AIP Press, 1992.

[34] D. A. Thomas, K. J. Brunner, S. J. Freethy, B. K. Huang, V. F. Shevchenko, and R. G. L. Vann. 2D Doppler backscattering using synthetic aperture microwave imaging of MAST edge plasmas. *Nuclear Fusion*, 56(2):026013, 2016. http://iopscience.iop.org/article/10.1088/0029-5515/56/2/026013.

[35] D. A. Thomas, K. J. Brunner, S. J. Freethy, B. K. Huang, V. F. Shevchenko, and R. G. L. Vann. Simultaneous 2D Doppler backscattering from edge turbulence. *Bulletin of the American Physical Society*, 60, 2015.

[36] E. Holzhauer, M. Hirsch, T. Grossmann, B. Branas, and F. Serra. Theoretical and experimental investigation of the phase-runaway in microwave reflectometry. *Plasma Physics and Controlled Fusion*, 40(11):1869, 1998.

[37] E. Z. Gusakov, A. V. Surkov, and A. Y. Popov. Multiple scattering effect in Doppler reflectometry. *Plasma Physics and Controlled Fusion*, 47(7):959, 2005.

[38] G. D. Conway, J. Schirmer, S. Klenge, W. Suttrop, E. Holzhauer, and the ASDEX Upgrade Team. Plasma rotation profile measurements using Doppler reflectometry. *Plasma Physics and Controlled Fusion*, 46(6):951, 2004.

[39] J. C. Hillesheim, W. A. Peebles, T. L. Rhodes, L L. Schmitz, T. A. Carter, P. A. Gourdain, and G. Wang. A multichannel, frequency-modulated, tunable Doppler backscattering and reflectometry system. *Review of Scientific Instruments*, 80(8):083507, 2009.

[40] M. Hirsch, E. Holzhauer, J. Baldzuhn, and B. Kurzan. Doppler reflectometry for the investigation of propagating density perturbations. *Plasma Physics and Controlled Fusion*, 43(12):1641, 2001.

[41] M. Hirsch and E. Holzhauer. Doppler reflectometry with optimized temporal resolution for the measurement of turbulence and its propagation velocity. *Plasma Physics and Controlled Fusion*, 46(4):593, 2004.

[42] C. Zhou, A. D. Liu, X. H. Zhang, J. Q. Hu, M. Y. Wang, H. Li, T. Lan, J. L. Xie, X. Sun, W. X. Ding, W. D. Liu, and C. X. Yu. Microwave Doppler

reflectometer system in the experimental advanced superconducting tokamak. *Review of Scientific Instruments*, 84(10):103511, 2013.

[43] X. Weiwen, D. Xuantong, L. Zetian, Y. Lianghua, S. Hongjuan, D. Xuru, Y. Longwen, and Y. Qingwei. Measurement of turbulence propagation velocity using Doppler reflectometer on HL-2A tokamak. *Plasma Science and Technology*, 10(4):403, 2008.

[44] T. Tokuzawa, A. Ejiri, K. Kawahata, K. Tanaka, I. Yamada, M. Yoshinuma, K. Ida, and C. Suzuki. Microwave Doppler reflectometer system in LHD[a)]. *Review of Scientific Instruments*, 83(10):10E322, 2012.

[45] A. A. Pshenichnikov, L. V. Kolik, N. I. Malykh, A. E. Petrov, M. A. Tereshchenko, N. K. Kharchev, and Y. V. Kholnov. The use of Doppler reflectometry in the l-2M stellarator. *Plasma Physics Reports*, 31(7):554–561, 2005.

[46] J. C. Hillesheim, N. A. Crocker, W. A. Peebles, H. Meyer, A. Meakins, A. R. Field, D. Dunai, M. Carr, N. Hawkes, and the MAST Team. Doppler backscattering for spherical tokamaks and measurement of high-k density fluctuation wavenumber spectrum in MAST. *Nuclear Fusion*, 55(7):073024, 2015.

[47] K. H. Burrell. Effects of E× B velocity shear and magnetic shear on turbulence and transport in magnetic confinement devices. *Physics of Plasmas*, 4(5):1499–1518, 1997.

[48] L. Schmitz, L. Zeng, T. L. Rhodes, J. C. Hillesheim, E. J. Doyle, R. J. Groebner, W. A. Peebles, K. H. Burrell, and G. Wang. Role of zonal flow predator-prey oscillations in triggering the transition to H-mode confinement. *Physical Review Letters*, 108(15):155002, 2012.

[49] T. Happel, T. Estrada, E. Blanco, V. Tribaldos, A. Cappa, and A. Bustos. Doppler reflectometer system in the stellarator TJ-ii. *Review of Scientific Instruments*, 80(7):073502, 2009.

[50] P. Hennequin, C. Honoré, A. Truc, A. Quéméneur, N. Lemoine, J. M. Chareau, and R. Sabot. Doppler backscattering system for measuring fluctuations and

their perpendicular velocity on Tore Supra. *Review of Scientific Instruments*, 75(10):3881–3883, 2004.

[51] T. Happel, G. D. Conway, W. Kasparek, B. Plaum, C. Lechte, D. Wagner, U. Stroth, and the ASDEX Upgrade Team. Design of a new Doppler reflectometer front-end for the ASDEX Upgrade Tokamak. In *Proceedings of the 10th International Reflectometry Workshop (IRW 10)*, 2011.

[52] J. C. Hillesheim, W. A. Peebles, T. L. Rhodes, L. Schmitz, A. E. White, and T. A. Carter. New plasma measurements with a multichannel millimeter-wave fluctuation diagnostic system in the DIII-D tokamak. *Review of Scientific Instruments*, 81(10):10D907, 2010.

[53] G. Wang, W. A. Peebles, T. L. Rhodes, M. E. Austin, Z. Yan, G. R. McKee, R. J. La Haye, K. H. Burrell, E. J. Doyle, J. C. Hillesheim, M. J. Lanctot, R. Nazikian, C. C. Petty, L. Schmitz, S. Smith, E. J. Strait, M. Van Zeeland, and L. Zeng. Multi-field characteristics and eigenmode spatial structure of geodesic acoustic modes in DIII-D L-mode plasmas. *Physics of Plasmas*, 20(9):092501, 2013.

[54] G. D. Conway, B. Scott, J. Schirmer, M. Reich, A. Kendl, and the ASDEX Upgrade Team. Direct measurement of zonal flows and geodesic acoustic mode oscillations in ASDEX Upgrade using Doppler reflectometry. *Plasma Physics and Controlled Fusion*, 47(8):1165, 2005.

[55] Z. Huang, C. A. de Meijere, S. Coda, L. Vermare, T. Vernay, V. Vuille, S. Brunner, J. Dominski, P. Hennequin, A. Kraemer-Flecken, G. Maimbourg, G. Merlo, L. Porte, and L. Villard. Multi-diagnostic characterization of geodesic acoustic modes in the TCV tokamak. In *Proceedings of the 40th EPS Conference on Plasma Physics*, number EPFL-CONF-197182, 2013. http://ocs.ciemat.es/EPS2013PAP/pdf/P2.175.pdf.

[56] R. Sabot, A. Macor, C. Nguyen, J. Decker, D. Elbeze, L. Eriksson, X. Garbet, M. Goniche, G. Huysmans, Y. Ladroit, P. Maget, and J. L. Segui. Observation of acoustic and subacoustic fast particles driven modes in Tore-Supra. *Nuclear Fusion*, 49(8):085033, 2009.

[57] P. Hennequin, C. Honoré, A. Truc, A. Quéméneur, C. Fenzi-Bonizec, C. Bourdelle, X. Garbet, G. T. Hoang, and the Tore Supra team. Fluctuation spectra and velocity profile from Doppler backscattering on Tore Supra. *Nuclear Fusion*, 46(9):S771, 2006.

[58] A. D. Gurchenko, E. Z. Gusakov, A. B. Altukhov, E. P. Selyunin, L. A. Esipov, M. Yu Kantor, D. V. Kouprienko, S. I. Lashkul, A. Y. Stepanov, and F. Wagner. Spatial structure of the geodesic acoustic mode in the FT-2 tokamak by upper hybrid resonance Doppler backscattering. *Plasma Physics and Controlled Fusion*, 55, 2013.

[59] V. V. Bulanin, V. I. Varfolomeev, V. K. Gusev, A. E. Ivanov, S. V. Krikunov, G. S. Kurskiev, M. M. Larionov, V. B. Minaev, M. I. Patrov, A. V. Petrov, N. V. Sakharov, S. Yu. Tolstyakov, N. A. Khromov, and A. Yu. Yashin. Observation of filaments on the Globus-M tokamak by Doppler reflectometry. *Technical Physics Letters*, 37(4):340–343, 2011.

[60] C. Lechte. Investigation of the scattering efficiency in Doppler reflectometry by two-dimensional full-wave simulations. *IEEE Transactions on Plasma Science*, 37(6):1099–1103, 2009.

[61] I. H. Hutchinson. *Principles of plasma diagnostics*. Cambridge University Press, 2005.

[62] P. Hennequin. Scaling laws of density fluctuations in tokamak plasmas. *Comptes Rendus Physique*, 7(6):670–678, 2006.

[63] E. Z. Gusakov and A. V. Surkov. Spatial and wavenumber resolution of Doppler reflectometry. *Plasma Physics and Controlled Fusion*, 46(7):1143, 2004.

[64] B. D. Scott. The mechanism of self-sustainment in collisional drift wave turbulence. *Physics of Fluids B*, 4(8):2468–2494, 1992.

[65] K. Ida. Experimental studies of the physical mechanism determining the radial electric field and its radial structure in a toroidal plasma. *Plasma Physics and Controlled Fusion*, 40(8):1429, 1998.

[66] A. R. Field, J. McCone, N. J. Conway, M. Dunstan, S. Newton, and M. Wisse. Comparison of measured poloidal rotation in MAST spherical tokamak plasmas with neo-classical predictions. *Plasma Physics and Controlled Fusion*, 51(10):105002, 2009.

[67] A. R. Field, D. Dunai, R. Gaffka, Y-C. Ghim, I. Kiss, B. Mészáros, T. Krizsanóczi, S. Shibaev, and S. Zoletnik. Beam emission spectroscopy turbulence imaging system for the MAST spherical tokamak. *Review of Scientific Instruments*, 83(1):013508, 2012.

[68] N. J. Conway, P. G. Carolan, J. McCone, M. J. Walsh, and M. Wisse. High-throughput charge exchange recombination spectroscopy system on MAST. *Review of Scientific Instruments*, 77(10):10F131, 2006.

[69] C. Angioni, L. Fattorini, A. G. Peeters, F. Ryter, F. Jenko, C. D. Conway, T. Dannert, H. U. Fahrbachand, M. Reich, W. Suttrop, and the ASDEX Upgrade Team. Relationship between density peaking, particle thermodiffusion, Ohmic confinement, and microinstabilities in ASDEX Upgrade L-mode plasmas. *Physics of Plasmas*, 12(4):040701, 2005.

[70] P. Barton. Digital beam forming for radar. *Communications, Radar and Signal Processing, IEE Proceedings F*, 127(4):266–277, 1980.

[71] T. E. Curtis and R. J. Ward. Digital beam forming for sonar systems. *Communications, Radar and Signal Processing, IEE Proceedings F*, 127(4):257–265, 1980.

[72] S. Rost and C. Thomas. Array seismology: methods and applications. *Reviews of Geophysics*, 40(3), 2002.

[73] J. Litva and L. K. Titus. *Digital beamforming in wireless communications*. Artech House, Inc., 1996.

[74] C. K. Hansen. *Beamforming techniques and interference mitigation using a multiple feed array for radio astronomy*. PhD thesis, Brigham Young University, 2004. http://scholarsarchive.byu.edu/etd/216.

[75] X. Anguera, C. Wooters, and J. Hernando. Acoustic beamforming for speaker diarization of meetings. *IEEE Transactions on Audio, Speech, and Language Processing*, 15(7):2011–2022, 2007.

[76] L. Jian-yu, H. Zou, and J. F. Greenleaf. Biomedical ultrasound beam forming. *Ultrasound in Medicine & Biology*, 20(5):403–428, 1994.

[77] V. F. Shevchenko, R. G. L. Vann, S. J. Freethy, and B. K. Huang. Synthetic aperture microwave imaging with active probing for fusion plasma diagnostics. *Journal of Instrumentation*, 7(10):P10016, 2012.

[78] R. Fitzpatrick. Introduction to plasma physics. *The University of Texas at Austin*, page 242, 2008.

[79] E. Poli, A. G. Peeters, and G. V. Pereverzev. TORBEAM, a beam tracing code for electron-cyclotron waves in tokamak plasmas. *Computer Physics Communications*, 136(1):90–104, 2001.

[80] G. V. Pereverzev. Beam tracing in inhomogeneous anisotropic plasmas. *Physics of Plasmas*, 5(10):3529–3541, 1998.

[81] W. M. Stacey. Neoclassical calculation of poloidal rotation and poloidal density asymmetries in tokamaks. *Physics of Plasmas*, 9(9):3874–3883, 2002.

[82] P. Rohmann, S. Wolf, W. Kasparek, B. Plaum, and J. Hesselbarth. A 32-element frequency-steered array antenna for reflectometry in W-band. In *2013 IEEE International Symposium on Phased Array Systems and Technology*, pages 559–563, 2013.

[83] B. K. Huang. *Development of FPGA controlled diagnostics on the MAST fusion reactor*. PhD thesis, Durham University, 2013.

[84] P. J. Gibson. Proceedings of the 9$^{\text{th}}$ European Microwave Conference, 1979. http://ieeexplore.ieee.org/xpl/articleDetails.jsp?arnumber=4131323.

[85] D. H. Schaubert, E. L. Kollberg, T. L. Korzeniowski, T. Thungren, J. Johansson, and K. Yngvesson. Endfire tapered slot antennas on dielectric substrates. *IEEE Transactions on Antennas and Propagation*, 33(12):1392–1400, 1985.

[86] K. S. Yngvesson, T. L. Korzeniowski, Kim Y-S, E. L. Kollberg, and J. F. Johansson. The tapered slot antenna - a new integrated element for millimeter-wave applications. *IEEE Transactions on Microwave Theory and Techniques*, 37(2):365–374, 1989.

[87] T-H. Chio and D. H. Schaubert. Parameter study and design of wide-band widescan dual-polarized tapered slot antenna arrays. *IEEE Transactions on Antennas and Propagation*, 48(6):879–886, 2000.

[88] S. Sugawara, Y. Maita, K. Adachi, K Mori, and Koji Mizuno. A mm-wave tapered slot antenna with improved radiation pattern. In *Microwave Symposium Digest, 1997., IEEE MTT-S International*, volume 2, pages 959–962. IEEE, 1997.

[89] E. Thiele and A. Taflove. FD-TD analysis of Vivaldi flared horn antennas and arrays. *IEEE Transactions on Antennas and Propagation*, 42(5):633–641, 1994.

[90] S. G. Kim. *Wideband two-dimensional and multiple beam phased arrays and microwave applications using piezoelectric transducers.* PhD thesis, Texas A&M University, 2005.

[91] M. J. Ammanii and Z. N. Chen. Wideband monopole antennas for multi-band wireless systems. *IEEE Transactions on Antennas and Propagation*, 45(2), 2003.

[92] R. O'Brient. *A log-periodic focal-plane architecture for cosmic microwave background polarimetry.* PhD thesis, University of California, Berkeley, 2010.

[93] S. Nagarani. Performance of broadband directional log periodic planar 2-petal and 4-petal sinuous antennas. *Global Journal of Comuter Application and Technology*, 2(1), 2012.

[94] K. S. Saini and R. F. Bradley. The sinuous antenna - a dual polarized element for wideband phased array feed application. *Electronic Division Internal Memo*, 1996. http://www.gb.nrao.edu/electronics/edir/edir301.pdf.

[95] S. J. Freethy, V. F. Shevchenko, and R. G. L. Vann. Optimization of wide field interferometric arrays via simulated annealing of a beam efficiency function. *IEEE Transactions on Antennas and Propagation*, 60(11):5442–5446, 2012.

[96] A. Camps, I. Corbella, J. Bara, and F. Torres. Radiometric sensitivity computation in aperture synthesis interferometric radiometry. *IEEE Transactions on Geoscience and Remote Sensing*, 36(2):680–685, 1998.

[97] D. Clarke. *Stellar Polarimetry*. Wiley Online Library, 2010.

[98] A. R. Thompson, J. M. Moran, and G. W. Swenson Jr. *Interferometry and synthesis in radio astronomy*. John Wiley & Sons, 2008.

[99] R. Pánek, O. Bilyková, V. Fuchs, M. Hron, P. Chráska, P. Pavlo, J. Stöckel, J. Urban, V. Weinzettl, J. Zajac, and F. Zacek. Reinstallation of the COMPASS-D tokamak in IPP ASCR. *Czechoslovak Journal of Physics*, 56(2):B125–B137, 2006.

[100] D. A. Thomas, K. J. Brunner, S. J. Freethy, B. K. Huang, V. F. Shevchenko, and R. G. Vann. Observations of 2D Doppler backscattering on MAST using SAMI. In *Talk presented at 12th International Reflectometry Workshop (IRW 12)*, Jülich, 2015.

[101] L. L. Lao, H. St. John, R. D. Stambaugh, A. G. Kellman, and W. Pfeiffer. Reconstruction of current profile parameters and plasma shapes in tokamaks. *Nuclear Fusion*, 25(11):1611, 1985.

[102] S. J. Freethy, B. K. Huang, V. F. Shevchenko, and R. G. L. Vann. Lensless passive and active microwave imaging on MAST. *Plasma Physics and Controlled Fusion*, 55(12):124010, 2013.

[103] S. J. Freethy, K. G. McClements, S. C. Chapman, R. O. Dendy, W. N. Lai, S. J. P. Pamela, V. F. Shevchenko, and R. G. L. Vann. Electron kinetics inferred from observations of microwave bursts during edge localized modes in the Mega-Amp Spherical Tokamak. *Physical Review Letters*, 114(12):125004, 2015.

[104] B. P. LeBlanc, R. E. Bell, D. W. Johnson, D. E. Hoffman, D. C. Long, and R. W. Palladino. Operation of the NSTX Thomson scattering system. *Review of Scientific Instruments*, 74(3):1659–1662, 2003.

[105] A. Diallo, B. P. LeBlanc, G. Labik, and D. Stevens. Prospects for the Thomson scattering system on NSTX-Upgrade. *Review of Scientific Instruments*, 83(10):10D532, 2012.

[106] K. J. Brunner, J. C. Chorley, N. A. Dipper, G. Naylor, R. M. Sharples, G. Taylor, D. A. Thomas, and R. G. L. Vann. Modifications to the synthetic aperture microwave imaging diagnostic. *Review of Scientific Instruments*. Submitted 2016.

[107] V. V. Bulanin, S. V. Lebedev, L. S. Levin, and V. S. Roytershteyn. Study of plasma fluctuations in the Tuman-3m tokamak using microwave reflectometry with an obliquely incident probing beam. *Plasma Physics Reports*, 26(10):813–819, 2000.

[108] T. R. N. Williams, A. Köhn, M. R. O'Brien, and R. G. L. Vann. Propagation in 3D of microwaves through density perturbations. *Plasma Physics and Controlled Fusion*, 56(7):075010, 2014.

[109] M. P. S. Nightingale, G. W. Crawford, S. J. Gee, D. J. Hurford, D. Martin, M. R. Simmonds, R. T. C. Smith, C. C. Tsai, and S. E. V. Warder. The MAST neutral beam injection system. *Fusion Engineering and Design*, 56:529–532, 2001.

[110] N. J. Conway, M. F. M. De Bock, C. A. Michael, M. J. Walsh, P. G. Carolan, N. C. Hawkes, E. Rachlew, J. F. G. McCone, S. Shibaev, and G. Wearing. The MAST motional stark effect diagnostic. *Review of Scientific Instruments*, 2010.

[111] M. Brix, N. C. Hawkes, A. Boboc, V. Drozdov, S. E. Sharapov, and JET-EFDA Contributors. Accuracy of EFIT equilibrium reconstruction with internal diagnostic information at JETa). *Review of Scientific Instruments*, 79(10):10F325, 2008.

[112] A. Kirk, E. Nardon, R. Akers, M. Bécoulet, G. De Temmerman, B. Dudson, B. Hnat, Y. Q. Liu, R. Martin, P. Tamain, D. Taylor, and the MAST team. Resonant magnetic perturbation experiments on MAST using external and internal coils for ELM control. *Nuclear Fusion*, 50(3):034008, 2010.

[113] R. A. Moyer, S. Mordijck, C. Rost, G. R. McKee, T. L. Rhodes, E. J. Doyle, L. Zeng, L. Schmitz, , and T. E. Evans. Impact of resonant magnetic perturbations (rmps) on turbulence drives, damping, and transport. *Bulletin of the American Physical Society*, 55, 2010.

[114] C. Laviron, A. J. H. Donné, M. E. Manso, and J. Sanchez. Reflectometry techniques for density profile measurements on fusion plasmas. *Plasma Physics and Controlled Fusion*, 38(7):905, 1996.

[115] J. Manickam. Stability of n=1 internal modes in tokamaks. *Nuclear Fusion*, 24(5):595, 1984.

[116] R. G. L. Vann, K. J. Brunner, R. Ellis, G. Taylor, and D. A. Thomas. Preliminary measurements of the edge magnetic field pitch from 2-D Doppler backscattering in MAST and NSTX-U. *Review of Scientific Instruments*. Submitted 2016.

[117] F. M. Levinton and H. Yuh. The motional stark effect diagnostic on NSTX. *Review of Scientific Instruments*, 79(10):10F522, 2008.

[118] T. N. R. Williams. *Full-wave simulation of high-frequency electromagnetic propagation through inhomogeneous plasma*. PhD thesis, The University of York, September 2014.

[119] J. C. Chorley, R. J. Akers, K. J. Brunner, N. A. Dipper, S. J. Freethy, R. M. Sharples, V. F. Shevchenko, D. A. Thomas, and R. G. L. Vann. GPU-Based data processing for 2-D microwave imaging on MAST. *Fusion Science and Technology*, 69(3), 2016.

[120] R. A. Pucel. Monolithic microwave integrated circuits. *New York, IEEE Press*, 1985.

[121] L. C. Appel, G. T. A. Huysmans, L. L. Lao, P. J. McCarthy, D. G. Muir, E. R. Solano, J. Storrs, D. Taylor, W. Zwingmann, contributors to the EFDA Integrated Tokamak Modelling (ITM) Task Force, and JET-EFDA Contributors. A unified approach to equilibrium reconstruction. In *Proceedings-33rd EPS conference on Controlled Fusion and Plasma Physics*, 2006.

[122] E. Blanco, T. Estrada, and J. Sánchez. Doppler reflectometry studies using a two-dimensional full-wave code. *Plasma Physics and Controlled Fusion*, 48(5):699, 2006.

[123] J. D. S. Langley, P. S. Hall, and P. Newham. Balanced antipodal Vivaldi antenna for wide bandwidth phased arrays. *Microwaves, Antennas and Propagation, IEE Proceedings*, 143:97–102, 1996.

[124] B. Lloyd, J. W. Ahn, R. J. Akers, L. C. Appel, E. R. Arends, K. B. Axon, R. J. Buttery, C. Byrom, P. G. Carolan, C. Challis, D. Ciric1, N.J. Conway, M. Cox, G.F. Counsell, G. Cunningham, A. Darke, A. Dnestrovskij, J. Dowling, M.R. Dunstan, A.R. Field, S.J. Fielding, S. Gee1, M.P. Gryaznevich, P. Helander, M. Hole, M.B. Hood, P.A. Jones, A. Kirk, I.P. Lehane, G.P. Maddison, S.J. Manhood, R. Martin, G.J. McArdle, K.G. McClements, M.A. McGrath, H. Meyer, A.W. Morris, S.K. Nielsen, M. Nightingale, A. Patel, T. Pinfold, M.N. Price, J. Qin, C. Ribeiro, C.M. Roach, D.C. Robinson1, O. Sauter, V. Shevchenko, S. Shibaev, K. Stammers, A. Sykes, A. Tabasso, D. Taylor, M.R. Tournianski, G. Turri, M. Valovic, G. Voss, M.J. Walsh, S. Warder, J.R. Watkins, H.R. Wilson, Y. Yang, S. You, the MAST, and NBI teams. Overview of recent experimental results on MAST. *Nuclear Fusion*, 43(12):1665, 2003.

[125] G. Vayakis, C. I. Walker, F. Clairet, R. Sabot, V. Tribaldos, T. Estrada, E. Blanco, J. Sánchez, G. G. Denisov, V. I. Belousov, F. Da Silva, P. Varela, M.E. Manso, L. Cupido, J. Dias, N. Valverde, V.A. Vershkov, D.A. Shelukhin, S.V. Soldatov, A.O. Urazbaev, E. Yu Frolov, and S. Heuraux. Status and prospects for mm-wave reflectometry in ITER. *Nuclear Fusion*, 46(9):S836, 2006.

[126] L. D. Landau and E. M. Lifshitz. *The Classical Theory of Fields*, volume 2 of *Course of Theoretical Physics*. Butterworth Heinemann, 4$^{\text{th}}$ edition, 2010.

[127] H. Biglari, P. H. Diamond, and P. W. Terry. Influence of sheared poloidal rotation on edge turbulence. *Physics of Fluids B*, 2(1):1–4, 1990.

[128] B. B. Kadomtsev and O. P. Pogutse. Trapped particles in toroidal magnetic systems. *Nuclear Fusion*, 11(1):67, 1971.